TECHNISCHE UNIVERSITÄT MÜNCHEN
TUM Campus Straubing für Biotechnologie und Nachhaltigkeit

Model-based Scale-up of the Continuous Production of Poly(oxymethylene) Dialkyl Ethers

Johannes Voggenreiter

Vollständiger Abdruck der von der promotionsführenden Einrichtung TUM Campus Straubing für Biotechnologie und Nachhaltigkeit der Technischen Universität München zur Erlangung des akademischen Grades eines

Doktors der Ingenieurwissenschaften (Dr.-Ing.)

genehmigten Dissertation.

Vorsitzender: Prof. Dr.-Ing. Michael Zavrel
Prüfer der Dissertation: 1. Prof. Dr.-Ing. Jakob Burger
2. Prof. Dr.-Ing. Jörg Sauer

Die Dissertation wurde am 11.07.2022 bei der Technischen Universität München eingereicht und von der promotionsführenden Einrichtung TUM Campus Straubing für Biotechnologie und Nachhaltigkeit am 08.11.2022 angenommen.

Danksagung

Die vorliegende Arbeit entstand während meiner Tätigkeit als wissenschaftlicher Mitarbeiter der Professur für Chemische und Thermische Verfahrenstechnik am Campus Straubing für Biotechnologie und Nachhaltigkeit der Technischen Universität München.

Als Erstes danke ich meinem Doktorvater Prof. Dr.-Ing. Jakob Burger für seine fachlichen Ratschläge, sein großes Interesse an meiner Arbeit, sein uneingeschränktes Vertrauen in meine Fähigkeiten und nicht zuletzt, dass er mir immer den Rücken freihielt.

Prof. Dr.-Ing. Jörg Sauer danke ich für die Begutachtung dieser Arbeit und Prof. Dr.-Ing. Michael Zavrel für die Übernahme des Prüfungsvorsitzes. Dr. Ulrich Arnold danke ich für seine Rolle als Mentor während meiner Promotion.

Ein herzlicher Dank geht an die NAMOSYN Kollegen Christian Breitkreuz aus Kaiserslautern und Denis Worch aus Leipzig für die angenehme und produktive Zusammenarbeit.

Während meiner Zeit an der Universität konnte ich mit vielen tollen Menschen zusammenarbeiten, welche die vergangenen Jahre zu der ereignisreichen Zeit gemacht haben, an die ich mich immer gerne erinnern werde. Birgit Aich-Bauer danke ich neben der Hilfe bei administrativen Aufgaben besonders für ihr offenes Ohr und ihre Freundschaft. Christina Wolf danke ich für ihre kompetente Unterstützung in allen Laborangelegenheiten. Stefan Hartl danke ich für seinen großen Einsatz bei der Planung und beim Aufbau der Pilotanlage. Yannic Tönges danke ich für sein Vorbild als Senior PhD Student. Eva Kirchinger danke ich für die gemeinsame Zeit im Büro und für die manchmal notwendige Ablenkung. Quirin Göttl danke ich für seine Tätigkeit als Gruppenbuchmacher. Bei Alvaro Ferre bedanke ich mich für die immer angenehme Zusammenarbeit bei allen OME Themen. Leandros Paschalidis danke ich für die zahlreichen Lehren über die deutsche Grammatik. Natalie Rosen danke ich für den frischen Wind im Büro durch ihre fröhliche Art. Lukas Winklbauer danke ich für seine qualifizierte Nachfolge als Chief Social Officer.

Darüber hinaus bedanke ich mich bei allen Studierenden, die zu dieser Arbeit beigetragen haben: Theresa Büchel, Daniela Fröschl, Matthias Tobler, Fabian Turkowski und Pascal van de Zande.

Ein großer Dank geht an meine Familie, insbesondere an meine Eltern. Danke, dass ihr mir immer gute Vorbilder wart und seid, dass ihr immer an mich glaubt und mir all das ermöglicht habt. Zuletzt möchte ich mich noch bei der wichtigsten Person in meinem Leben bedanken. Liebe Laura, danke für dein Verständnis, deine grenzenlose Unterstützung und deine Liebe.

Mühldorf am Inn, im März 2023
Johannes Voggenreiter

Abstract

Poly(oxymethylene) dimethyl ethers (OME) are discussed as a neat alternative or blend component to diesel fuel offering soot-free combustion and sustainable production pathways. OME are currently produced mostly in water-free processes. Even though water-tolerant processes offer greater overall efficiencies, they lack industrial realization.

The formation of side products during the OME synthesis via a water-tolerant route from methanol and aqueous formaldehyde solution over the acidic ion-exchange resin Amberlyst 46 as heterogeneous catalyst is studied. Reaction experiments at elevated temperatures are carried out in a batch reactor. Trioxane, methyl formate, and formic acid are detected and quantified. Trioxane is formed reversibly and limited by the chemical equilibrium. The formation of methyl formate and formic acid is linked via the esterification reaction and umlimited. A model is developed, fitted to the experimental results, and used in process simulation studies to examine the implications for the process design. Some side products accumulate within the process and, thus, their removal is indispensable. Introducing a purge stream results in 2.7% loss of product at a reactor temperature of 343.15 K. The loss of product could be further reduced by applying more selective removal methods.

The continuous production of OME from methanol and formaldehyde in tubular reactors using Amberlyst 46 as catalyst is studied. Reaction experiments with varying feed composition and operating conditions are carried out. Catalyst stability experiments are performed and catalyst deactivation is detected. The deactivation originates from ion exchange with cations present in feed solutions and is fully reversible by acid treatment. A pseudo-homogeneous model is adjusted to the experimental data and is able to reliably describe the reaction progress throughout the reactor. The adjusted model is used to design the reactor of an industrial-scale process with a production capacity of 100 kt/a $\mathrm{OME}_{3\text{–}5}$. The space–time yield is selected to 10 kg/($\mathrm{kg}_{\mathrm{cat}} \cdot \mathrm{h}$). Feasible reactor geometries are found for multitube reactors. This work demonstrates that the large-scale production of OME is feasible in tubular reactors.

Other representatives of the group of poly(oxymethylene) dialkyl ethers (OAE) feature similar favorable properties as OME. Moreover, properties can be adjusted to specific applications by exchanging the terminating alkyl group. This work presents a generalized model to describe the chemical equilibrium of water-free mixtures containing OAE, with various terminating alkyl groups and chain lengths, and trioxane as anhydrous formaldehyde source. The entirely predictive model is based on a generalized equilibrium constant for the formaldehyde oligomerization and statistical considerations. Reaction experiments with various feed compositions are performed at different temperatures and samples are analyzed by NMR spectroscopy. OAE with chain lengths $n \leq 5$ are quantified. The model performs very well when compared to the experimental results of the present work and is thus able to fully describe the chemical equilibrium in mixtures containing OAE and a formaldehyde source. The presented model serves as reliable base for further extensions regarding more complex alkyl groups and systems containing water and alcohols.

Kurzfassung

Poly(oxymethylen) dimethylether (OME) werden als saubere Alternative oder als Mischungsbestandteil zu Dieselkraftstoff diskutiert, da sie eine rußfreie Verbrennung und nachhaltige Produktionswege bieten. OME werden aktuell hauptsächlich in wasserfreien Prozessen hergestellt. Obwohl wassertolerante Verfahren eine höhere Prozesseffizienz bieten, mangelt es an der industriellen Umsetzung.

Die Bildung von Nebenprodukten während der OME-Synthese aus Methanol und wässriger Formaldehydlösung über eine wassertolerante Route mit dem sauren Ionenaustauscherharz Amberlyst 46 als heterogenen Katalysator wird untersucht. Es werden Reaktionsexperimente bei erhöhter Temperatur in einem Batch-Reaktor durchgeführt. Trioxan, Methylformiat und Ameisensäure werden nachgewiesen und quantifiziert. Trioxan wird reversibel gebildet und durch das chemische Gleichgewicht begrenzt. Die Bildung von Methylformiat und Ameisensäure ist über die Veresterungsreaktion gekoppelt und nicht limitiert. Es wird ein Modell entwickelt, das an die experimentellen Ergebnisse angepasst und in Prozesssimulationsstudien verwendet wird, um die Auswirkungen auf das Prozessdesign zu untersuchen. Einige Nebenprodukte reichern sich im Prozess an, so dass ihre Entfernung unerlässlich ist. Die Einführung eines Purgestroms führt bei einer Reaktortemperatur von 343,15 K zu einem Produktverlust von 2,7%. Der Produktverlust könnte durch die Anwendung selektiverer Methoden zur Ausschleusung der Nebenprodukte weiter verringert werden.

Die kontinuierliche Herstellung von OME aus Methanol und Formaldehyd in Rohrreaktoren unter Verwendung von Amberlyst 46 als Katalysator wird untersucht. Es werden Reaktionsexperimente mit unterschiedlicher Feedzusammensetzung bei verschiedenen Betriebsbedingungen durchgeführt. Zudem werden Experimente zur Katalysatorstabilität durchgeführt, wobei eine Deaktivierung des Katalysators festgestellt wird. Die Deaktivierung geht auf einen Ionenaustausch mit den in der Feedlösung vorhandenen Kationen zurück und ist durch eine Säurebehandlung vollständig reversibel. Ein pseudohomogenes Modell wird an die experimentellen Daten angepasst und ist in der Lage, den Reaktionsverlauf im gesamten Reaktor zuverlässig zu beschreiben. Das angepasste Modell wird zur Auslegung des Reaktors eines großtechnischen Verfahrens mit einer Produktionskapazität von 100 kt/a OME_{3-5} verwendet. Die Raum-Zeit-Ausbeute wird auf

10 kg/(kg$_{\mathrm{cat}}$ · h) festgelegt. Durch den Einsatz von mehreren parallelen Rohrreaktoren oder Rohrbündelreaktoren werden vernünftige Reaktorabmessungen erzielt. Damit zeigt diese Arbeit, dass die großtechnische Herstellung von OME in Rohrreaktoren möglich ist.

Weitere Vertreter der Gruppe der Poly(oxymethylen) dialkylether (OAE) weisen ähnlich vorteilhafte Eigenschaften wie OME auf. Darüber hinaus können die Eigenschaften durch den Austausch der endständigen Alkylgruppen an spezifische Anwendungen angepasst werden. In dieser Arbeit wird ein allgemeines Modell zur Beschreibung des chemischen Gleichgewichts von wasserfreien Mischungen vorgestellt, die OAE mit verschiedenen endständigen Alkylgruppen und Kettenlängen und Trioxan als wasserfreie Formaldehydquelle enthalten. Das vollständig prädiktive Modell basiert auf einer allgemeines Gleichgewichtskonstante für die Oligomerisierung mit Formaldehyd und statistischen Überlegungen. Es werden Reaktionsexperimente mit verschiedenen Feedzusammensetzungen bei unterschiedlichen Temperaturen durchgeführt. Die Proben werden mittels NMR-Spektroskopie analysiert. OAE mit Kettenlängen $n \leq 5$ werden quantifiziert. Beim Vergleich zu den experimentellen Ergebnisse der vorliegenden Arbeit schneidet das Modell sehr gut ab und ist somit in der Lage, das chemische Gleichgewicht in Mischungen mit OAE und einer Formaldehydquelle vollständig zu beschreiben. Das vorgestellte Modell dient somit als zuverlässige Grundlage für Erweiterungen hinsichtlich komplexerer Alkylgruppen und Systemen, die Wasser und Alkohole enthalten.

Contents

List of Symbols

Latin symbols

a_j, b_j	Correlation parameters
A_j, B_j	Correlation parameters
c	Concentration
$c_{\mathrm{cat}}^{\mathrm{H^+}}$	Catalyst activity in terms of $\mathrm{H^+}$-loading (amount of acid sites per dry mass)
$c_{p,i}^{l}$	Molar liquid heat capacity of component i
d_{cat}	Diameter of a single catalyst particle
d_{R}	Diameter of the reactor
$F(t)$	Cumulative distribution curve
$\Delta h_{f,i}^{0}$	Standard heat of formation
$\Delta_{\mathrm{R}} h_j$	Reaction enthalpy of reaction j
k_j	Reaction rate constant of reaction j
K_j	Mole fraction-based chemical equilibrium constant of reaction j
L_{R}	Length of the reactor
$\dot{m}$	Mass flow rate
m_{cat}	Mass of dry catalyst
m_{cat}^{*}	Already passed mass of dry catalyst
m_i^0	Initial weights of compontent i
$\hat{m}_i$	Acidic overall mass of component i
m_{L}	Mass of liquid mixture
$m_{\mathrm{L},0}$	Initial mass of liquid mixture
M_i	Molar mass of compontent i
n	Oligomer chain length
n_i	True amount of component i
$\tilde{n}_i$	Neutral overall amount of component i
$\dot{n}_i$	Molar flow rate of component i
n_{max}	Maximum oligomer chain length considered in the model
n_{R}	Number of tubes

N_C	Total number of components
N_G	Total number of alkyl groups in G considered in the model
N_R	Total number of reactions
p	Pressure
Δp	Pressure drop
r_j	Reaction rate of reaction j
t	Time
T	Temperature
$T_{\mathrm{b},i}$	Standard boiling point of component i
T_R	Reactor temperature
ΔT_ad	Adiabatic temperature rise
u_0	Empty tube velocity
V	Volume
$\dot{V}$	Volume flow rate
V_0	Volume of connecting tubes
V_cat	Volume of the catalyst after swelling
V_R	Volume of the reactor
w_i	True mass fraction of component i
$\tilde{w}_i$	Neutral overall mass fraction of component i
$\hat{w}_i$	Acidic overall mass fraction of component i
$\bar{w}^9_\mathrm{side}$	Side product level in recycle stream 9
x_i	True mole fraction of component i
x_i^0	Initial mole fraction of component i
x_i^EQ	True mole fraction of component i in chemical equilibrium
$\tilde{x}_i$	Neutral overall mole fraction of component i
$\hat{x}_i$	Acidic overall mole fraction of component i

Greek symbols

δ	Chemical shift
ϵ	Porosity of the packed bed
η	Dynamic viscosity
ν_cat	Specific volume of the catalyst after swelling
ν_{ij}	Stoichiometric coefficient of component i in reaction j
ξ_j	Molar extent of reaction j
$\dot{\xi}_j$	Molar extent per time of reaction j

$\xi_j(t^*)$	Cumulative molar extent of reaction j from time $t = 0$ till time t^*
$\dot{\xi}_j(m^*_{\text{cat}})$	Cumulative molar extent over time of reaction j between reactor entrance and position m^*_{cat}
ρ	Density
ρ_{cat}	Densityi of the catalyst after swelling
τ	Pseudo residence time
$\bar{\tau}$	Average residence time

Abbreviations

Bo	Bodenstein number
CPR	Catalyst-to-product ratio
DME	Dimethyl ether
FA	Formaldehyde
FOAC	Formic acid
GC	Gas chromatography
HF	Poly(oxymethylene) hemiformal
IC	Ion chromatography
ME	Methanol
MEFO	Methyl formate
MG	Poly(oxymethylene) glycol
NMR	Nuclear magnetic resonance
OAE	Poly(oxymethylene) dialkyl ether
OME	Poly(oxymethylene) dimethyl ether
PFR	Plug Flow Reactor
P&ID	Piping and instrumentation diagram
Re	Reynolds number
RTD	Residence time distribution
STY	Space–time yield
TMS	Tetramethylsilane
TRI	Trioxane
WA	Water

1 Introduction

The transportation sector is a major contributor of CO_2 emissions within the European Union (EU) (27% in 2020 [1]) and worldwide (14% in 2010 [2]). With the 2019 green deal, EU countries have set targets to reduce greenhouse gas emissions in the transportation sector by 55% until 2030 and 90% until 2050 compared to the 1990 emissions to fight climate change. However, despite the transition to electrified transportation, mobility still depends on easy-to-handle liquid fuels which are based on fossil resources for the most part [3]. Especially heavy-duty vehicles, which can hardly be electrified, and the existing fleet of passenger vehicles (in the EU and worldwide) need to be addressed to meet the ambitious goals.

Synthetic fuels can be produced from renewable energy and sustainable carbon sources and thus can contribute to the transition of the transportation sector [4]. Poly(oxymethylene) dimethyl ethers (OME), prominent representatives of oxygenated compounds, are a class of oligomers that are discussed as a neat alternative or blend component to diesel fuel [5–7]. Due to the high oxygen content and due to the lack of $C{-}C$ bonds (chemical formula $H_3C{-}(O{-}CH_2)_n{-}O{-}CH_3$), OME burn almost soot-free and, therefore, offer the potential to decrease local emissions of internal combustion engines, i.e., particulate matter and NO_x, substantially [6–9]. By using OME, air pollution could be reduced, as road transportation is one of the main emitters of harmful pollutants like soot and NO_x [10]. $OME_{3\text{–}5}$, oligomers with 3–5 oxymethylene groups, fit well into the diesel specification and can be used in conventional engines [8, 9]. In addition, OME feature favorable fuel properties, e.g., a larger cetane number and a higher combustion efficiency compared to conventional diesel fuel [11, 12], and could therefore simplify the engine system [13].

The production of OME is based on methanol as feedstock. Methanol is partly converted to formaldehyde, which is the monomer of the OME chains. The chains are capped either using methanol directly [14, 15] or using methanol derivatives such as dimethyl ether or methylal (OME_1) [16–20]. OME synthesis processes can be classified into water-free processes and water-tolerant processes [21, 22]. The water-free processes use dry monomeric formaldehyde, paraformaldehyde, or trioxane as formaldehyde source. Water-tolerant processes use methanol and formaldehyde solutions directly and include a water removal step in the OME process. The production of monomeric formaldehyde or the production of the intermediates paraformaldehyde and trioxane is therefore avoided. Industrial-size plants to produce OME currently rely on water-free processes for the most part [22]. However, water-tolerant processes offer greater potential for process efficiency [23–25]. In addition, the latter processes are based on the bulk chemicals methanol and formaldehyde, which are established in the value chain of the chemical industry and are therefore already available in large quantities.

Efforts are being made to further improve OME synthesis by fundamentally novel reaction pathways. Process intensification approaches to reduce the number of intermediate process steps are reported, e.g., the synthesis of OME_n ($n > 1$) from OME_1 and monomeric gaseous formaldehyde [26], the non-oxidative direct transformation of methanol to OME_1 [27], or the dehydrogenation of methanol yielding formaldehyde and hydrogen [28]. These examples illustrate the remarkable progress being made in the search for new reaction pathways and catalysts. Especially the developments regarding the non-oxidative conversion of methanol to formaldehyde offers substantially increased process efficiencies [29]. However, as comprehensively summarized in a recent review [30], further substantial improvements regarding the catalyst stability and the process design need to be made before scale-up to commercial scale is feasible.

The present work focuses on a water-tolerant process. In water-tolerant processes, OME are produced in slightly exothermic, acid-catalyzed equilibrium reactions [14, 15, 31]. Sulfuric acid [21], ion-exchange resins [14, 32], zeolites [15, 33], and solid superacids [21, 34] are reported to catalyze the formation reactions. The reaction temperature and pressure barely influence the chemical equilibrium due to the small reaction enthalpy and the liquid phase reaction, respectively [14, 15]. The chemical equilibrium and the associated reaction kinetics for several catalysts are already well-studied in literature and kinetic models are reported [15, 31]. Schmitz et al. [35] proposed a process concept that converts a feed solution comprising methanol and aqueous formaldehyde to $\mathrm{OME}_{3\text{–}5}$ and water as byproduct. The process consists of a tubular reactor, two distillation columns, and a water separation unit. The process concept is based on extensive experimental and modeling work addressing the reaction [14, 31], the distillation [36], and the water separation [37]. The present work builds on these findings and examines crucial issues for the realization of an industrial-size process. In addition, a generalized model to describe the reactions of oxymethylene ethers of various types is presented.

The process concept from Schmitz et al. [35] features large recycle streams due to the limiting chemical equilibrium. Depending on the process conditions, the reactor effluent contains roughly about 0.15 g/g of the desired product $\mathrm{OME}_{3\text{–}5}$. This leaves a major fraction of unreacted educts and OME with undesired chain lengths that need to be recycled. With these large inevitable internal process streams, potential side products can easily accumulate and adversely affect the industrial-size process. The formation of various side products is reported in the literature, but only qualitatively and not at conditions relevant for the process. In addition, the formation of side products has not been included in simulations of the OME process, so their implications for the process design are unknown. Chapter 2 summarizes the state of the art on side-product formation and presents experimental results on the formation of the side products methyl formate, formic acid, and trioxane. A reaction model was fitted to experimental data to describe the formation of the latter side products and implemented in a process simulation. The effects of side product formation on the process are extensively analyzed from different perspectives, and operating conditions for the reactor are proposed.

The formation of OME from methanol and formaldehyde has been extensively examined in the literature, mostly in batch reactors and from pure methanol and formaldehyde feed solutions. The process concept from Schmitz et al. [35] features, however, a continuous tubular fixed-bed reactor and substantial amounts of recycled OME in the reactor feed. Furthermore, little is known about the long-term usage of ion-exchange resins in OME synthesis, which is another crucial aspect of the large-scale continuous production of OME. In addition, despite the numerous studies regarding the industrial-scale production of OME [25, 29, 38, 39], a comprehensive examination of the particular challenges of large-scale reactor design, e.g., multiphase flow, heat and mass transfer, and pressure drop, is missing. This work closes this gap. A pilot plant including a continuous tubular fixed-bed reactor based on the process concept from Schmitz et al. [35] was built-up at the TUM Campus Straubing for Biotechnology and Sustainability [40]. Experimental results from reaction experiments with the tubular reactor are presented in Chapter 3. Furthermore, studies on the catalyst stability were performed. A reaction model was adjusted to experimental results and practical issues regarding the scale-up to an industrial-size reactor, e.g., heat transfer and pressure drop, are discussed.

Besides OME, other representatives of the general group of poly(oxymethylene) dialkyl ethers (OAE), i.e., oligomers with repeating oxymethylene groups (CH_2O) and terminating alkyl groups, like the ones derived from di-n-butyl ether, have gained increasing interest. They also show favorable properties when used in combustion engines [41, 42] and offer the potential of tuning physical and fuel properties not just by adjusting the chain length but also by exchanging the terminating alkyl groups [43]. This additional mutability is promising on the way to application-specific and optimized fuels [44–46]. However, many of the auspicious fuel candidates lack large-scale production processes. Quantitative knowledge about the respective formation reactions, i.e., systematic data let alone a model on the chemical equilibrium, is missing for essentially all OAE but OME. Chapter 4 closes this gap and presents a generalized model to describe the oligomerization and transacetalization (exchange of terminating groups) reactions in water-free systems containing OAE with various end groups and formaldehyde. Reaction experiments were performed and samples were analyzed by ^{13}C NMR spectroscopy. Chemical equilibrium constants were determined from the experimental results and compared to model values. Finally, the overall model performance was evaluated by comparison to experimental results of the present work.

2 Formation of Side Products and Implications for Process Design

2.1 State of the art

The formation of side products is crucial regarding the industrial production of OME. Various side products are reported in the literature. Baranowski et al. [47] investigated the formation of OME from trioxane and methylal catalyzed by H-ZSM-5 zeolites. Methyl formate was detected and a linear increase in concentration was observed over a reaction time of 4 h at 70 °C. Wu et al. [48] performed experiments with methylal and trioxane catalyzed by H-ZSM-5 zeolites with different Si/Al ratios. The Si/Al ratio determines the acidity of the catalyst. With rising acidity, the selectivity of methyl formate increases up to 47.3% after 45 min at 120 °C. The same group [49] examined the performance of a series of other zeolites for the reaction of methylal and trioxane at 30–150 °C. Selectivity of methyl formate and dimethyl ether increased significantly when the temperature exceeded 100 °C. In addition, the structural properties of the catalyst influenced the selectivities of main and side products. Burger et al. [16] investigated the formation of OME from methylal and trioxane catalyzed by ion-exchange resins Amberlyst 36 and Amberlyst 46. Dimethyl ether (DME) and methyl formate were detected as side products for Amberlyst 36 but not for Amberlyst 46 at temperatures up to 363 K. The different behavior was explained by the higher degree of sulfonation and the accompanying stronger acidity of the catalyst Amberlyst 36. Liu et al. [50] investigated the effect of reaction conditions when OME is synthesized from methylal and paraformaldehyde. They used the acidic ion-exchange resin NKC-9 as catalyst. Methyl formate, dimethyl ether, and formic acid were detected. High temperatures and long reaction times enhanced the formation of these side products. Furthermore, adding water to the originally water-free system resulted in a reduced formation of side products. Schmitz et al. [14] mentioned methyl formate and trioxane as side products during the formation of OME from methanol and aqueous formaldehyde solution catalyzed by Amberlyst 46. Oestreich et al. [15] examined the formation of OME from methanol and formaldehyde with different catalyst systems. Methyl formate and trioxane were detected as side products. The amount of methyl formate was found to be below 1%. Zhenova et al. [51] studied the formation of peroxides in a mixture of $OME_{3\text{–}5}$ and the pure substances under strong UV radiation and exposure to air. The rate of peroxide formation was comparable to a reference value of cyclopentyl methyl ether, which is said to have negligible peroxide formation [52].

To summarize, for a broad range of acidic catalysts, the side products methyl formate, dimethyl ether, formic acid, and trioxane have been found. Most of the above works discuss their formation in a qualitative way. Further, little is known about the quantitative formation of side products and the implications for OME process design.

This chapter presents experimental results regarding the formation of the side products methyl formate, formic acid, and trioxane. After briefly explaining the process and the chemical reactions in Section 2.2, experiments are presented (Section 2.3) based on which the kinetics of the side product formation were quantified and modeled. The model, which is described in Section 2.4, is based on an established model from Schmitz et al. [14, 31] and was extended by the side reactions. By embedding the developed model into a process simulation, implications of the side products on the steady-state operation of the process were derived. Purge streams and related product losses were quantified. The results of the reactions experiments and the process simulation are described in Section 2.5.

2.2 Fundamentals

2.2.1 Studied OME Process and Main Reactions

The studied process concept has been proposed by Schmitz et al. [35] and is presented in Figure 1.

Feed stream 1 is a liquid mixture of formaldehyde (FA, CH_2O), methanol (ME, H_3COH), and water (WA, H_2O). Such mixtures are reactive — formaldehyde forms oligomers with both water and methanol. According to reactions (I) and (II) poly(oxymethylene) glycols (MG_n, $HO(CH_2O)_nH$) are formed with water and poly(oxymethylene) hemiformals (HF_n, $HO(CH_2O)_nCH_3$) are formed with methanol (see reactions (III) and (IV)).

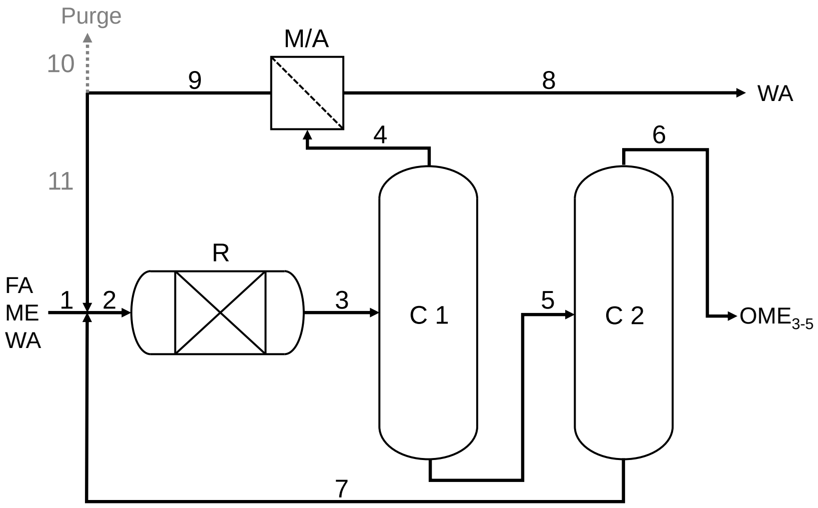

Figure 1: Flowsheet for the OME process following Schmitz et al. [35] R: Reactor unit; C1, C2: Distillation columns; M/A: Membrane or Adsorption unit.

$$FA + WA \rightleftharpoons MG_1 \qquad \text{(I)}$$

$$FA + MG_{n-1} \rightleftharpoons MG_n \qquad n \geq 2 \qquad \text{(II)}$$

$$FA + ME \rightleftharpoons HF_1 \qquad \text{(III)}$$

$$FA + HF_{n-1} \rightleftharpoons HF_n \qquad n \geq 2 \qquad \text{(IV)}$$

Reactions (I)–(IV) are reversible and fast even at neutral conditions without catalyst [53–55]. They can be assumed to be in chemical equilibrium in strongly acidic milieu [14, 31] and occur at all places in the process where formaldehyde is present together with methanol and/or water.

The reactor R is a fixed-bed reactor filled with catalyst Amberlyst 46 and operated at 343.15 K [35]. Inside, OME with various chain lengths are either produced from hemiformals (see reactions (V) and (VI)) or from the chain propagation mechanism according to reactions (VII) and (VIII) [31].

$$HF_1 + ME \xrightleftharpoons{H^+} OME_1 + WA \qquad \text{(V)}$$

$$HF_n + ME \xrightleftharpoons{H^+} OME_n + WA \qquad n \geq 2 \qquad \text{(VI)}$$

$$FA + OME_1 \xrightleftharpoons{H^+} OME_2 \qquad \text{(VII)}$$

$$FA + OME_{n-1} \xrightleftharpoons{H^+} OME_n \qquad n \geq 3 \qquad \text{(VIII)}$$

OME are stable at neutral conditions and reactions (V)–(VIII) occur only in the reactor R, where catalyst is present. The reactor effluent is worked up in a direct distillation sequence. The middle-boiling fraction (stream 6) contains the $OME_{3\text{–}5}$ product. The heavy-boiling fraction (stream 7) of long-chain OME_n with $n \geq 6$ is recycled to the reactor. The low-boiling fraction (stream 4) contains unreacted educts and short-chain OME_n with $n \leq 3$. It is also recycled back to the reactor after water (stream 8) is removed in a membrane or adsorption unit. Water is a stoichiometric side product of the main reactions and has to be removed.

2.2.2 Side Products

Apart from the above main reactions, several side reactions may occur in the reactor leading to several side products. In the experiments of this work with the catalyst Amberlyst 46, three of them were identified: trioxane, methyl formate, and formic acid.

Different reaction mechanisms for producing trioxane (TRI, $(CH_2O)_3$) are proposed in the literature [16, 17, 56–58]. It could, for example, be formed by decomposition of OME_4 to OME_1 and trioxane (reaction (IXa)) [16, 17], by dehydration of MG_3 (reaction (IXb)) [57, 58], or by combination of three monomeric formaldehyde units (reaction (IXc)) [56]. No matter which mechanism is considered, the trioxane formation is quite limited due to a favorable chemical equilibrium [56, 59].

$$\mathrm{OME_4} \xrightleftharpoons{\mathrm{H^+}} \mathrm{TRI} + \mathrm{OME_1} \tag{IXa}$$

$$\mathrm{MG_3} \xrightleftharpoons{\mathrm{H^+}} \mathrm{TRI} + \mathrm{WA} \tag{IXb}$$

$$3\,\mathrm{FA} \xrightleftharpoons{\mathrm{H^+}} \mathrm{TRI} \tag{IXc}$$

The formation of methyl formate (MEFO, $HCOOCH_3$), the methyl ester of formic acid, is described as combination of two formaldehyde molecules [16]

$$2\,\mathrm{FA} \xrightarrow{\mathrm{H^+}} \mathrm{MEFO} \tag{X}$$

This so-called Tishchenko-reaction is catalyzed by Lewis-acids [60] and is described as both reversible [61, 62] and irreversible [16, 19] in the literature. Methyl formate could also be formed from the reversible acid-catalyzed esterification of formic acid (FOAC, HCOOH) with methanol [63, 64]

$$\mathrm{FOAC} + \mathrm{ME} \xrightleftharpoons{\mathrm{H}^+} \mathrm{MEFO} + \mathrm{WA} \tag{XI}$$

In this case, formic acid would be formed prior to methyl formate from formaldehyde and water in a Cannizzaro-reaction

$$2\,\mathrm{FA} + \mathrm{WA} \xrightarrow{\mathrm{H}^+/\mathrm{OH}^-} \mathrm{FOAC} + \mathrm{ME} \tag{XII}$$

Strong bases and Lewis acids are reported to catalyze reaction (XII) [65, 66]. The reversability of reaction (XII) is, again, described ambigiously in the literature [57, 66].

2.2.3 True Composition and Overall Composition

In working with reactive formaldehyde systems, it is common to work with overall and true compositions [16, 31, 54, 55]. In this work, three different ways to describe the composition are used, which are explained in Figure 2. True mole fractions (x_i) and true mass fractions (w_i) quantify all chemical species described above, including the OME, the MG, and the HF. Neutral overall mole fractions ($\tilde{x}_i$) and neutral overall mass fractions ($\tilde{w}_i$) are obtained theoretically when all MG and HF, which are unstable at neutral conditions, are completely decomposed into formaldehyde, water, and methanol. Acidic overall mole fractions ($\hat{x}_i$) and acidic overall mass fractions ($\hat{w}_i$) are obtained theoretically when all MG, HF, and additionally all OME, which are unstable at acidic conditions, have completely reacted to formaldehyde, water, and methanol. To calculate the neutral and acidic overall composition, the side products (TRI, MEFO, FOAC) are considered as stable because their reactions are very slow compared to the main reactions.

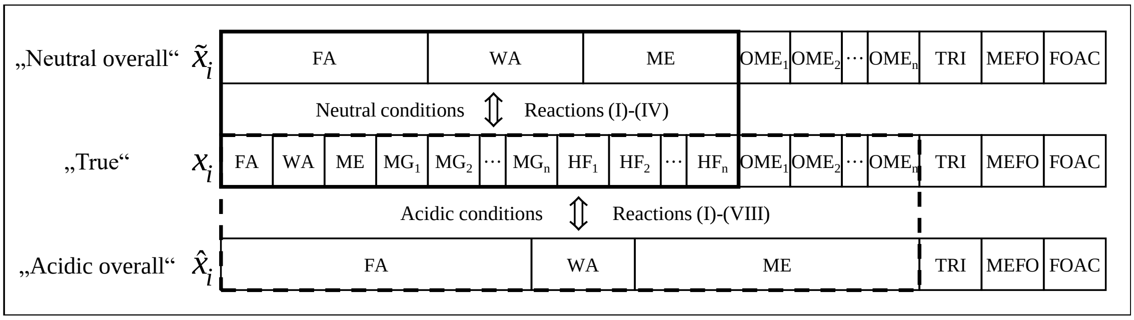

Figure 2: Scheme to visualize the true and overall compositions used in the present work.

Since one OME molecule requires one molecule of water for reacting to methanol and formaldehyde, the acidic overall mole/mass fractions of water may become negative when OME are present. For example, pure OME_1 expressed in acidic overall mole fractions is $\begin{pmatrix} \hat{x}_{\mathrm{FA}} & \hat{x}_{\mathrm{WA}} & \hat{x}_{\mathrm{ME}} \end{pmatrix} = \begin{pmatrix} 0.5 & -0.5 & 1 \end{pmatrix}$ mol/mol.

The true composition is used in the model. The neutral overall composition is obtained in the analysis of the reactor samples. The acidic overall composition is used in the experimental planning, since it fully specifies the true composition in the chemical equilibrium of the main reactions (I)–(VIII) at a given temperature. (The pressure dependency of the chemical equilibrium is disregarded due to the liquid phase). The mathematical expressions for the calculation of the neutral overall and acidic overall compositions from the true composition are given in the Appendix A.1.

2.3 Experiments

2.3.1 Chemicals and Catalyst

Paraformaldehyde (>0.95 g/g) and methylal (>0.99 g/g) were purchased from Sigma-Aldrich. Methanol (>0.999 g/g) was purchased from Merck. Chemicals were used without further purification. Ultrapure water was produced with a PURELAB Classic water purification system from ELGA. Formaldehyde solutions were prepared by dissolving paraformaldehyde in a solvent. Preparation methods slightly differed for negative and positive acidic overall water contents of the desired solutions, see Table 1 for details. Paraformaldehyde was dissolved in the solvent by stirring at elevated temperatures under reflux. A few drops of base were added to the mixture to enhance the dissolving process. After stirring for typically two days, residues of undissolved paraformaldehyde were removed from the solution through filtration.

Table 1: Conditions for the preparation of formaldehyde solutions used in the experiments KIN-S1–KIN-S6, depending on the desired acidic overall mass fraction of water $\hat{w}_{\mathrm{WA}}$.

	$\hat{w}_{\mathrm{WA}} < 0$ [a]	$\hat{w}_{\mathrm{WA}} > 0$
solvent	methylal + methanol	water + methanol
T / K	313.15	333.15
base	sodium methoxide	sodium hydroxide

[a] As outlined in Section 2.2.3, $\hat{w}_{\mathrm{WA}}$ can take negative values.

The ion-exchange resin Amberlyst 46, provided by DuPont, was used as the catalyst for all experiments of this work. The catalyst was shipped in wet form. It was dried overnight in a vacuum oven at 343.15 K and <10 mbar before use.

2.3.2 Analysis

The neutral overall mass fractions of formaldehyde and water were determined by the sodium sulfite method [56] and Karl-Fischer titration, respectively. The titrations were performed at least three times per sample with standard deviations typically below 1%. The neutral overall mass fractions of methanol, OME, methyl formate, and trioxane were quantified by gas chromatography (GC) with 1,4-dioxane as internal standard (Thermo Fisher Trace 1310, flame ionization detector, detector temperature: 250 °C, injection temperature: 240 °C, helium as carrier gas, Split 1:80, Restek Rtx-Wax column (ID: 0.32 mm, L: 30 m)). Pure substances were used for calibrating methanol, OME_1 to OME_4, trioxane, and methyl formate. The calibration curves for OME_5 and OME_6 were extrapolated from OME_1 to OME_4. OME with $n > 6$ were not detected with the applied methods.

The mass fraction of formic acid was obtained from ion chromatography (IC) analysis (Metrohm 930 Compact IC Flex, Metrosep A Supp 5 250/4.0 with an aqueous solution of 3.2 mmol/L sodium carbonate and 1.0 mmol/L sodium hydrogen carbonate as eluent). IC measurements yield the total amount of formates in the solution (formic acid + methyl formate). Thus, the mass fraction of formic acid was obtained by subtracting the mass fraction of methyl formate (obtained from GC analysis) from the total amount of formates (obtained from IC analysis).

After the reaction experiment, the resulting solution was separated from the catalyst and tested for peroxides (Dosatest peroxide test strips 25, 0–25 mg/, VWR). All tests were negative. Gravimetically prepared test samples containing the pure components were analyzed to determine the analytical error. The mass fractions of formic acid were obtained by combining two analytical methods (GC and IC) resulting in a relative error that was estimated to be <5%. Relative deviations were below 5% for methanol and below 2% for all other components. The sum of all overall mass fractions was between 0.97 and 1.03 g/g for all samples, thereby confirming reliable analysis methods. All mass fractions shown in this work were normalized to a sum of 1 g/g by proportional weighting.

The specific catalyst activity in terms of H^+-loading, i.e., the amount of acid sites per dry mass, was obtained after every single experiment by determining the acid sites by acid-base titration. In the following, the short expression catalyst activity is used. The method is an adaption from von Harbou et al. [67] and is briefly described in the following. The catalyst was rinsed thoroughly with water to remove organic material. Then, the catalyst sample (typically 1 g) was given into water and a known volume (typically 5 ml) of sodium hydroxide (c = 1 mol/L) was added. The acid sites of the catalyst partially neutralize the base. The solution was then titrated with hydrochloric acid (c = 1 mol/L) to neutral pH and the number of acid sites was determined based on the consumption of hydrochloric acid. The catalyst was collected and dried in the vacuum oven at 343.15 K overnight to measure the dry mass of the catalyst. The catalyst samples were analyzed twice after each experiment with a standard deviation typically below 5%.

2.3.3 Apparatus und Experimental Procedure

The reaction experiments were carried out in a 0.5 L stainless steel batch reactor from Büchi. A schematic overview is given in Figure 3. The temperature inside the double jacketed reactor was controlled with a thermostat (FP50-ME, Julabo) combined with a Pt100 resistance thermometer (accuracy ±0.1 K). The pressure inside the reactor was measured with a pressure transmitter (WIKA P-30, 0–100 barg, accuracy ≤ ±0.1%). A propeller stirrer was used for mixing the reaction mixture. Samples were taken through a riser pipe and cooled by a double pipe heat exchanger to prevent them from evaporating when expanded to atmospheric pressure. A mesh out of stainless steel, attached around the opening of the riser pipe, prevented the catalyst from entering the sampling tube. A flexible tube (material: PTFE) in combination with a clamp was used for storing the catalyst separately from the liquid before the reaction was initiated by releasing the catalyst into the liquid mixture.

All experiments with the batch reactor in this chapter were carried out according to the following procedure. The tube was filled with a weighed amount of dry catalyst and mounted on top of the reactor. The educt mixture was filled in the reactor and the reactor was closed pressure-tight. Remaining oxygen in the reactor was removed through multiple flushing with nitrogen. The reactor was pressurized with nitrogen and the temperature was set. Since the pressure has little effect on the reaction taking place in the liquid phase, no special care was taken regarding the absolute pressure value. Nevertheless, the pressure was sufficient in all experiments to avoid boiling. To ensure a constant starting temperature, the educt mixture was continuously stirred and thermostated overnight. A sample was taken before removing the clamp of the catalyst tube. The catalyst was added to the mixture and the reactions commenced.

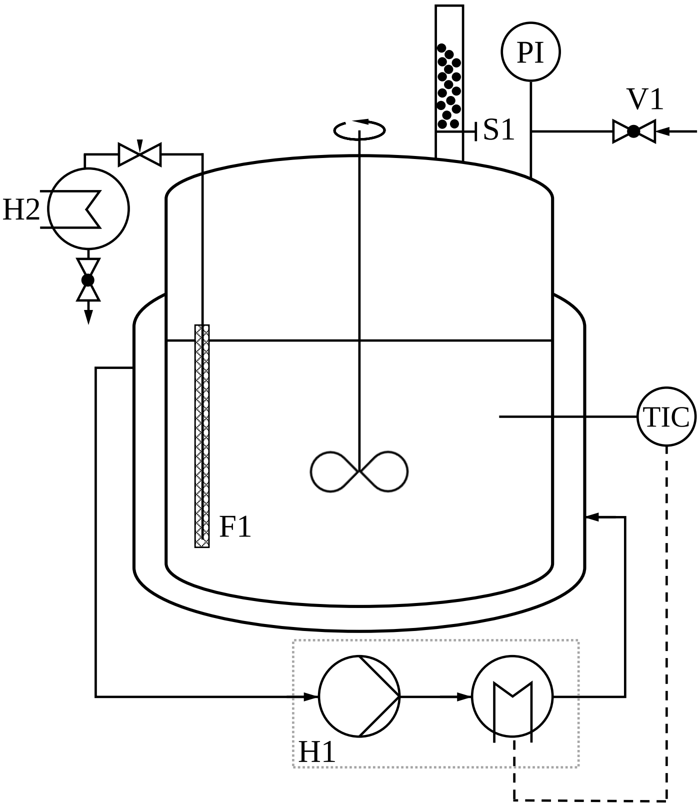

Figure 3: Schematic of the batch reactor. H1: Thermostat. H2: Sample cooling. TIC: Temperature measurement and control. PI: Pressure measurement. V1: Inlet valve. S1: Catalyst supply with clamp. F1: Filter around sample line.

The influence of the stirrer speed on the reaction conversion was tested in preliminary experiments. No significant difference between results was observed when the stirrer speed was set to 250 and 350 rpm. Hence, the stirrer speed was set to 350 rpm for all experiments. Recurrent sampling was carried out over the complete reaction duration of typically five to six days. After finishing the experiment, the catalyst was separated from the reaction mixture by filtration. All samples and the catalyst were carefully analyzed promptly after the end of each run.

2.3.4 Experimental Program

Four parameters were identified that influence the reaction progress. The chemical equilibrium of the main reactions is fully specified by the acidic overall mass ratio of formaldehyde to methanol and the acidic overall mass fraction of water. In addition, the mass ratio of catalyst to initial liquid mixture $m_{\text{cat}}/m_{\text{L,0}}$ and the temperature T both influence the reaction kinetics. Table 2 summarizes the performed experiments and the respective values for the four parameters.

Table 2: Overview of the reaction conditions and influence parameters in the kinetic experiments KIN-S1–KIN-S6.

	$\hat{m}_{\text{FA}}/\hat{m}_{\text{ME}}$ g/g	$\hat{w}_{\text{WA}}$ g/g	$m_{\text{cat}}/m_{\text{L,0}}$ g/g	T K	$m_{\text{L,0}}$ g
KIN-S1	0.88	−0.067	0.024	343.15	370.3
KIN-S2	0.92	−0.064	0.025	358.15	353.8
KIN-S3	0.86	0.041	0.020	358.15	462.5
KIN-S4	0.58	−0.072	0.025	358.15	347.7
KIN-S5	0.94	−0.062	0.023	373.15	393.4
KIN-S6	0.90	−0.065	0.033	358.15	400.4

Experiment KIN-S1 is similar to the reactor conditions proposed in the OME production process by Schmitz et al. [35]. Since the aim of this work was to investigate the formation of irreversible side products at process-relevant conditions, KIN-S1 was chosen as the base case. The four mentioned influence parameters were varied in a star-shaped experimental design to isolate their effects. The temperature was varied twice. This resulted in a total of six experiments.

2.4 Modeling and Simulation

2.4.1 Chemical Equilibrium and Reaction Kinetics

A pseudo-homogeneous model was chosen to describe the reaction kinetics of the formation of OME and side products. This approach has shown good results in work with heterogeneous acidic catalysts like ion-exchange resins [68] and has already been used to model OME reactions [15, 31, 69]. The reaction kinetic model of the main reactions (I)–(VIII) is adapted from Schmitz et al. [31] and extended by the formation of trioxane, methyl formate and formic acid. The pseudo-homogeneous model assumes that the catalyst active sites are freely accessible to all components in the bulk liquid. Possible mass transfer limitations are not explicitly taken into account but are considered in the reaction kinetic constants.

The chemical equilibrium of reactions (I)–(IX) and reaction (XI) is described using mole-fraction based chemical equilibrium constants.

$$K_{\mathrm{I}}(T) = \frac{x_{\mathrm{MG}_1}^{\mathrm{EQ}}}{x_{\mathrm{FA}}^{\mathrm{EQ}} \cdot x_{\mathrm{WA}}^{\mathrm{EQ}}} \tag{1}$$

$$K_{\mathrm{II},n}(T) = \frac{x_{\mathrm{MG}_n}^{\mathrm{EQ}}}{x_{\mathrm{FA}}^{\mathrm{EQ}} \cdot x_{\mathrm{MG}_{n-1}}^{\mathrm{EQ}}} \qquad n \geq 2 \tag{2}$$

$$K_{\mathrm{III}}(T) = \frac{x_{\mathrm{HF}_1}^{\mathrm{EQ}}}{x_{\mathrm{FA}}^{\mathrm{EQ}} \cdot x_{\mathrm{ME}}^{\mathrm{EQ}}} \tag{3}$$

$$K_{\mathrm{IV},n}(T) = \frac{x_{\mathrm{HF}_n}^{\mathrm{EQ}}}{x_{\mathrm{FA}}^{\mathrm{EQ}} \cdot x_{\mathrm{HF}_{n-1}}^{\mathrm{EQ}}} \qquad n \geq 2 \tag{4}$$

$$K_{\mathrm{V}}(T) = \frac{x_{\mathrm{OME}_1}^{\mathrm{EQ}} \cdot x_{\mathrm{WA}}^{\mathrm{EQ}}}{x_{\mathrm{HF}_1}^{\mathrm{EQ}} \cdot x_{\mathrm{ME}}^{\mathrm{EQ}}} \tag{5}$$

$$K_{\mathrm{VI},n}(T) = \frac{x_{\mathrm{OME}_n}^{\mathrm{EQ}} \cdot x_{\mathrm{WA}}^{\mathrm{EQ}}}{x_{\mathrm{HF}_n}^{\mathrm{EQ}} \cdot x_{\mathrm{ME}}^{\mathrm{EQ}}} \qquad n \geq 2 \tag{6}$$

$$K_{\mathrm{VII}}(T) = \frac{x_{\mathrm{OME}_2}^{\mathrm{EQ}}}{x_{\mathrm{FA}}^{\mathrm{EQ}} \cdot x_{\mathrm{OME}_1}^{\mathrm{EQ}}} \tag{7}$$

$$K_{\mathrm{VIII},n}(T) = \frac{x_{\mathrm{OME}_n}^{\mathrm{EQ}}}{x_{\mathrm{FA}}^{\mathrm{EQ}} \cdot x_{\mathrm{OME}_{n-1}}^{\mathrm{EQ}}} \qquad n \geq 3 \tag{8}$$

$$K_{\mathrm{IXa}}(T) = \frac{x_{\mathrm{TRI}}^{\mathrm{EQ}} \cdot x_{\mathrm{OME}_1}^{\mathrm{EQ}}}{x_{\mathrm{OME}_4}^{\mathrm{EQ}}} \tag{9}$$

$$K_{\mathrm{IXb}}(T) = \frac{x_{\mathrm{TRI}}^{\mathrm{EQ}} \cdot x_{\mathrm{WA}}^{\mathrm{EQ}}}{x_{\mathrm{MG}_3}^{\mathrm{EQ}}} \tag{10}$$

$$K_{\mathrm{XI}}(T) = \frac{x_{\mathrm{MEFO}}^{\mathrm{EQ}} \cdot x_{\mathrm{WA}}^{\mathrm{EQ}}}{x_{\mathrm{FOAC}}^{\mathrm{EQ}} \cdot x_{\mathrm{ME}}^{\mathrm{EQ}}} \tag{11}$$

The nomenclature of the subscripts of the equilibrium constants K_j follows the numbering of the reactions and the oligomer chain length n, if necessary. Note that eqs (1)–(11) represent definitions of the chemical equilibrium constants that are consequently only valid in the chemical equilibrium. As the model describes the reaction kinetics, the chemical equilibrium is not always reached. Therefore, these equations are not implemented in the kinetic model. Instead, the chemical equilibrium constants of all reactions are calculated by the van't Hoff equation

$$\ln K_j(T) = A_j + \frac{B_j}{T/\mathrm{K}} \tag{12}$$

with the two parameters A_j and B_j. The values of the parameters for reactions (I)-(IX) are taken from literature [14, 15, 54] and are listed in Table 3. The mole fraction-based constant K_{XI} has been measured over a broad range of temperatures and compositions in the literature. It scatters strongly with composition, cf. Appendix. Since no data on the reaction in OME systems are available, the parameters are fitted to the experimental data of the present work. (Using an activity-based equilibrium constant K_{XI} and the UNIFAC [70, 71] activity coefficient model did not remove the composition dependency and was thus no longer followed.) The fitted values of the parameters are given in Table 3.

In general, reaction rates r_j are defined using the number of active sites as base

$$r_j = \frac{\mathrm{d}\xi_j}{\mathrm{d}t} \cdot \frac{1}{m_{\mathrm{cat}} \cdot c_{\mathrm{cat}}^{\mathrm{H}^+}} \quad ; \quad [r_j] = \frac{\mathrm{mol}}{\mathrm{s} \cdot \mathrm{mol}_{\mathrm{cat}}^{\mathrm{H}^+}} \tag{13}$$

with $c_{\mathrm{cat}}^{\mathrm{H}^+}$ as the specific catalyst activity, m_{cat} as the mass of dry catalyst, and ξ_j as the molar extent of reaction j.

Two groups of reactions with substantially different reaction rates are included in the model. The reactions (I)-(IV) quickly proceed even at neutral conditions without a catalyst [31, 53, 54]. In addition, the experimental results (see below) revealed that the esterification reaction (XI) of formic acid to methyl formate is very fast and can be assumed to be in chemical equilibrium under the given conditions. This finding is

Table 3: Parameters for the calculation of the mole fraction-based chemical equilibrium constants K_j using the correlation $\ln K_j = A_j + B_j/(T/\mathrm{K})$.

	A_j	B_j	Reference
K_{I}	−2.325	2579	Hahnenstein et al. [54]
$K_{\mathrm{II},2}$	−2.311	3140	
$K_{\mathrm{II},n} (n \geq 3)$	−2.433	3039	
K_{III}	−1.902	3512	
$K_{\mathrm{IV},n} (n \geq 2)$	−2.250	3009	
K_{V}	0.8147	340.3	Schmitz et al. [14]
$K_{\mathrm{VI},2}$	0.6489	361.1	
$K_{\mathrm{VI},3}$	0.4831	381.9	
$K_{\mathrm{VI},4}$	0.3173	402.8	
$K_{\mathrm{VI},5}$	0.1515	423.6	
$K_{\mathrm{VI},6}$	−0.01426	444.4	
$K_{\mathrm{VI},7}$	−0.1801	465.3	
$K_{\mathrm{VI},8}$	−0.3459	486.1	
K_{VII}	−2.415	3030	
K_{VIII}	−2.415	3030	
K_{IXa}	0.5583	−872.5	Oestreich et al. [15]
K_{IXb}	0.2400	−506.3	
K_{XI}	0.06455	359.0	This work

consistent with the literature [72–75]. The composition dependence of their rates r_{I}–$r_{\mathrm{IV},n}$ and r_{XI} is described in eqs (14)–(18)

$$r_{\mathrm{I}} = k_{\mathrm{I}} \left(x_{\mathrm{FA}} x_{\mathrm{WA}} - \frac{1}{K_{\mathrm{I}}(T)} x_{\mathrm{MG}_1} \right) \tag{14}$$

$$r_{\mathrm{II},n} = k_{\mathrm{II},n} \left(x_{\mathrm{FA}} x_{\mathrm{MG}_{n-1}} - \frac{1}{K_{\mathrm{II},n}(T)} x_{\mathrm{MG}_n} \right) \qquad n \geq 2 \tag{15}$$

$$r_{\mathrm{III}} = k_{\mathrm{III}} \left(x_{\mathrm{FA}} x_{\mathrm{ME}} - \frac{1}{K_{\mathrm{III}}(T)} x_{\mathrm{HF}_1} \right) \tag{16}$$

$$r_{\mathrm{IV},n} = k_{\mathrm{IV},n} \left(x_{\mathrm{FA}} x_{\mathrm{HF}_{n-1}} - \frac{1}{K_{\mathrm{IV},n}(T)} x_{\mathrm{HF}_n} \right) \qquad n \geq 2 \tag{17}$$

$$r_{\mathrm{XI}} = k_{\mathrm{XI}} \left(x_{\mathrm{FOAC}} x_{\mathrm{ME}} - \frac{1}{K_{\mathrm{XI}}(T)} x_{\mathrm{MEFO}} x_{\mathrm{WA}} \right) \tag{18}$$

The respective reaction rate constants k_j are set to $k_{\mathrm{I}} = k_{\mathrm{II},n} = k_{\mathrm{III}} = k_{\mathrm{IV},n} = k_{\mathrm{XI}} = 10^8$ to model them as essentially infinitely fast reactions. (Increasing this value did not change the model results.) The reactions (I)-(IV) and (XI) are therefore in quasi-equilibrium.

By contrast, the formation of OME is kinetically controlled, and thus rate-determining. This second group of reactions (V)-(VIII) is modeled with finite temperature-dependent reaction rate constants according to the following equations

$$r_{\mathrm{V}} = k_{\mathrm{A}}(T)\left(x_{\mathrm{HF}_1}x_{\mathrm{ME}} - \frac{1}{K_{\mathrm{V}}(T)}x_{\mathrm{OME}_1}x_{\mathrm{WA}}\right) \tag{19}$$

$$r_{\mathrm{VI},n} = k_{\mathrm{A}}(T)\left(x_{\mathrm{HF}_n}x_{\mathrm{ME}} - \frac{1}{K_{\mathrm{VI},n}(T)}x_{\mathrm{OME}_n}x_{\mathrm{WA}}\right) \qquad n \geq 2 \tag{20}$$

$$r_{\mathrm{VII}} = k_{\mathrm{G}}(T)\left(x_{\mathrm{FA}}x_{\mathrm{OME}_1} - \frac{1}{K_{\mathrm{VII}}(T)}x_{\mathrm{OME}_2}\right) \tag{21}$$

$$r_{\mathrm{VIII},n} = k_{\mathrm{G}}(T)\left(x_{\mathrm{FA}}x_{\mathrm{OME}_{n-1}} - \frac{1}{K_{\mathrm{VIII},n}(T)}x_{\mathrm{OME}_n}\right) \qquad n \geq 3 \tag{22}$$

The mole fraction-based chemical equilibrium constants $K_{j,n}$ in eqs (19)–(22) depend on the oligomer chain length n and are known, cf. Table 3. The rate constants do not depend on the chain length. Thus, they are aggregated to the rate constant k_{A} for acetalization reactions and the rate constant k_{G} for growth reactions [31]. The temperature dependency of the rate constants is expressed by the Arrhenius equation and given in Table 4.

Table 4: Parameters for the calculation of the reaction rate constants k_j using the correlation $\ln(k_j/(\mathrm{mol}/(\mathrm{s}\cdot\mathrm{mol}_{\mathrm{cat}}^{\mathrm{H}^+}))) = a_j + b_j/(T/\mathrm{K})$.

	a_j	b_j	Reference
k_{A}	19.96	−6670	Schmitz et al. [31]
k_{G}	31.05	−8907	
k_{IXa}	33.29	−13749	This work
k_{IXb}	20.34	−8875	
k_{X}	27.67	−9528	

The formation of trioxane is modeled as an additional kinetically controlled reaction. The decomposition of OME_4 (reaction (IXa)) is chosen as the model reaction for the batch reactor experiments because all participating reactants are quantified directly. This leads to a smaller statistical error caused by model calculations and facilitates comparison to literature even with water-free systems.

Using reaction (IXb) or reaction (IXc) instead of reaction (IXa) did not improve the description of the experimental profiles from the experiments with the batch reactor. However, using the resulting model to describe the tubular reactor in the process simulation reveals an influence exerted by the chosen formation mechanism. This is attributed to the qualitatively different concentration profiles of the respective components over the reactor. The mass fraction of OME_4 changes strongly within the reactor, whereas MG_3 and FA stay roughly constant. In order to cover both described cases, process simulations are performed either with reaction (IXa) or reaction (IXb) and results are compared. The rates of both reactions are modeled by the following equations

$$r_{\mathrm{IXa}} = k_{\mathrm{IXa}}(T)\left(x_{\mathrm{OME}_4} - \frac{1}{K_{\mathrm{IXa}}(T)} x_{\mathrm{OME}_1} x_{\mathrm{TRI}}\right) \tag{23a}$$

$$r_{\mathrm{IXb}} = k_{\mathrm{IXb}}(T)\left(x_{\mathrm{MG}_3} - \frac{1}{K_{\mathrm{IXb}}(T)} x_{\mathrm{WA}} x_{\mathrm{TRI}}\right) \tag{23b}$$

The equilibrium constants K_{IXa} and K_{IXb} were calculated from literature data [15, 54], cf. Table 3 for the result and Appendix A.3 for details. The rate constants k_{IXa} and k_{IXb} are given in Table 4 and were fitted to experimental data of the present work.

The experimental profiles of the present work reveal that the concentrations of methyl formate and formic acid increase linearly without saturation observed. Thus, they are formed at constant rates during the experiments. This indicates that there is no reverse reaction or that the equilibrium of the formation reactions is far away. Since methyl formate and formic acid are interlinked via the fast reaction (XI), it is not possible to tell from the experiments, whether methyl formate is formed initially via reaction (X), whether formic acid is formed initially via reaction (XII), or whether both these reactions occur in significant rates. Since the formation of methyl formate is observed quite prominently in the literature, even in systems without water or methanol, reaction (X) was used in the model and reaction (XII) was left out for simplicity's sake. Adding reaction (XII) to the model did not improve the fit to the experimental data. The rate of reaction (X) is given by

$$r_{\mathrm{X}} = k_{\mathrm{X}}(T) \cdot (x_{\mathrm{FA}})^2 \tag{24}$$

The rate constant k_{X} is given in Table 4 and was fitted to experimental data of the present work.

2.4.2 Reactor Models

Batch Stirred-Tank Reactor A perfectly mixed reactor is assumed in the model. Therefore, concentration and temperature gradients in the reactor are disregarded. In addition, The time-dependent amount $n_i(t^*)$ of any true component i in the batch reactor is described by the material balance

$$n_i(t^*) = \tilde{n}_i(t = 0) + \sum_{j=1}^{N_\mathrm{R}} \nu_{ij} \cdot \xi_j(t^*) \tag{25}$$

with $\tilde{n}_i(t = 0)$ as the initial overall amount of component i, N_R as the number of reactions, ν_{ij} as the stoichiometric coefficient of component i in reaction j, and $\xi_j(t^*)$ as the cumulative molar extent of reaction j from time $t = 0$ till time t^*. The latter is calculated by

$$\xi_j(t^*) = m_\mathrm{cat} \cdot c_\mathrm{cat}^{\mathrm{H}^+} \cdot \int_0^{t^*} r_j \, \mathrm{d}t \tag{26}$$

Combining the latter two equations with eqs (12)–(24) to describe the concentration profiles over time in the batch reactor, results in a system of differential and algebraic equations that is solved numerically.

Continuous Tubular Reactor An ideal plug flow reactor (PFR) is assumed. Therefore, axial diffusion and radial concentration gradients are disregarded. Additionally, isothermal conditions throughout the reactor are assumed. The material balance

$$\dot{n}_i(m_\mathrm{cat}^*) = \dot{n}_i(m_\mathrm{cat} = 0) + \sum_{j=1}^{N_\mathrm{R}} \nu_{ij} \cdot \dot{\xi}_j(m_\mathrm{cat}^*) \tag{27}$$

describes the molar flow rate $\dot{n}_i(m_\mathrm{cat}^*)$ of any true component i at the position m_cat^* in the reactor under steady-state conditions. The already passed dry mass of catalyst m_cat is used as variable to define the position in the reactor (see Figure 4).

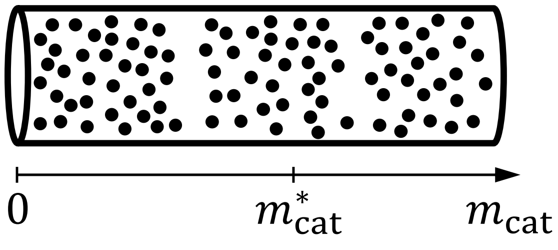

Figure 4: Scheme of the tubular reactor model.

According to eq (27), the molar flow rate $\dot{n}_i(m_\mathrm{cat}^*)$ at position m_cat^* is calculated from the entering molar flow rate $\dot{n}_i(m_\mathrm{cat} = 0)$, the number of reactions, the stoichiometric coefficients, and the cumulative molar extent over time $\dot{\xi}_j(m_\mathrm{cat}^*)$ of reaction j between reactor entrance and position m^*_{cat}. The latter is calculated by

$$\dot{\xi}_j(m^*_{\text{cat}}) = \int_0^{m^*_{\text{cat}}} c^{\text{H}^+}_{\text{cat}} \cdot r_j(m_{\text{cat}})\,\text{d}m_{\text{cat}} \tag{28}$$

Applying eqs (12)–(24) in combination with the latter two equations to describe the concentration profiles of each component i throughout the reactor, results in a system of differential and algebraic equations that is solved numerically.

2.4.3 Simulation of the OME Process

The process described in Section 2.2.1 along Figure 1 is simulated in steady-state. The feed comprises formaldehyde ($w^{\text{Feed}}_{\text{FA}}$ = 0.55 g/g), methanol ($w^{\text{Feed}}_{\text{ME}}$ = 0.35 g/g), and water($w^{\text{Feed}}_{\text{WA}}$ = 0.10 g/g) (stream 1). The reaction unit is modeled as PFR following the description above. The distillation units are modeled as ideal splitters for all components besides OME$_3$. It is assumed in the simulation that 30% of the OME$_3$ entering column 1 (stream 3) leaves the column through the top (stream 4). The rest leaves in stream 5. The membrane or adsorption unit is modeled as an ideal splitter with the specification that 85% of the water entering the unit is separated. This assumption is motivated by the results of Schmitz et al. [35]

Since methyl formate and formic acid are formed irreversibly in the reactor, an outlet is required. The standard boiling points for TRI, MEFO, and FOAC are $T_{\text{b,TRI}}$ = 388 K [5], $T_{\text{b,MEFO}}$ = 305 K [76], and $T_{\text{b,FOAC}}$ = 374 K [76], respectively. Compared to the standard boiling points of OME$_2$ ($T_{\text{b,OME}_2}$ = 378 K) [5] and OME$_3$ ($T_{\text{b,OME}_3}$ = 429 K) [5], it is assumed that all three side products leave column 1 through the distillate. Therefore, they would accumulate in the cycle of streams 2, 3, 4, 9 with their highest concentration in stream 9. To create the necessary outlet, parts of stream 9 are purged.

The resulting process simulation has three degrees of freedom left to specify: the reactor temperature, the mass of dry catalyst in the reactor, and the level of side products in recycle stream 9. The latter determines the size of the purge stream via the overall material balance of the side products. To quantify the level of side products in stream 9, the combined mass fraction $\bar{w}^9_{\text{side}}$ of methyl formate and formic acid is used. To keep the results at different reactor temperatures comparable, the mass of dry catalyst is always chosen so that the production of OME$_4$ in a single reactor pass is 90% of the OME$_4$ possible in the chemical equilibrium of the main reactions. Thus, two parameters are varied in the simulation studies, the reactor temperature T_{R} and the side product level $\bar{w}^9_{\text{side}}$. For convenient scaling, all simulation results are reported for a product rate

$\dot{m}_{\text{product}}$ of 1 kg/h. The mass of dry catalyst is reported using the catalyst-to-product ratio CPR (the inverse of the space–time yield, STY)

$$\text{CPR} = \frac{1}{\text{STY}} = \frac{m_{\text{cat}}}{\dot{m}_{\text{product}}} \tag{29}$$

2.4.4 Implementation and Parameter Estimation

All simulations that are described in this chapter were carried out using the software gProms Model Builder V 5.1.1 (Process Systems Enterprise). The chain length of poly(oxymethylene) glycols and of poly(oxymethylene) hemiformals was limited to $n = 10$ and the chain length of OME was limited to $n = 8$. As confirmed by Schmitz et al. [31], there was no significant effect on the results when increasing the maximum chain length. The experiments KIN-S1–KIN-S6 were simulated using the model of the batch reactor as described above. The parameters were adjusted to the experimental concentration profiles by using the maximum likelihood method. The parameters A_j, B_j and a_j, b_j of the temperature-dependent parameters K_{XI}, k_{IX}, and k_{X}, respectively, were fitted to all measured concentrations of all experiments, simultaneously. From KIN-S5 and KIN-S6, only the first five time points were used in the fit. As the absolute mass of the liquid phase decreases during an experiment due to sampling, the relative mass of the catalyst does not have a constant value. To accurately capture the influence of the catalyst-to-mixture ratio, the mass of catalyst was adjusted accordingly in the simulation. During the experiments, the specific catalyst activity decreased, cf. Appendix. To account for the decreased catalyst activity, the mean of the values before and after each experiment was used in the model.

2.5 Results and Discussion

2.5.1 Experimental Profiles and Kinetic Model

The measured neutral overall mass fractions and specific catalyst activities for all experiments (KIN-S1–KIN-S6) are tabulated in Appendix A.4. The concentration profiles of trioxane for all experiments are shown in Figure 5 and Figure 6 along with the calculated results from the model, which are depicted as solid lines. The qualitative concentration profile is similar in all experiments and clearly indicates an equilibrium reaction.

The concentration profiles of methyl formate and formic acid for KIN-S1 and KIN-S2 are illustrated along with the model results in Figure 7. The similarity of the profiles

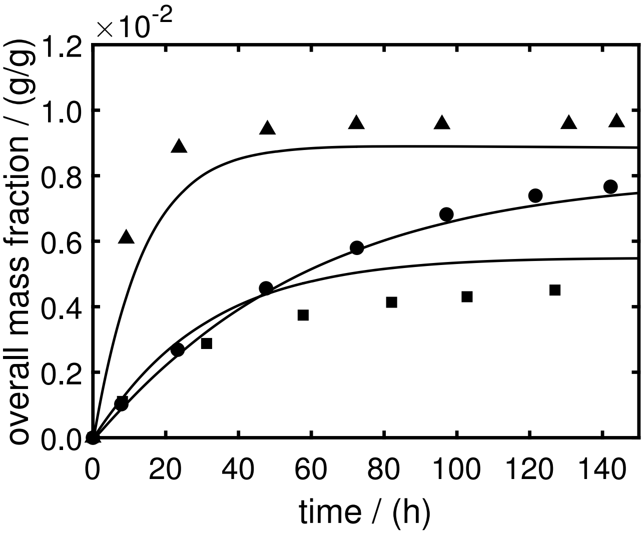

Figure 5: Measured overall concentration profiles of trioxane (symbol, T_{R} / K, $(\hat{m}_{\mathrm{FA}}/\hat{m}_{\mathrm{ME}})$ / (g/g), $\hat{w}_{\mathrm{WA}}$ / (g/g)): KIN-S1(•, 343.15, 0.88, −0.067), KIN-S2(▲, 358.15, 0.92, −0.064) and KIN-S3(■, 358.15, 0.86, 0.041). Kinetic model: solid lines(-).

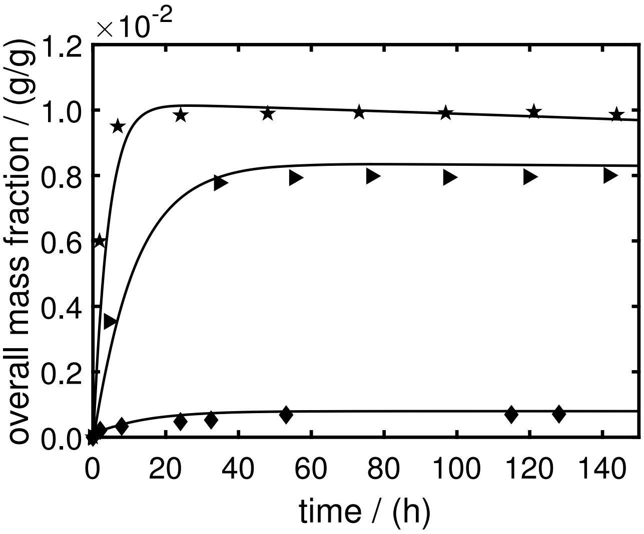

Figure 6: Measured overall concentration profiles of trioxane under varied reaction conditions (symbol, T_{R} / K, $(\hat{m}_{\mathrm{FA}}/\hat{m}_{\mathrm{ME}})$ / (g/g), $\hat{w}_{\mathrm{WA}}$ / (g/g)): KIN-S4(♦, 358.15, 0.58, −0.072), KIN-S5(★, 373.15, 0.94, −0.062), and KIN-S6(▸, 358.15, 0.90, −0.065). Kinetic model: solid lines(-).

of both species is observed in all experiments, cf. Appendix A.5. This corroborates the direct link between methyl formate and formic acid via the esterification reaction (cf. reaction (XI)).

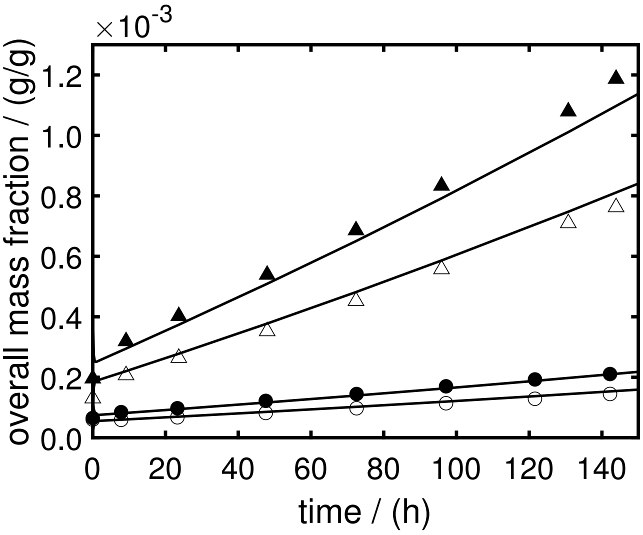

Figure 7: Measured overall concentration profiles of methyl formate (filled symbols) and formic acid (empty symbols) under varied reaction conditions (symbol, T_{R} / K, $(\hat{m}_{\mathrm{FA}}/\hat{m}_{\mathrm{ME}})$ / (g/g), $\hat{w}_{\mathrm{WA}}$ / (g/g)): KIN-S1(•,○, 343.15, 0.88, −0.067), and KIN-S2(▲,△, 358.15, 0.92, −0.064). Kinetic model: solid lines(-).

Not all experimental concentration profiles of methyl formate and formic acid develop linearly till the end. Especially, the concentration profiles from the reaction experiments KIN-S5 and KIN-S6 reveal an increasing slope with the growing concentration of side products (cf. Figure 8). This can be attributed to an autocatalytic effect since increasing amounts of formic acid act as catalyst for its formation reaction [72, 73]. This is in line with studies from the literature, as strong acidic catalysts showed a higher rate of methyl formate formation [16, 48]. However, this effect is limited to only two experiments and, therefore, the amount of experimental data appears to be too small for reliable modeling of autocatalysis. Thus, the model does not account for autocatalytic effects.

The comparison of the model calculations with the experimental results for the formation of trioxane (cf. Figures 5 and 6) and methyl formate and formic acid (cf. Figures 7 and 8) shows a good agreement. Thus, the pseudo-homogeneous kinetic approach is capable of describing the formation of the mentioned side products with good accuracy. The influences of the varied reaction conditions (temperature, educt composition, and mass of catalyst) are represented well by the model. The applied assumption for the average catalyst capacity during the experiments is suitable for describing the experimental profiles but remains uncertain. Especially for the long-term continuous operation, it will be essential to consider catalyst deactivation. Even if the model does not account

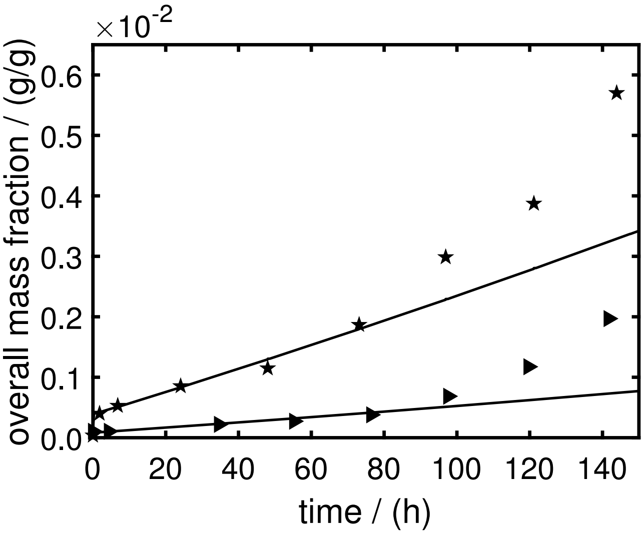

Figure 8: Measured overall concentration profiles of formic acid under varied reaction conditions (symbol, T_R / K, $(\hat{m}_\mathrm{FA}/\hat{m}_\mathrm{ME})$ / (g/g), $\hat{w}_\mathrm{WA}$ / (g/g)): KIN-S5(★, 373.15, 0.94, −0.062), and KIN-S6(▸, 358.15, 0.90, −0.065). Kinetic model: solid lines(-).

for the enhanced autocatalytic formation of side products, the model appears sufficient to enhance process design. The extent of side products should be anyways limited to avoid autocatalysis.

2.5.2 Process Simulation

Side Products and Purge The parameters reactor temperature T_R and side product level $\bar{w}^9_\mathrm{side}$ are varied and the resulting ratio of purge stream to product stream is depicted in Figure 9. As expected, lower side product levels lead to increased purge streams due to the overall material balance of the side products. In addition, an enhanced formation of side products with rising reactor temperature is observed, although the mass of dry catalyst in the reactor was adjusted to meet the same extent of the main reactions. Thus, when the temperature rises, the side reaction resulting in methyl formate is favored compared to the main reactions that form OME.

In order to inhibit autocatalysis, the mass fraction of formic acid should not exceed 0.0005 g/g (cf. Figure 8), which translates to a suggested maximum side product level (sum of MEFO and FOAC) of 0.001 g/g (highlighted in Figure 9). This limitation is recommended as an auto-accelerated formation of side products and, more severe, deleterious effects on the stability of OME in an acidic environment should be avoided. The resulting ratio of purge stream to product stream at a constant side product level

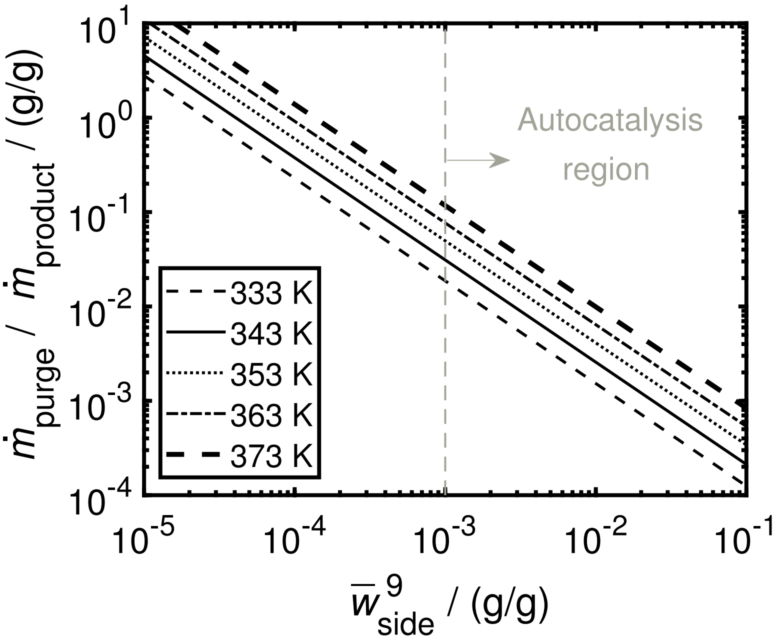

Figure 9: Mass flow ratio of purge/product plotted against the mass fraction of side products in recycle stream 9 $\bar{w}^{9}_{\mathrm{side}}$ at different reactor temperatures T_{R} in a double-logarithmic plot.

($\bar{w}^{9}_{\mathrm{side}}$ = 0.001 g/g) at different reactor temperatures is shown in Figure 10. The necessary mass of catalyst (illustrated as the catalyst-to-product ratio CPR according to eq (29)) is also given.

A trade-off between the purge stream and the mass of catalyst in the reactor is detected. Reducing the purge stream by decreasing the reactor temperature comes with increased demand for catalyst, and vice versa. A reactor temperature of T_{R} = 343.15 K seems to be a good compromise that comes with an acceptable reactor size and a ratio of purge-to-product of 2.7%.

Besides methyl formate and formic acid, trioxane is present in the recycle streams. The trioxane level in recycle stream 9 increases with rising reactor temperature due to faster reaction kinetics of the trioxane formation (see Appendix A.6). As opposed to methyl formate and formic acid, the formation of trioxane is limited to the chemical equilibrium. This is highlighted in Figure 11, where the trioxane level in stream 9 is plotted against the ratio of purge stream to product stream. As a consequence of this limited formation, the implications of trioxane for the process design are bearable, if negative effects on the downstream process units are excluded.

Unlike methyl formate and formic acid, the trioxane level remains roughly constant when the purge-to-product ratio falls below 0.1 g/g due to the said chemical equilibrium. In

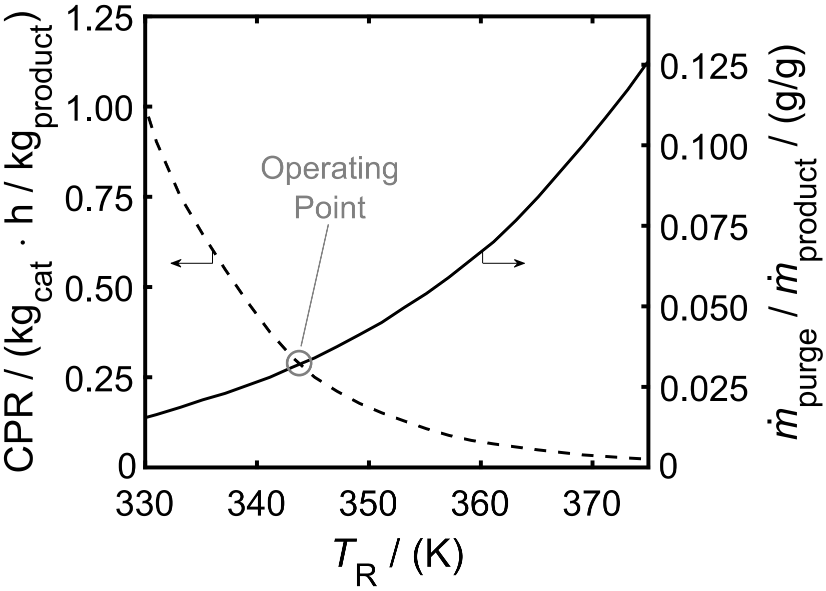

Figure 10: Catalyst-to-product ratio CPR = $m_{cat}/\dot{m}_{product}$ (dashed line, left axis) and mass flow ratio of purge/product (solid line, right axis) plotted against the reactor temperature T_R at a constant mass fraction of side products in recycle stream 9 ($\bar{w}^9_{side}$ = 0.001 g/g).

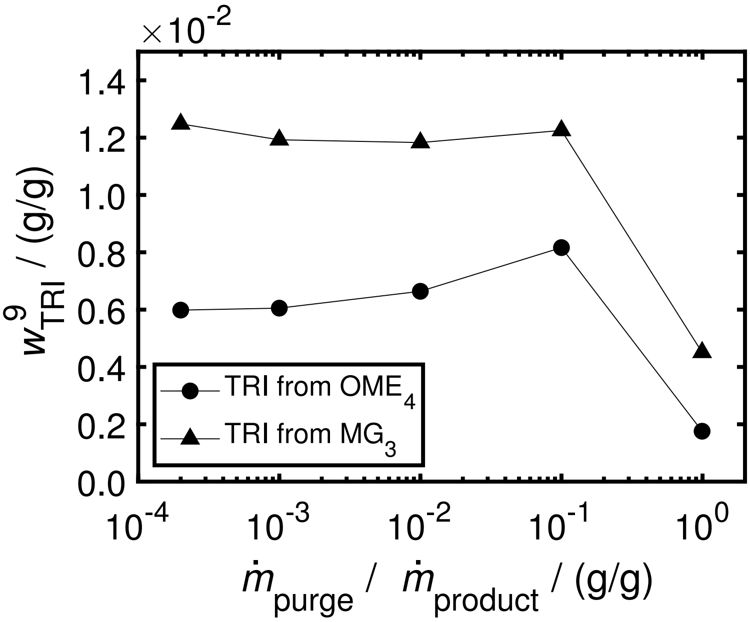

Figure 11: Mass fraction of trioxane in recycle (stream 9) plotted against the mass flow ratio of purge/product at a constant reactor temperature T_R = 343.15 K when two different formation mechanisms are applied: TRI from OME$_4$ (reaction IXa, •), TRI from MG$_3$ (reaction IXb,▲).

addition, Figure 11 reveals the dependence of the resulting trioxane level from the chosen formation mechanism (TRI from OME_4 or MG_3). The reason for this difference is due to the qualitatively different concentration profiles of OME_4 and MG_3 in the PFR, as described previously in the modeling section. A reliable elucidation of the true formation mechanism is not possible from the results in the present work. A combination of both mechanisms is conceivable, as is only one of the mechanisms. For process design and to evaluate the implications on other process units, it is recommended that the higher trioxane level is used as a rather conservative estimate. The choice of trioxane formation mechanism did not affect the results for methyl formate and formic acid.

A stream table, calculated with trioxane formation from MG_3 at the proposed operating conditions from Figure 10 (T_R = 343.15 K, $\bar{w}^9_\mathrm{side}$ = 0.001 g/g), is shown in Table 19 in the Appendix. The stream table reveals that the formation of the side products methyl formate and formic acid inevitably leads to a perceptible purge stream, thus resulting in a loss of product, or in other words, a reduced overall process efficiency. However, the implications of side product formation can be attenuated by applying more focused methods of removal. A partial condensation in the first column (methyl formate is one of the lightest boiling components in the system), a more specific purge within the column (with higher concentrations of side products), or selective adsorption is conceivable. Further, the implications of side product formation can be attenuated by the development of improved catalysts that suppress side product formation.

Product Distribution Adding a purge to the process is not just unfavorable for the process efficiency, but also influences the resulting product composition. Figure 12 shows the distribution of the mass fractions of OME_{3-5} in the product (stream 6) for different purge streams at a constant reactor temperature T_R = 343.15 K. With rising purge mass flow, the mass fraction of OME_3 decreases, and the mass fractions of OME_4 and OME_5 increase. The examination of the overall process mass balance simplified to the acidic overall mass fractions of FA, WA, and ME (cf. Table 19 in the Appendix) reveals that the ratio of formaldehyde to methanol in stream 9, which is partially used as purge, is small compared to the product stream. Removing parts of this stream inevitably results in a larger formaldehyde fraction (or a smaller methanol fraction) in the product, which appears as a shift to long-chain OME. This is also confirmed by the acidic overall FA-to-ME ratio in the product that is shown in Figure 12 and increases with the rising purge-to-product ratio.

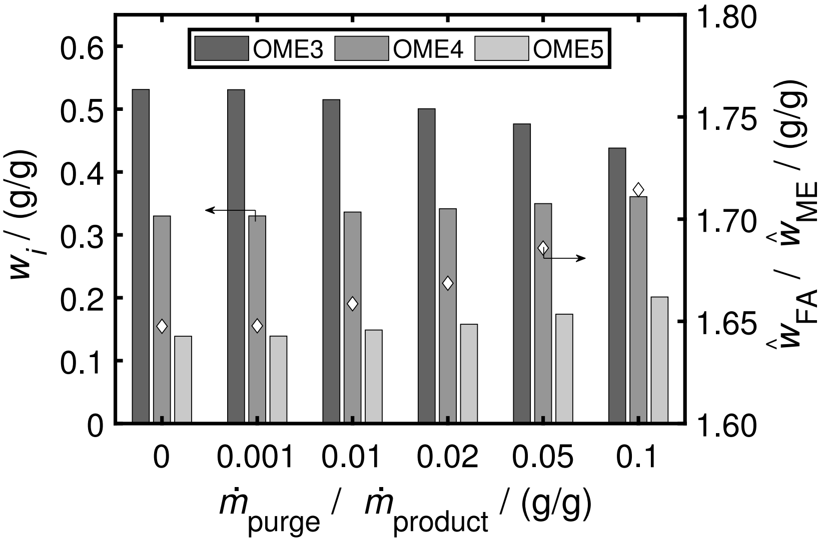

Figure 12: Mass fractions of $OME_{3–5}$ in the product stream (left axis) and the respective ratio of acidic overall mass fractions of formaldehyde to methanol (right axis) plotted against the mass flow ratio of purge/product at a constant reactor temperature T_R = 343.15 K.

3 Scale-up of a Tubular Reactor for the Production of OME

3.1 State of the art

The chemical equilibrium of the reaction of formaldehyde and methanol yielding OME and the associated reaction kinetics are already well-studied in the literature for several catalysts. Oestreich et al. [15] investigated the formation of OME from methanol and formaldehyde in a batch reactor with various types of catalyst. The temperature, and the feed composition were varied and a kinetic model was developed to describe the reaction progress. Drunsel et al. [69] used a tubular reactor filled with the catalyst Amberlyst 15 to examine the formation of methylal from methanol and formaldehyde. The feed composition, the reactor temperature, and the mass flow rate were varied as key parameters influencing the reaction, and samples throughout the reactor were taken to monitor the reaction progress. Zhang et al. [34] performed reaction experiments in a fixed-bed reactor filled with alumina-supported ZrO_2 with methanol and formaldehyde as feed. The applied large temperature range from 333 to 433 K required sufficient pressure up to 2.5 MPa. Peláez et al. [32] investigated the formation of OME from trioxane and methylal catalyzed by Amberlyst 15 in both a batch reactor and a fixed-bed reactor. Again, the feed composition, the reactor temperature, and the mass flow rate were identified as the key parameters influencing the reaction progress.

Ion-exchange resins like the Amberlyst catalysts play an important role in OME synthesis and process design [21, 35]. In general, ion-exchange resins consist of a porous support structure, e.g., a cross-linked divinylbenzene copolymer for Amberlyst resins, and functional groups with anion or cation functionality, leading to either basic or acidic properties. With their mutable properties, ion-exchange resins have a wide range of applications in the chemical industry [68] and are commonly used in the OME synthesis due to their easy handling and excellent catalytic performance [14–16, 69]. Long-term stability, deactivation, and regeneration are additional key factors for the industrial application. Four major deactivation mechanisms are reported in the literature when ion-exchange resins are used as catalyst: fouling, desulfonation, chemical deactivation, and mechanical degradation [77]. Fouling is caused by polymerization or polycondensation products that block pores and therefore the active centers [77]. Desulfonation is mainly related to thermal effects at temperatures above 380 K and denotes a release of the functional sulfonic groups [78]. Chemical deactivation represents the actual ion exchange, meaning, for example, the exchange of the original H^+-ions with cations. Mechanical degradation is caused by improper handling or use [77] and is irreversible. For the other three deactivation mechanisms, regeneration methods like acid-alkali treatment, resulfonation, or oxidizing agent treatment are reported [77, 79, 80]. However, little is known about the (long-term) stability of ion-exchange resins in OME synthesis.

The present chapter describes the scale-up of an OME synthesis reactor to a production capacity of 100 000 tons per year $OME_{3–5}$ (100 kt/a) up to the stage of equipment design. The reactor is assumed to be embedded in a process that consumes only methanol and aqueous formaldehyde solution and yields pure $OME_{3–5}$ and water. The setup of a continuous tubular reactor that is part of an $OME_{3–5}$ demo plant with a capacity of 8 t/a and the reaction and catalyst experiments are described in Section 3.2. The results from the experiments and the model calculations are presented in Section 3.4. The results are further used for the technical design of the large-scale reactor including multiphase flow and heat transfer (Section 3.5).

3.2 Experiments

3.2.1 Chemicals and Catalyst

The experiments of this chapter were performed using paraformaldehyde (>0.895 g/g, rest is mainly water) and methylal (>0.997 g/g) from Prefere. Methanol (>0.998 g/g) was purchased from VWR and 1,3,5-trioxane (>0.99 g/g) was purchased from Sigma-Aldrich. The chemicals were used without further purification. Paraformaldehyde was dissolved in methanol by stirring at 330 K under reflux. As described in Section 2.3.1, the ion-exchange resin Amberlyst 46 was used as catalyst in the tubular reactor and dried overnight in a vacuum oven at 343.15 K and <10 mbar before use.

3.2.2 Analysis

The neutral overall mass fractions of each component and the catalyst activity were determined according to the procedures described in Section 2.3.2.

3.2.3 Reactor Setups

3.2.3.1 Continuous Tubular Reactor

The tubular reactor setup used for the reaction experiments in this chapter is part of a pilot plant for the production of OME from formaldehyde and methanol [40]. The conceptual design of the pilot plant and the reactor is based on the process presented by Schmitz et al. [35]. Details on the process are given in Section 2.2.1. A fixed-bed tubular reactor filled with the heterogeneous catalyst Amberlyst 46 was designed with a production capacity of 1 kg/h $OME_{3–5}$. The reactor specifications are listed in Table 5.

Table 5: Specifications of the reactor setup.

Tubular bed length L_R / m	4.80 (6 x 0.80)
Tube diameter d_R / mm	16.6
Bed volume V_R / L	1.03
Tube material	316L
Catalyst	Amberlyst 46
Mass of dry catalyst m_{cat} / g	309

A piping and instrumentation diagram (P&ID) of the reactor is given in Figure 13. The feed stream is fed to the reactor by the membrane pump P1 with an adjustable stroke length. After passing valve V1, the feed stream is preheated to reach the desired reaction temperature before entering the reactive section. The reactive section consists of six stainless steel tubes in series filled with Amberlyst 46 to allow sampling between each tube. They are placed in an oil bath together with the preheating section to obtain isothermal conditions. The temperature of the oil bath is measured by the Pt 100 thermometer TIC05 and controlled by the thermostat (TH1, Julabo SL-26). After passing the reactive section, the stream is cooled before relaxation to atmospheric pressure to prevent boiling. The pressure inside the reactor is manually controlled by V2 and measured by PIC03 (analog pressure gauge, WIKA).

The reactor setup contains six sample lines (X1–X6), one after each tube containing catalyst. Five Pt 100 resistance thermometers (accuracy ±0.1 K) and two pressure transmitters (WIKA S-20, 0–10 barg, accuracy $\leq \pm 0.1\%$) are installed to obtain an overview of the temperature profile and the pressure drop over the bed. Moreover, a mass flow meter (FI01, Bronkhorst mini CORI-FLOW M14, 0–20 kg/h, accuracy ±0.2%) is used inline. A conductivity sensor (CI01, JUMO Blackline CR-EC) is installed at the end of the reactive section for the residence time distribution experiments. All

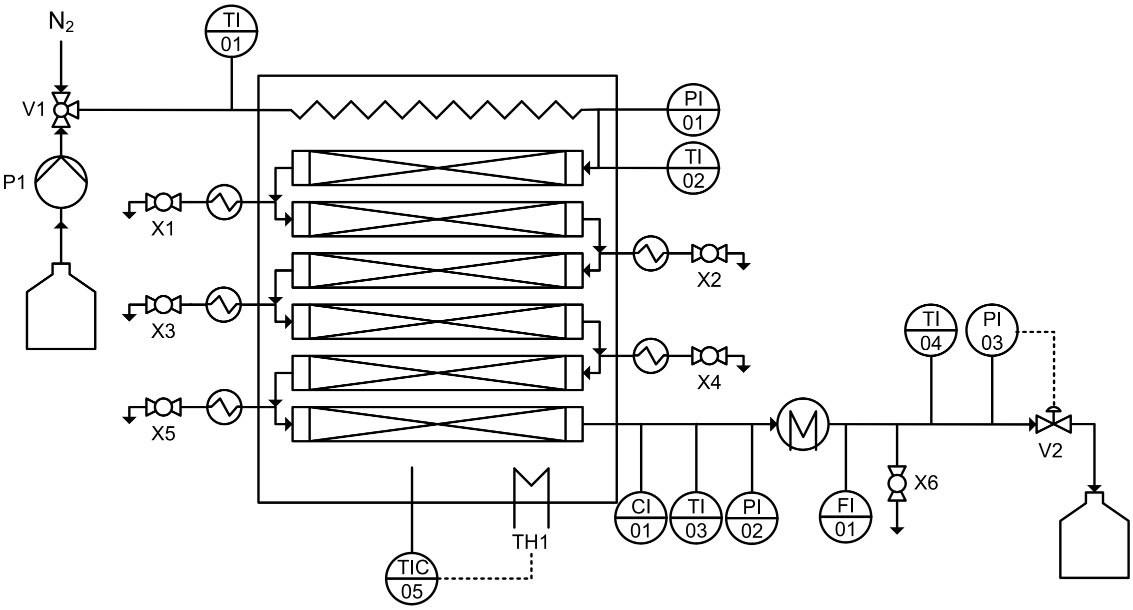

Figure 13: P&ID of the tubular reactor.

signals are processed, visualized, and recorded by hardware from National Instruments in combination with the software LabVIEW (V19.0, National Instruments).

The catalyst Amberlyst 46 swells to different extents depending on the solvent [69] (cf. Appendix B.1). To avoid further swelling after filling, the catalyst was stored in a mixture of formaldehyde, methanol, and mainly OME before filling the reactor tubes. The catalyst showed the largest swelling when stored in this mixture (cf. Appendix B.1). This procedure is crucial as catalyst swelling in a closed reactor can destroy the catalyst and can lead to a decrease of free space in the packed bed, and consequently to a substantial pressure drop. After swelling, the catalyst was carefully filled in each of the six reactor tubes with a special focus on a uniformly distributed packed bed without gaps. After completely filling each of the reactor tubes, the tubes were closed and the catalyst was kept in the reactor tubes by meshes made from stainless steel at the ends of each tube.

3.2.3.2 Batch Stirred-Tank Reactor

In addition to the experiments with the tubular reactor, a 0.5 L batch reactor was used for the reaction experiments. Details on the setup are given in Section 2.3.3.

3.2.4 Procedure

3.2.4.1 Residence Time Distribution

Residence time distribution (RTD) experiments were performed to characterize the continuous tubular reactor. The conductivity of the solution was measured in the reactor directly after the reactive section. Two aqueous feed solutions of different concentrations of hydrochloric acid were used for the experiments. A step function was applied by switching from one to the other feed solution by a valve, and the conductivity was recorded continuously. This procedure was repeated six times per mass flow rate. Three different mass flow rates were evaluated. All RTD experiments were performed at ambient temperature and elevated pressure of 5 bar.

3.2.4.2 Kinetics in the Tubular Reactor

Prior to the reaction experiments, the oil bath was heated overnight to obtain isothermal conditions. The reactor was flushed with nitrogen to avoid contact between the reactive mixture and oxygen, and to eliminate possible side reactions and safety hazards. The reactor was pressurized with nitrogen, and the pressure was set by adjusting V2. The pressure profile inside the reactor was usually kept in a steady-state and was always sufficiently high to keep all components in the liquid phase. The pump was started and the mass flow rate was set by adjusting the stroke length of the pump. Measurement values, i.e., temperatures, pressures, and the mass flow rate, were continuously visualized and recorded during the experiment. Preliminary experiments showed that the steady-state was reached within around 20–30 min depending on the mass flow rate and the reactor temperature. Samples were taken not earlier than 50 min after mass flow rate adjustments. To ensure that the composition at the sampling points did not change any longer and thus steady-state was reached, samples were taken with a 5 min gap at the last sampling point X6. After a further 5 min, the six final samples at all positions X1–X6 were taken starting from the end of the reactor. After the final samples were taken, either the mass flow rate was changed to reach another operating point or the experiment was finished and the reactor was shut down.

The goal of the reaction experiments was to test the performance of the reactor at several operating points. Three parameters were chosen to be varied, particularly the feed composition $\tilde{w}^0$, the reactor temperature T_R, and the mass flow rate through the reactor $\dot{m}$. The feed composition was specified by the initial mass ratio of formaldehyde to methanol $\tilde{w}^0_\mathrm{FA}/\tilde{w}^0_\mathrm{ME}$ and the initial mass fractions of water $\tilde{w}^0_\mathrm{WA}$, OME_1 $\tilde{w}^0_{\mathrm{OME}_1}$, and long-chain OME $\tilde{w}^0_{\text{OME}_{2+}}$. Eight reaction experiments were performed with the tubular reactor. The respective reaction conditions are listed in Table 6.

The feed composition was varied by combining different ratios of methanolic formaldehyde solution ($\tilde{w}_{\text{FA}}/\tilde{w}_{\text{ME}}/\tilde{w}_{\text{WA}} \approx 0.55/0.40/0.05$ g/g) and OME. OME was added because there is a large recycle of OME_1 and OME_2 in the production process [35, 40]. In most experiments, OME_1 was added. In two experiments, KIN-T7 and KIN-T8, also higher OME were added. Details on the feed preparation are given in Appendix B.2. In addition to the variation of the feed composition, the reactor temperature was varied. The mass flow rate was adjusted accordingly to obtain a high conversion with meaningful concentration profiles in the reactor.

Table 6: Overview of Reaction Conditions in Kinetic Experiments KIN-T1–KIN-T8 and KIN-B1

	$\tilde{w}^0_{\text{FA}}/\tilde{w}^0_{\text{ME}}$ g/g	$\tilde{w}^0_{\text{WA}}$ g/g	$\tilde{w}^0_{\text{OME}_1}$ g/g	$\tilde{w}^0_{\text{OME}_{2+}}$ g/g	T_{R} K	$\dot{m}$ kg/h
KIN-T1	1.31	0.02	0.58	-	311	1.6
KIN-T2	1.29	0.02	0.59	-	311	2.1
KIN-T3	1.31	0.02	0.60	-	325	4.2
KIN-T4	1.31	0.02	0.60	-	324	5.0
KIN-T5	1.28	0.02	0.61	-	341	9.3
KIN-T6	1.28	0.02	0.61	-	337	11.5
KIN-T7	1.39	0.02	0.46	0.15*	327	2.6
KIN-T8	1.39	0.02	0.46	0.15*	327	5.2
KIN-B1	1.41	0.02	0.61	-	333	-

* Detailed feed compositions of KIN-T7 and KIN-T8 are given in the Appendix.

3.2.4.3 Kinetics in Batch Reactor

The procedure of the reaction experiments with the batch reactor follows the description in Section 2.3.3.

One reaction experiment (KIN-B1) was performed in the batch reactor. The feed composition and the reaction conditions are listed in Table 6.

3.2.4.4 Catalyst Stability, Deactivation, and Regeneration

The long-term catalyst stability was investigated in the experiment CAT1 as follows. The catalyst was mixed and stirred in methanolic formaldehyde solution ($\tilde{w}_{\text{FA}}/\tilde{w}_{\text{ME}}/\tilde{w}_{\text{WA}}$

≈ 0.55/0.40/0.05 g/g) in a 0.25 L closed vessel for more than 70 days at ambient temperature. Catalyst samples were taken regularly, and the catalyst activity was determined.

Chemical deactivation through feed impurities was evaluated in experiment CAT2 by stirring the catalyst in methanolic formaldehyde solution at ambient temperature with varying solution-to-catalyst mass ratios. This simulates different times on stream during the continuous operation. After stirring for 24 h, the catalyst was separated from the solution, and the catalyst activity was determined.

In addition, experiments were carried out to elucidate the ease of regeneration (CAT3). The catalyst was deactivated completely by stirring in sodium hydroxide solution ($c(\mathrm{NaOH}) = 1$ mol/L) overnight. Residual sodium hydroxide was removed by washing thoroughly with distilled water. The deactivated catalyst was then stirred in various strong acidic solutions: in hydrochloric acid ($c(\mathrm{HCl}) = 1$ and 12 mol/L) and sulfuric acid ($c(\mathrm{H_2SO_4}) = 0.5$ and 7 mol/L) with an acid-to-catalyst mass ratio of roughly 3 to 4. After stirring for 24 h, the catalyst was separated from the solution and washed with distilled water to remove the residual acid. Subsequently, the catalyst activity was determined again.

3.3 Modeling

The model that was used to describe the concentration profiles in the tubular reactor is the same as described in Section 2.4. The parameters for the calculation of k_A and k_G were refitted to the experimental data from the experiments with the tubular reactor that are presented in this chapter. The result of this fit is shown in Table 7.

Table 7: Parameters for the calculation of the reaction rate constants k_j using the correlation $\ln(k_j/(\mathrm{mol}/(\mathrm{s} \cdot \mathrm{mol}^{\mathrm{H}^+}_{\mathrm{cat}}))) = a_j + b_j/(T/\mathrm{K})$.

	a_j	b_j	Reference
k_A	25.82	−8033	This work
k_G	19.13	−4759	

The parameters were adjusted to the experimental concentration profiles of the tubular reactor using the maximum likelihood method. Thereby, the parameters k_A and k_G were fitted individually to the experimental concentration profiles of each experiment KIN-T1–KIN-T6. The profiles of OME_5 and OME_6 were excluded from the fit because their concentrations were small in all experiments with large experimental uncertainty.

The parameters a_j and b_j were then fitted to the resulting values of k_j. Fitting the parameters to all experiments simultaneously did not improve the quality of the model.

To account for the partial deactivation of the catalyst in the first section of the reactor (see Section 3.4), the specific catalyst activity was set to 0.536 mmol(H^+)/g in the first 1/6 of the reactor and set to 0.760 mmol(H^+)/g in the remaining reactor.

3.4 Results and Discussion

3.4.1 Residence Time Distribution

The RTD experiments were carried out with three different mass flow rates. To compare the conductivity profiles, they need to be normalized in amplitude and time. The conductivity values were normalized between 0 (lower concentration of HCl) and 1 (higher concentration of HCl), which converts the experimental conductivity data to the cumulative distribution curve $F(t)$. The time scale was set to 0 at the time the step function was applied at the inlet and set to the average residence time $\bar{\tau}$ when a normalized conductivity of 0.5 was reached. This procedure was chosen as the residence time could not be determined a priori as the porosity of the packed bed was unknown and hard to reliably determine. However, using $\bar{\tau}$ to calculate the porosity ϵ of the packed bed

$$\bar{\tau} = \frac{V}{\dot{V}} = \frac{V_0 + V_\mathrm{R} \cdot \epsilon}{\dot{m}/\rho} \quad \rightarrow \quad \epsilon = \frac{\frac{\bar{\tau} \cdot \dot{m}}{\rho} - V_0}{V_\mathrm{R}} \tag{30}$$

with the constant density $\rho = 1$ kg/L, V_0 as the additional volume of the empty connecting tubes and a known mass flow rate $\dot{m}$, yields a constant value ($\epsilon = 0.44$) for all three mass flow rates. The resulting cumulative distribution curves $F(t/\bar{\tau})$ normalized to $\bar{\tau}$ are shown in Figure 14, whereas only one curve is shown per mass flow rate as deviations between the runs were negligible.

All three curves match, and therefore, the influence of the mass flow rate on the dispersion in the reactor can be disregarded in the studied range. To better assess the resulting curves, the well-known axial dispersion model was chosen for comparison [81, 82]. The dimensionless Bodenstein number Bo represents the ratio of convective to diffusive mass transfer. Thus, large Bodenstein numbers are associated with small axial dispersion. An ideal PFR is represented by $\mathrm{Bo} \rightarrow \infty$. $\mathrm{Bo} = 0$ describes an ideal continuous stirred tank reactor with full backmixing. The cumulative distribution curve depending on Bo is described by [83]

$$F(t/\bar{\tau}) = \frac{1}{2} \cdot \left(1 - \mathrm{erf}\left(\frac{\sqrt{\mathrm{Bo}}}{2} \cdot \frac{1 - t/\bar{\tau}}{\sqrt{t/\bar{\tau}}}\right)\right) \tag{31}$$

Note that, even if eq (31) is based on open–open boundary conditions, which do not always hold in tubular flows, it is still a good approximation when dispersion is small, i.e., when $\mathrm{Bo} > 50$ [83, 84]. Four curves for different Bodenstein numbers are depicted in Figure 14. The experimental curves fit well to $\mathrm{Bo} = 1000$ for $t/\bar{\tau} < 1$ and well to $\mathrm{Bo} = 200$ for $t/\bar{\tau} > 1$. Therefore, the average Bodenstein number is greater than 100, which is considered as the lower limit at which a real reactor can be approximated as an ideal PFR with adequate accuracy [84]. Hence, the assumption of an ideal PFR is justified.

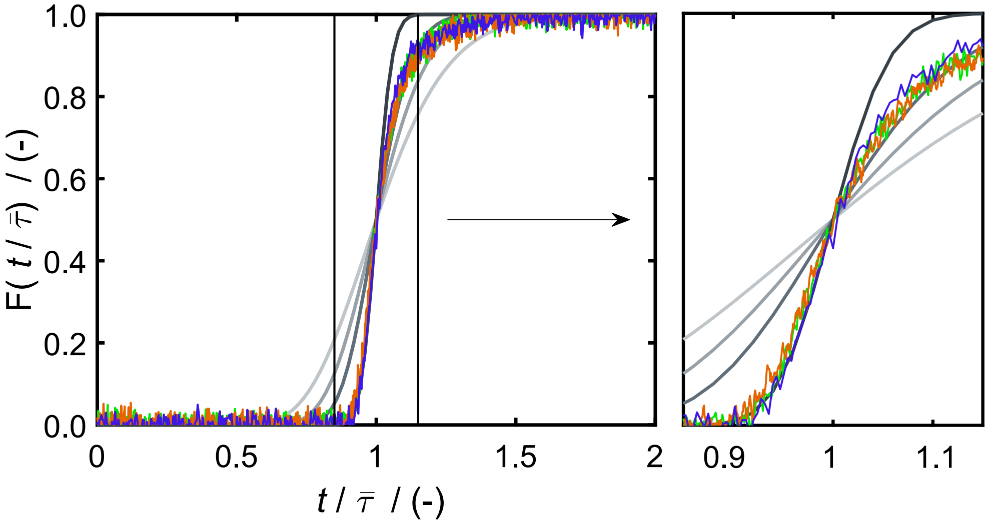

Figure 14: Cumulative distribution curves of the residence time distribution experiments (experimental results: $\dot{m}$ / kg/h = 6.3(–)/10.0(–)/14.2(–), model lines (Bo/– = 50(–)/100(–)/200(–)/1000(–)). The experiments have a strong overlap and are thus hard to discern.

3.4.2 Kinetics in the Tubular Reactor

The results of the reaction experiments KIN-T1–KIN-T8 and KIN-B1 are tabulated in Appendix B.3. The concentration profiles of the various experiments look similar and therefore only representative examples are shown here. All other concentration profiles are depicted in the Appendix.

The concentration profiles over the reactor of the kinetic experiment KIN-T1 are shown in Figure 15. Overall mass fractions are plotted against the pseudo residence time

$$\tau = \frac{m^*_{\mathrm{cat}}}{\dot{m}} \tag{32}$$

for better comparison. As in the kinetic model, the already passed mass of catalyst m^*_{cat} is used to indicate the position in the reactor. The experimental results from the six sample lines and the feed are visualized as symbols. The mass fractions of the educts formaldehyde and methanol decrease within the reactor, and the mass fractions of the products OME and water increase. The profiles fit well to the expected equilibrium reactions as all concentration profiles tend toward an equilibrium concentration with progressive conversion. Even if the chemical equilibrium is not reached in any kinetic experiment, this trend is visible without exception. The concentration profile of OME_1 develops noticeably different compared to the other components, c.f. Figure 15. The mass fraction increases slightly until the first sample line. This development occurs in almost all kinetic experiments. It can be attributed to the enhanced OME_1 formation from acetalization (see reactions (V) and (VI)) as formaldehyde and methanol are, besides OME_1, primarily present in the feed and therefore in the first reactive section. With decreasing concentration of formaldehyde and methanol, the mass fraction of OME_1 decreases because the chain elongation to OME_{2+} dominates. Long-chain OME are formed simultaneously, which is consistent to literature [15, 31]. This indicates that OME are formed individually from the reactive solution by the acetalization reactions (V) and (VI). However, as described by Schmitz et al. [31], with large amounts of OME present in the solution, the chain growth reactions also need to be considered to reliably describe the reaction kinetics.

The feed compositions of the reaction experiments KIN-T7 and KIN-T8 are very close to the expected process conditions from the conceptual process design [35]. In addition, the experimental conditions of KIN-T7 and KIN-T8 were chosen to evaluate the influence of the flow velocity and the potential mass transfer limitation. The feed composition and the reactor temperature were kept constant, and the mass flow rate was increased by a factor of 2 between KIN-T7 and KIN-T8. These mass flow rates correspond to empty tube velocities of 0.33 and 0.67 cm/s, respectively. The experimental results from KIN-T7 and KIN-T8 are plotted in Figure 16. When one assumes an ideal PFR without mass transfer limitations, the concentration profiles of KIN-T7 and KIN-T8 should be identical. Consequently, there is only one common simulation result for both KIN-T7 and KIN-T8. The experimental concentration profiles fit well together. Thus, mass transfer limitations can be disregarded within the applied operating conditions.

Besides the experimental values, Figures 15 and 16 contain results from model calcu-

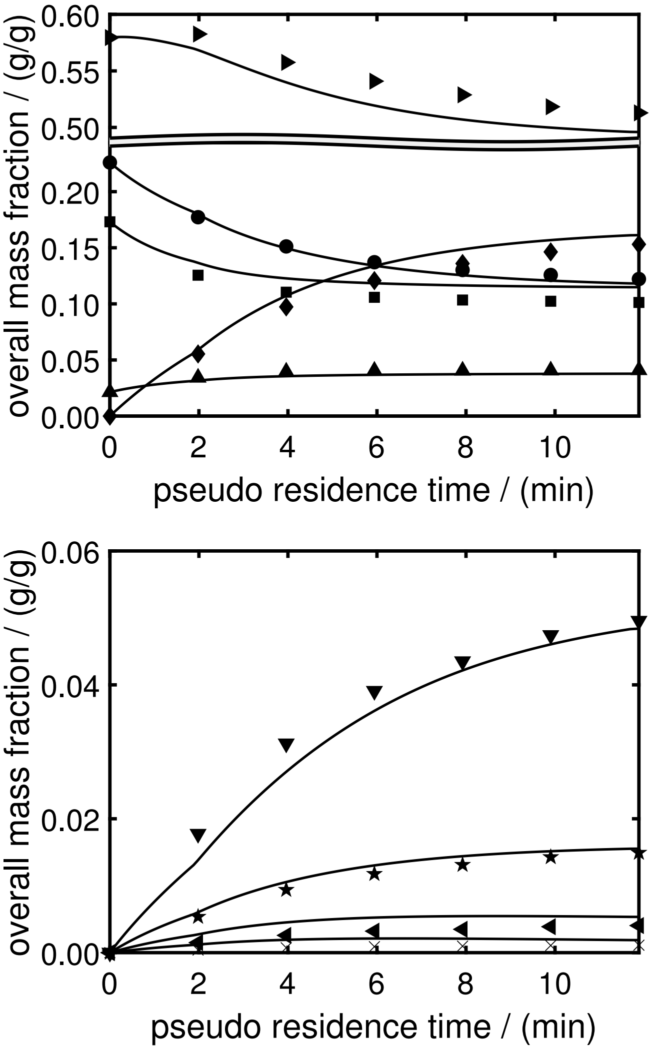

Figure 15: Measured overall concentration profiles of reaction experiment KIN-T1 (formaldehyde (•), methanol (■), water (▲), OME$_1$ (▸), OME$_2$ (◆), OME$_3$ (▾), OME$_4$ (★), OME$_5$ (◂), OME$_6$ (×), Kinetic model (–)).

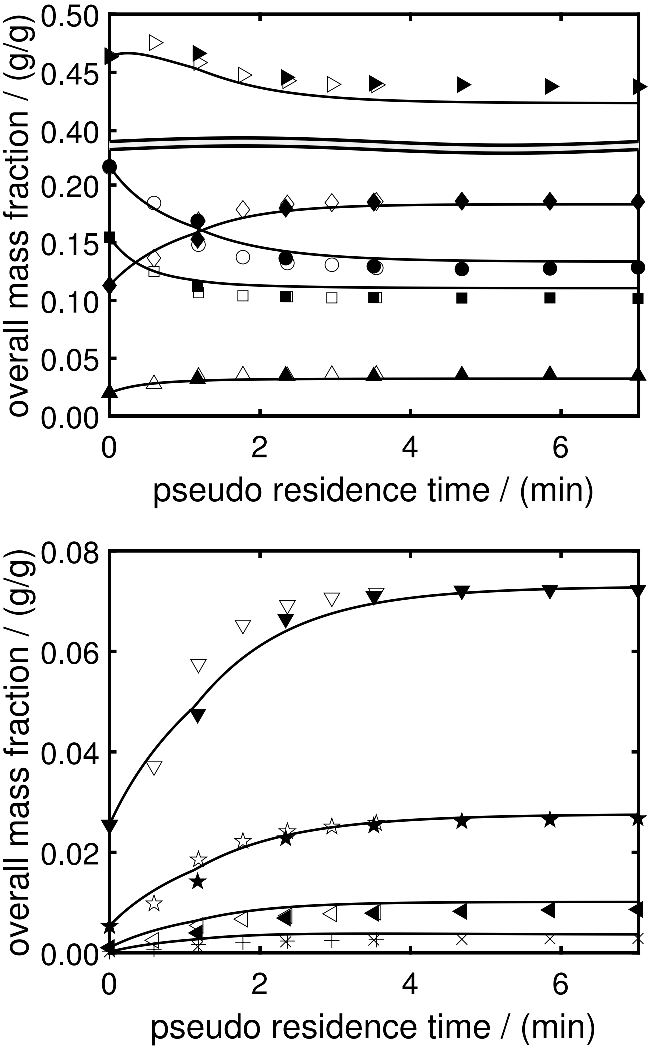

Figure 16: Measured overall concentration profiles of reaction experiment KIN-T7 (filled symbols) and KIN-T8 (empty symbols) normalized to pseudo residence time τ (formaldehyde (•,○), methanol (■,□), water (▲,△), OME$_1$ (▶,▷), OME$_2$ (◆,◊), OME$_3$ (▼,▽), OME$_4$ (★,☆), OME$_5$ (◀,◁), OME$_6$ (×,+), Kinetic model (–)).

lations. The solid lines represent the calculated concentration profiles. The suddenly changing slope of the model lines at the normalized reactor length 1/6 originates from a different catalyst activity in the first section of the reactor. The model is capable of reliably describing the concentration profiles of all components. The kinetic experiments KIN-T7 and KIN-T8 were not involved in the fitting procedure; the model results are therefore predictive. The comparison between the experiment and model in Figure 16 shows that even when OME_{2+} are present in the feed stream the model is also able to predict the concentration profiles.

3.4.3 Kinetics in Batch Reactor

The model was adopted from Schmitz et al. [31], who have reported the parameters k_A and k_G with smaller values, i.e., slower (cf. Tables 4 and 7). In contrast to this chapter, Schmitz et al. [31] used a batch reactor to study the kinetics of the OME formation. So, one possible explanation for the discrepancy between the parameter values could be the different reactor type along with changing mass transfer conditions. To test this hypothesis, the batch reactor experiment KIN-B1 was performed. The time profile of the experimental samples is shown in Figure 17.

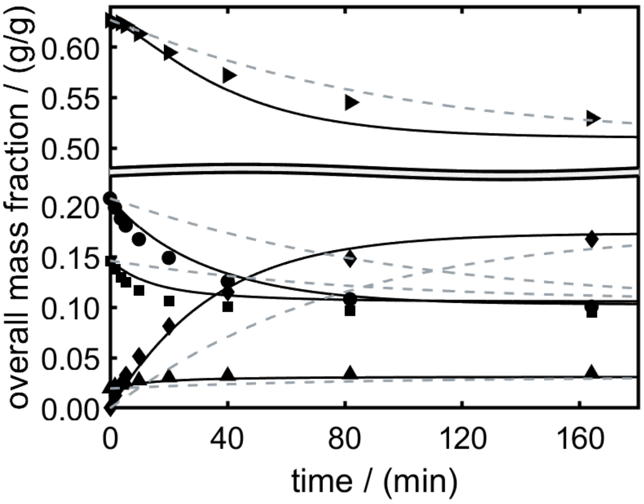

Figure 17: Measured overall concentration profiles of reaction experiment KIN-B1 (formaldehyde (•), methanol (■), water (▲), OME_1 (▶), OME_2 (◆). Kinetic model (–), Original kinetic model [31] (– –)).

Additionally, the figure depicts model calculations from both model parametrizations, the present work (solid line) and the parametrization from Schmitz et al. [31] (dashed line). It is clearly visible that the parametrization from Schmitz et al. [31] underestimates the reaction progress and that the present work's parametrization fits well to the reaction profiles, even if KIN-B1 was not involved in the fitting procedure. This indicates that the different reactor type is not responsible for the discrepancy between the two parametrizations. It is likely that Schmitz et al. [31] used an Amberlyst 46 that was less active or partly deactivated compared to the one used in the present work.

To sum up, the adjusted model is capable of reliably describing the experimental results of the present work that represent the conditions that are expected in the OME production process. Nevertheless, the discrepancy between the experimental results of the present work and Schmitz et al. [31] reveals that even when using the very same catalyst, reaction kinetics can be slightly different.

3.4.4 Catalyst Stability, Deactivation, and Regeneration

A crucial aspect of the operation of a continuous industrial process is the long-term stability of the catalyst. In experiments that are not shown in the present work, it was observed that the catalyst was partly contaminated by sodium ions (replacing hydrogen ions and decreasing the activity) if they are present in the feed (see Appendix B.5 for further details). Sodium ions are for example brought into the process by preparing feedstock solutions with NaOH. For the preparation of the experiments that are shown in this chapter, all solutions were prepared without NaOH, and consequently, no such contamination was observed. This is supported by the good fit of the reaction model to the experiments KIN-T7 and KIN-T8 (see Figure 16) that were performed at the very end of the campaign and were not included in the model fit. In addition, no trend is observed when the values of k_A and k_G obtained from single successively performed experiments are compared to the model fit (see Appendix B.6). Significant catalyst deactivation would have slowed the reaction and, thus, would have emerged from the parameter fit.

As the significance of this observation is restricted due to the limited total operating time of 25 h of all reaction experiments, additional experimental studies to further examine the catalyst deactivation were performed. In stability experiment CAT1, neither a significant reduction of activity nor any visual degradation of the catalyst was observed (see Appendix B.7 for details). The results from the CAT2 experiments are shown in Figure 18 along with the catalyst activity of a fresh catalyst as reference. With rising solution-to-catalyst ratio, the catalyst activity decreases. This is attributed to the increasing total amount of cations that are in contact with the catalyst. These cations exchange the active H^+-ions of the catalyst and therefore reduce the catalyst activity. The cations were not specifically added but were present in the raw materials methanol and paraformaldehyde. The significance of Figure 18 regarding the long-term continuous operation is hard to evaluate. When one considers the fresh feed stream (1.243 kg/h methanolic formaldehyde solution to produce 1 kg/h $OME_{3\text{–}5}$) as the only source for ions and therefore solely responsible for the catalyst deactivation and infinitely fast and complete ion exchange, a solution-to-catalyst ratio of 1000 is reached after around 250 h of operation of the pilot plant reactor. This estimate represents a minimum value and is therefore not necessarily applicable to the real conditions. Based on the experimental results with the pilot plant reactor, it is expected that the reactor can be operated for more than 250 h before substantial catalyst deactivation occurs. Although this rough estimation is subject to uncertainties, it illustrates the need for further studies regarding the catalyst deactivation, especially during continuous operation. If the catalyst deactivation turns out to be a problem, potential solutions could be a feed pretreatment or an additional catalyst section prior to the reactor as a guard bed. This section could be realized redundantly in combination with regeneration cycles to obtain permanent functionality.

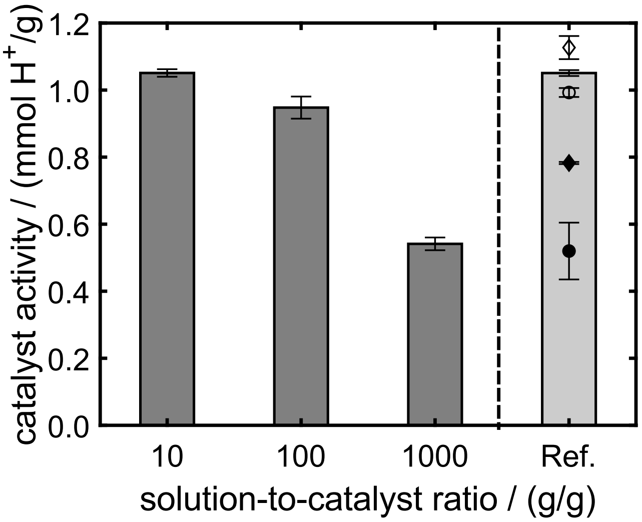

Figure 18: Measured catalyst activity after storing the catalyst for 24 h in methanolic formaldehyde solutions (CAT2, dark grey bars) and after regeneration with hydrochloric acid (CAT3, ⧫ 1 mol/L, ◊ 12 mol/L) and sulfuric acid (CAT3, • 0.5 mol/L, ∘ 7 mol/L) (Ref. indicates the reference catalyst activity of a fresh catalyst, errorbars indicate the standard deviation of the measured values. The standard deviation for 1 mol/L HCl is barely discernible due to its small value.).

The results from the catalyst regeneration experiments CAT3 are also depicted in Figure 18 as symbols. All acids were able to recover at least parts of the original catalyst activity. Unsurprisingly, the concentrated acids (empty symbols) performed better than the diluted acids (filled symbols). The resulting catalyst activity from the treatment with concentrated hydrochloric acid slightly exceeded the original benchmark. The regeneration ability of Amberlyst catalysts has also been reported in the literature [85, 86]. Acid treatment successfully restores the acid sites and thus catalytic performance. However, to ensure proper catalyst handling, the recovery method should be further examined in extended experiments, especially regarding the stability in repeated deactivation regeneration cycles.

3.5 Scale-up for OME Production including Downstreaming

The tubular reactor model was used in a process simulation to design an industrial-size process following the conceptual design from Schmitz et al. [35] with a production capacity of 100 kt/a $\mathrm{OME}_{3\text{–}5}$. The process simulation was performed according to the description in Section 2.4.3. The conversion in the reactor is characterized by the reactor temperature T_R and the catalyst-to-product ratio $\mathrm{CPR} = m_\mathrm{cat}/\dot{m}_\mathrm{product}$ (the inverse of the space–time yield, STY) as described in eq (29). Keeping the temperature constant at $T_\mathrm{R} = 343$ K, which was suggested in Chapter 2 and by Schmitz et al. [35], leaves the CPR as the remaining parameter influencing the conversion and, thus, downstreaming. With the given feed and product streams, the recycle streams in the process are crucial for the size of all equipment in the process. The recycle mass ratio $\dot{m}_\mathrm{recycle}/\dot{m}_\mathrm{product}$ is plotted against CPR in Figure 19.

Figure 19 shows that using small amounts of catalyst leads to unreasonably large recycle streams of unreacted educts. An increase in the mass of the catalyst decreases the recycle ratio but only until a lower limit is reached. This limit results from the chemical equilibrium. The depicted design point in Figure 19 was chosen for further calculations due to its small recycle ratio and its reasonable reactor size ($\mathrm{STY}=10\ \mathrm{kg}_\mathrm{prod}/(\mathrm{kg}_\mathrm{cat}\cdot \mathrm{h})$). The resulting input parameters for the design of the tubular reactor of the industrial size process are listed in Table 8.

Heat transfer often plays a major role when designing large reactors. The OME reactions however show a small reaction enthalpy [14–16]. A mixture of formaldehyde and methanol (0.6 g/g FA, 0.4 g/g ME) that reacts at 298 K to OME until the chemical equilibrium is reached has an adiabatic temperature rise of roughly 12 K (details of the calculation are given in the Appendix B.9). Since the process has large recycle

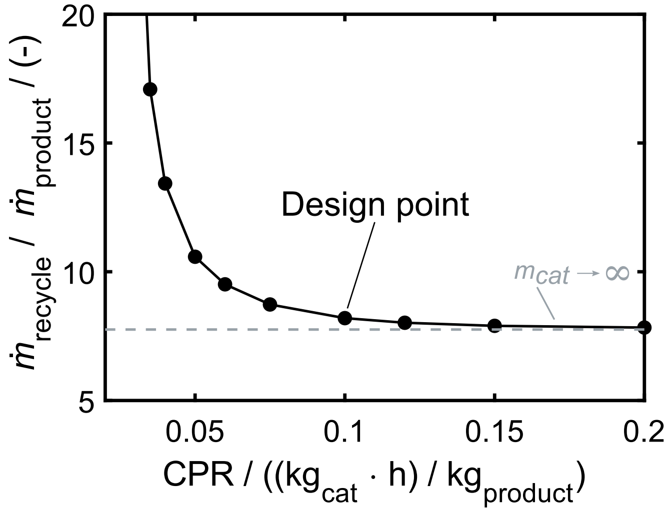

Figure 19: Recycle ratio $\dot{m}_{\text{recycle}}/\dot{m}_{\text{product}}$ plotted against the catalyst-to-product ratio CPR. The lower limit of the recycle ratio (dashed line) originates from the limiting chemical equilibrium.

Table 8: Input parameters for the design of the reactor for a product capacity of 100 kt/a $\text{OME}_{3\text{–}5}$.

$\dot{m}_{\text{product}}$ / t/h	12.5^{a}
ρ / kg/m^3	1000^{b}
η / mPa · s	0.40^{b}
catalyst	Amberlyst 46
$c_{\text{cat}}^{\text{H}^+}$ / mmol(H$^+$)/g	1.0
d_{cat} / mm	0.6
ϵ / -	0.44
STY / kg$_{\text{prod}}$/(kg$_{\text{cat}}$ · h)	10
m_{cat} / kg	1250
V_{R} / m^3	3.87^{c}

[a] Calculated with a plant availability of 8000 h/a .

[b] Estimated from available pure component data (details in Appendix) .

[c] Calculated with the catalyst density ρ_{cat} =323 kg/m^3 .

streams, that bring in significant heat capacity, the adiabatic temperature rise including the recycle is even smaller. This means that the heat transfer in the reactor poses no technological challenge and does not restrict the reactor design.

Another challenge during scale-up, especially for packed-bed reactors, is to keep the pressure drop over the reactor at an acceptable level. The pressure drop is influenced by the flow characteristics and thus by the geometry of the reactor. In the present work, a reactor that consists of one or more tubes filled with catalyst is considered. Given the total volume V_{R} of these tubes, cf. Table 8, there is a multitude of combinations of the design parameters pressure drop Δp, the empty tube velocity u_0, the number of parallel tubes n_{R}, the diameter d_{R}, and the length L_{R} of the tubes. These parameters are related via geometric relations

$$V_{\mathrm{R}} = n_{\mathrm{R}} \cdot L_{\mathrm{R}} \cdot \frac{\pi}{4} \cdot d_{\mathrm{R}}^2 \tag{33}$$

and correlations for the pressure drop of parallel tubes. Here, the Ergun equation [87]

$$\Delta p = \frac{\rho \cdot u_0^2 \cdot L_{\mathrm{R}}}{2 \cdot d_{\mathrm{cat}}} \cdot \frac{1-\epsilon}{\epsilon^3} \left[3.5 + \frac{300 \cdot (1-\epsilon)}{\mathrm{Re}}\right] \tag{34}$$

with ρ as the liquid density, d_{cat} as the diameter of a single catalyst particle, ϵ as the porosity of the packed bed, and Re as the Reynolds number is used. The Reynolds number for packed beds is defined as

$$\mathrm{Re} = \frac{\rho \cdot d_{\mathrm{cat}} \cdot u_0}{\eta} \tag{35}$$

with η as the liquid dynamic viscosity. The values of the parameters of eqs (34) and (35) are listed in Table 8. Given V_{R} and the above equations, the design of the reactor has two degrees of freedom and thus can be conveniently visualized in the 2D plot shown in Figure 20.

The axes show the pressure drop Δp over the reactor and the length-to-diameter ratio of the tubes $L_{\mathrm{R}}/d_{\mathrm{R}}$, both having a logarithmic scale illustrating the immense impact of the parameters. Typically, the ideal plug flow model can be used for packed beds with length-to-diameter ratios $L_{\mathrm{R}}/d_{\mathrm{R}} > 50$ for a wide range of flow velocities [84, 88, 89]. Using this value as the lower limit reveals that a single tube reactor ($n_{\mathrm{R}} = 1$) has a $\Delta p > 100$ bar. Thus is hardly feasible. An increase in the number of tubes substantially decreases the pressure drop and offers reasonable geometries. For example, one could use $n_{\mathrm{R}} = 30$ tubes of diameter $d_{\mathrm{R}} = 0.15$ m with $L_{\mathrm{R}} = 7.4$ m, $u_0 = 0.06$ m/s, and $\Delta p = 8.5$ bar (example illustrated as • in Figure 20).

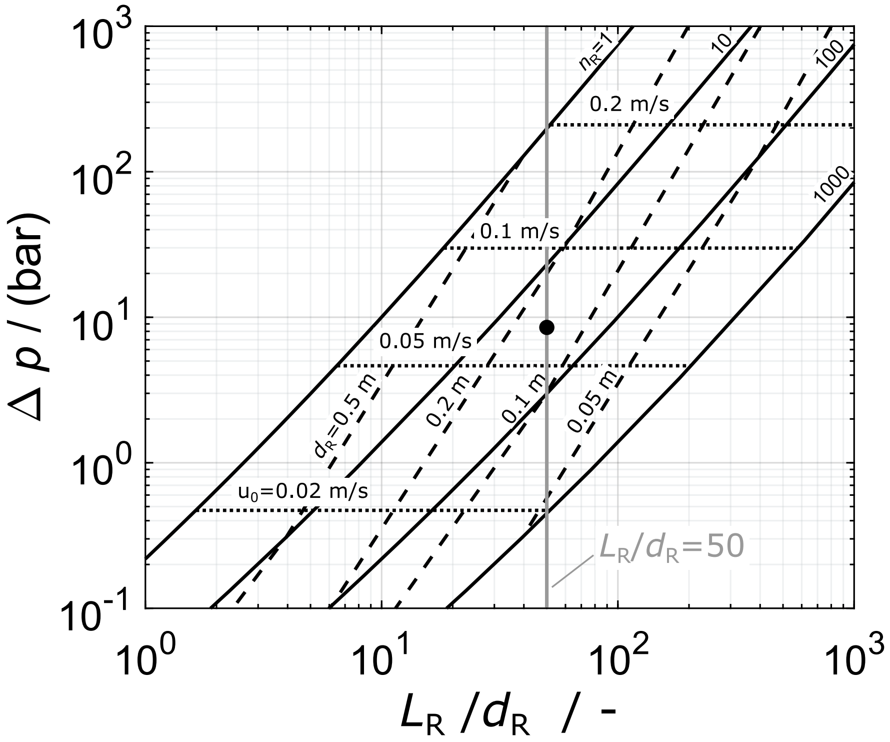

Figure 20: Pressure drop Δp over the reactor of the large-scale process plotted against the length to diameter ratio $L_\mathrm{R}/d_\mathrm{R}$. Three different sets of lines are plotted. Each set shows curves when a single parameter is kept constant at the given value (n_R (solid line), d_R (dashed line), and u_0 (dotted line)).

The last aspect of the scale-up discussed in the present work is the mass transfer from and to the heterogeneous catalyst. During the reactor experiments, no mass transfer limitation was observed that had not yet been included in the model. The reaction experiment with conditions closest to the large-scale process is KIN-T5 with T_R =341 K. When the flow velocity is assumed to be the main impact factor for the mass transfer, the empty tube flow velocity u_0 = 0.012 m/s from KIN-T5 can be taken as the lower limit. The above example and most of the data in Figure 20 exceed this lower limit. Hence, mass transfer is not expected to cause problems during scale-up.

To summarize, a reactor with a space–time yield of 10 $\mathrm{kg_{prod}/(kg_{cat} \cdot h)}$ is a good compromise between the mass of catalyst and the recycle-to-product ratio. Heat and mass transfer do not restrict the reactor design. A feasible pressure drop over the fixed-bed reactor can be obtained when multitube reactors are considered.

4 Chemical Equilibrium of Transacetalization and Oligomerization Reactions

4.1 Introduction and State of the art

In this chapter, the chemical equilibrium of the transacetalization and oligomerization reactions of poly(oxymethylene) dialkyl ethers (OAE) is systematically examined. Adjusting the chain length and the terminating end group by these reactions offers the potential of tuning physical and fuel properties [41, 42]. Most of the studies in literature have focused on the determination of these properties to identify promising fuel candidates [43–46]. In addition, Haltenort et al. [90] investigated the oligomerization and transacetalization reaction of methyl and ethyl-terminated OAE at mild conditions (T = 25 °C, p = 1.013 bar) using the zeolite BEA25 as acidic catalyst. The chain lengths in chemical equilibrium followed a Schulz-Flory distribution for both investigated ethers. In addition, the exchange of end groups was observed when OAE with different end groups were mixed with a catalyst. The same group [91] enlarged the variety of studied alkyl groups and produced asymmetric OAE with the chain length n = 1 and with terminating ethyl, propyl, butyl, and 2-ethylhexyl-groups via transacetalization. The products were extensively analyzed regarding physico-chemical, thermodynamic, and fuel properties.

This chapter presents a quantitative model of oligomerization and transacetalization reactions in OAE systems. The model is entirely predictive and describes the equilibrium composition in water-free mixtures of any OAE and mixtures thereof. The model is based on simple statistical considerations and a generalized chemical equilibrium constant for oligomerization reactions with formaldehyde that was uncovered by Kircher et al. [92]. This generalized constant is in line with experimental results on the oligomerization reaction of formaldehyde in systems containing various alcohols and water that have been collected starting in 1994 [53] and continuing today [93].

This chapter is structured as follows. First, the chemical system, its nomenclature, and the model are described (Section 4.2). In Section 4.3, the experiments and their analysis are presented. Finally, the chemical equilibrium constants for the oligomerization and transacetalization reactions are determined and the model is compared to the experimental results (Section 4.4).

4.2 Modeling

4.2.1 Nomenclature of Ethers

The general structure of poly(oxymethylene) dialkyl ethers (OAE) represents a variety of different compounds and is shown in Figure 21. All OAE are characterized by their alkyl groups R, R' and their chain length n, i.e., the number of repeating oxymethylene units. OAE are either symmetric ($\mathrm{R} = \mathrm{R}'$) or asymmetric ($\mathrm{R} \neq \mathrm{R}'$). The short notation R, R'-OAE_n for the OAE in Figure 21 is used. For instance, Et,Bu-OAE_3 denotes the OAE with an ethyl and a butyl group and three oxymethylene units of the chemical structure $C_2H_5{-}O{-}(CH_2O)_3{-}C_4H_9$. Thereby and in the following, linear alkyl groups (e.g., n-butyl) are meant when not further specified.

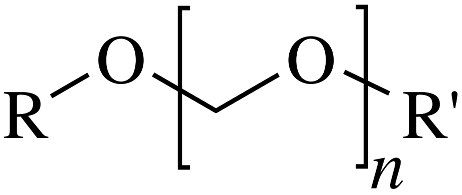

Figure 21: General chemical structure of poly(oxymethylene) dialkyl ethers R, R'-OAE_n.

4.2.2 Model Reactions

Although some of the following reactions are mentioned in previous chapters, they are renumbered in this chapter to avoid confusion and facilitate understanding.

The chemical system consisting of all OAE with $\mathrm{R} = \mathrm{R}'$ being members of a given set of alkyl groups $G = \{R_\alpha, R_\beta, R_\gamma, ...\}$ is considered. Further, formaldehyde (FA) and trioxane (TRI) are part of the chemical system. While these compounds are stable at neutral conditions, they form a reactive system in an acidic environment. A large number of reversible reactions are conceivable. Trioxane decomposes into formaldehyde [56, 59]:

$$\mathrm{TRI} \xrightleftharpoons{\mathrm{H}^+} 3\,\mathrm{FA} \tag{XIII}$$

The R,R'-OAE_n undergo oligomerization reactions [14, 16, 17], either with formaldehyde

$$\mathrm{R},\mathrm{R}'{-}\mathrm{OAE}_{n-1} + \mathrm{FA} \xrightleftharpoons{\mathrm{H}^+} \mathrm{R},\mathrm{R}'{-}\mathrm{OAE}_n \qquad \forall\, \mathrm{R},\mathrm{R}' \in G,\ \ n > 1 \tag{XIV}$$

with trioxane

$$\mathrm{R},\mathrm{R}'{-}\mathrm{OAE}_{n-3} + \mathrm{TRI} \xrightleftharpoons{\mathrm{H}^+} \mathrm{R},\mathrm{R}'{-}\mathrm{OAE}_n \qquad \forall\, \mathrm{R},\mathrm{R}' \in G,\ \ n > 3 \tag{XV}$$

or with themselves

$$\mathrm{R},\mathrm{R}'{-}\mathrm{OAE}_k + \mathrm{R},\mathrm{R}'{-}\mathrm{OAE}_l \xrightleftharpoons{\mathrm{H}^+} \mathrm{R},\mathrm{R}'{-}\mathrm{OAE}_{k-1} + \mathrm{R},\mathrm{R}'{-}\mathrm{OAE}_{l+1} \qquad \forall\, \mathrm{R},\mathrm{R}' \in G,\ \ k > 1, l > 0 \tag{XVI}$$

If more than one different alkyl group is present, transacetalization reactions are observed [90], for example

$$\mathrm{R{,}R}{-}\mathrm{OAE}_n + \mathrm{R}',\mathrm{R}'{-}\mathrm{OAE}_n \xrightleftharpoons{\mathrm{H}^+} 2\,\mathrm{R},\mathrm{R}'{-}\mathrm{OAE}_n \qquad \forall\, \mathrm{R},\mathrm{R}' \in G,\ \mathrm{R} \neq \mathrm{R}',\ \ n > 0 \tag{XVII}$$

Many further reactions are conceivable, e.g., transacetalization reactions between OAE with different chain lengths n and n'. Furthermore, the reaction system gets significantly more complex in presence of water or alcohols (see Section 2.2.1). Water and alcohols would also react with formaldehyde. The OAE would be hydrolyzed to hemiformals. These reactions would lead to further types of oligomers. In the present work, we consider however only systems free of water and alcohols.

4.2.3 Equilibrium Model

In this work, a model for the chemical equilibrium in the liquid phase is presented. The law of mass action as definition of the equilibrium constant K_j of reaction j is formulated using mole fractions

$$K_j(T) = \prod_{i=1}^{N_\mathrm{C}} x_i^{\nu_{ij}} \tag{36}$$

with N_C as the number of components, x_i as the mole fraction of component i and ν_{ij} as the stoichiometric coefficient of component i in reaction j. The stoichiometric coefficients have negative values for educts and positive values for products. By using the chemical equilibrium constants based on mole fractions, ideal mixtures according to Raoult are assumed. Given the chemical similarity of the components, this seemed reasonable, especially as this approach has already shown good results when working with oligomerization reactions of OME [14–16].

Independent of the actual reaction mechanism, it is sufficient to describe the chemical equilibrium with a minimum set of linear independent reaction equations. In the present work, the decomposition of trioxane (reaction (XIII)), the oligomerization reactions (XIV) for all R, R' in G, including symmetric and asymmetric OAE of all $n > 1$, and the transacetalization reactions (XVII) of the shortest ethers ($n = 1$) for all R, R' in G with $\mathrm{R} \neq \mathrm{R}'$ were chosen. All other reactions mentioned in the previous section result from linear combinations of this minimum set of reactions.

For the three types of reactions in the minimum set, the three respective equilibrium constants are

$$K_\mathrm{XIII}(T) = \frac{x_\mathrm{FA}^3}{x_\mathrm{TRI}} \tag{37}$$

$$K_\mathrm{XIV}^{\mathrm{R},\mathrm{R}',n}(T) = \frac{x_{\mathrm{R},\mathrm{R}'\text{-}\mathrm{OAE}_n}}{x_{\mathrm{R},\mathrm{R}'\text{-}\mathrm{OAE}_{n-1}} \cdot x_\mathrm{FA}} \qquad \forall\, \mathrm{R}, \mathrm{R}' \in G,\ \ n > 1 \tag{38}$$

$$K_\mathrm{XVII}^{\mathrm{R},\mathrm{R}'}(T) = \frac{x_{\mathrm{R},\mathrm{R}'\text{-}\mathrm{OAE}_1}^2}{x_{\mathrm{R},\mathrm{R}\text{-}\mathrm{OAE}_1} \cdot x_{\mathrm{R}',\mathrm{R}'\text{-}\mathrm{OAE}_1}} \qquad \forall\, \mathrm{R}, \mathrm{R}' \in G,\ \mathrm{R} \neq \mathrm{R}' \tag{39}$$

Table 9 gives an overview of the total number of components and independent equilibrium constants/reactions in the system, depending on the number of different alkyl groups N_G and the maximum chain length n_max.

The large number of independent K's is drastically reduced using the following two assumptions:

a) According to Kircher et al. [92], the oligomerization by the addition of formaldehyde is described using the generalized constant independent of the terminating alkyl group and the chain length. Thus, all K_XIV are assumed identical independent of R and R' and the chain length, and identical to the generalized constant reported by Kircher et al. [92], cf. Table 10.

b) The equilibrium of the transacetalization reaction (XVII) is assumed to be solely determined by statistical distribution of the alkyl groups leading to the constant value $K_{\mathrm{XVII}} = 4$. A purely statistical distribution is in line with experimental results in the literature [90, 91] and the experimental results of the present work, cf. below.

Table 9: Number of components and independent equilibrium constants/reactions in a system with N_G different alkyl groups and the maximum chain length $n_{\max}$.

# of different alkyl group combinations (types of OAE)	$N_G \cdot (N_G + 1)/2$
# of OAE species	$N_G \cdot (N_G + 1) \cdot n_{\max}/2$
# of components	$N_G \cdot (N_G + 1) \cdot n_{\max}/2 + 2$
# of independent K_2	$N_G \cdot (N_G + 1) \cdot (n_{\max} - 1)/2$
# of independent K_5	$N_G \cdot (N_G - 1)/2$
# of total independent K's	$N_G \cdot (N_G + 1) \cdot n_{\max}/2 - N_G + 1$

The temperature dependency of the chemical equilibrium constants is described by the van't Hoff equation (see eq (12)) with the two parameters A_j and B_j. The parameter B_j can be further used to determine the reaction enthalpy $\Delta_{\mathrm{R}} h_j$ of reaction j

$$\Delta_{\mathrm{R}} h_j/(\mathrm{J/mol}) = -B_j \cdot 8.314 \tag{40}$$

K_{XIII} is adopted from the literature [15]. The numerical values in temperature-dependent form are given in Table 10.

Table 10: Parameters for the calculation of the mole fraction-based chemical equilibrium constants K_j using the correlation $\ln K_j = A_j + B_j/(T/\mathrm{K})$.

K_j	A_j	B_j	Reference
K_{XIII}	6.829	−8252	[15]
$K_{\mathrm{XIV}}^{\mathrm{R,R}',n}$	−2.229	2993	[92]
$K_{\mathrm{XVII}}^{\mathrm{R,R}'}$	ln 4	0	This work

4.2.4 Subsystems and Extensions

For the following special cases, the model can be simplified:

a) There is only one alkyl group ($N_G = 1$): Reaction (XVII) does not have to be considered.

b) Neither FA, TRI nor any OAE_n with $n > 1$ are present ($n_{\max} = 1$): Reactions (XIII) and (XIV) do not have to be considered.

The model of the present work applies to the liquid phase. The respective equilibrium constants in the vapor phase are obtained via the vapor-liquid equilibrium of the mixture, see [93] for an example.

One has to be careful to apply the model in systems containing water or alcohols. Besides the additional reactions mentioned earlier, an activity-based equilibrium model should be used. The values of the mole fraction-based equilibrium constants reported in the present work provide, however, a good guess for the respective activity-based constants.

4.2.5 Implementation

In addition to the equilibrium conditions in eqs (37)-(39), mole balance equations are needed to determine the equilibrium composition of a mixture when the initial amounts of the components are specified. Subtracting the number of equilibrium conditions (total number of independent K's) from the number of components, cf. Table 9, one obtains N_G+1 missing material balances for N_G different alkyl groups present in the system. For example, one could balance the amounts of the N_G different alkyl groups and the overall amount of formaldehyde. Details on the explicit equations and the implementation in the software Matlab (R2020a, The MathWorks Inc.) in the present work are given in Appendix C.1.

4.3 Experiments

4.3.1 Chemicals

Methylal (Dimethoxymethan, Me,Me-OAE_1, >0.997 g/g) was purchased from Prefere. Ethylal (Diethoxymethan, Et,Et-OAE_1, >0.995 g/g) was purchased from Carl Roth, *n*-butylal (Dibutoxymethan, Bu,Bu-OAE_1, >0.97 g/g) and 1,3,5-trioxane (>0.99 g/g) were purchased from Sigma-Aldrich. The chemicals were used without further purification.

As described in previous chapters, the ion-exchange resin Amberlyst 46 was used as catalyst for the reaction experiments.

4.3.2 Analysis

NMR measurements were performed with an instrument from JEOL (JNM-ECS400) with a resonance frequency of 400 MHz. The samples were filled in 5 mm NMR tubes from Deutero, which were sealed after filling. The solvent $CDCl_3$ was used to assign peaks and to obtain the respective chemical shifts. To measure the chemical equilibrium, mixtures without $CDCl_3$ were analyzed. For the quantitative ^{13}C measurements, an inverse gated decoupling pulse sequence in combination with nuclear overhauser effect suppression was applied. The following acquisition parameters were chosen: acquisition time of 5.4 s, relaxation time of 90 s, flip angle of 90°, and 64 scans. The chosen NMR parameters have shown reliable performance when analyzing formaldehyde-containing mixtures [57, 92, 94] and were further tuned in prior test experiments. The temperature in the NMR spectrometer was set to 298 K for all measurements and controlled by the instrument with an accuracy of ±0.1 K. The NMR measurements yielded peaks for trioxane and the OAE of various chain lengths. Formaldehyde was not quantified in the spectra due to its small mole fraction [14, 16].

The model-based method from Matviychuk et al. [95] was used for the quantitative evaluation of the spectra. This method is based on Bayesian statistics and is especially suitable for spectra with strong overlapping peaks like in the present work [96, 97]. The software is written in python 3.7. Each component is characterized by all of its peaks and their relative quantity. For example, methylal (Me,Me-OAE_1, $H_3C-O-CH_2-O-CH_3$) shows one peak from the CH_2-group with the relative quantity 1 and one peak from the CH_3-groups with the relative quantity 2. Including this structural information ensured consistent evaluation of the individual peak areas. The software yielded an intensity for each specified component that was obtained from all individually assigned peaks weighted according to their relative quantity. The mole fractions were then determined from the component intensities divided by the sum of all component intensities. For single alkyl groups, e.g., in the system Me,Me-OAE + TRI, the chain length was limited to $n = 8$ in the software. Ethers up to $n = 5$ showed at least one non-overlapped peak enabling the determination of their mole fractions. Long-chain ethers with $n \geq 6$ were only included in the evaluation of the other components, i.e., the determination of the sum of all component intensities. For mixtures containing more than one alkyl group, peak overlapping was prominent. This limited the maximum evaluable chain length to $n = 3$ and the maximum chain length in the software to $n = 5$.

The chemical shifts in the NMR spectra were referenced to the solvent $CDCl_3$ (δ = 77.16 ppm (TMS)). Figure 22 shows a typical ^{13}C NMR spectrum of the system (Me,Me-OAE$_n$ + TRI) and information on the peak assignment. Peaks were assigned based on NMR measurements with the pure substances Me,Me-OAE$_1$ to Me,Me-OAE$_4$, Et,Et-OAE$_1$, Bu,Bu-OAE$_1$, and TRI. Due to their chemical similarity, findings from Me,Me-OAE were transferred to Et,Et-OAE and Bu,Bu-OAE. Details on the peak assignment of all components analyzed in the present work are given in Appendix C.2.

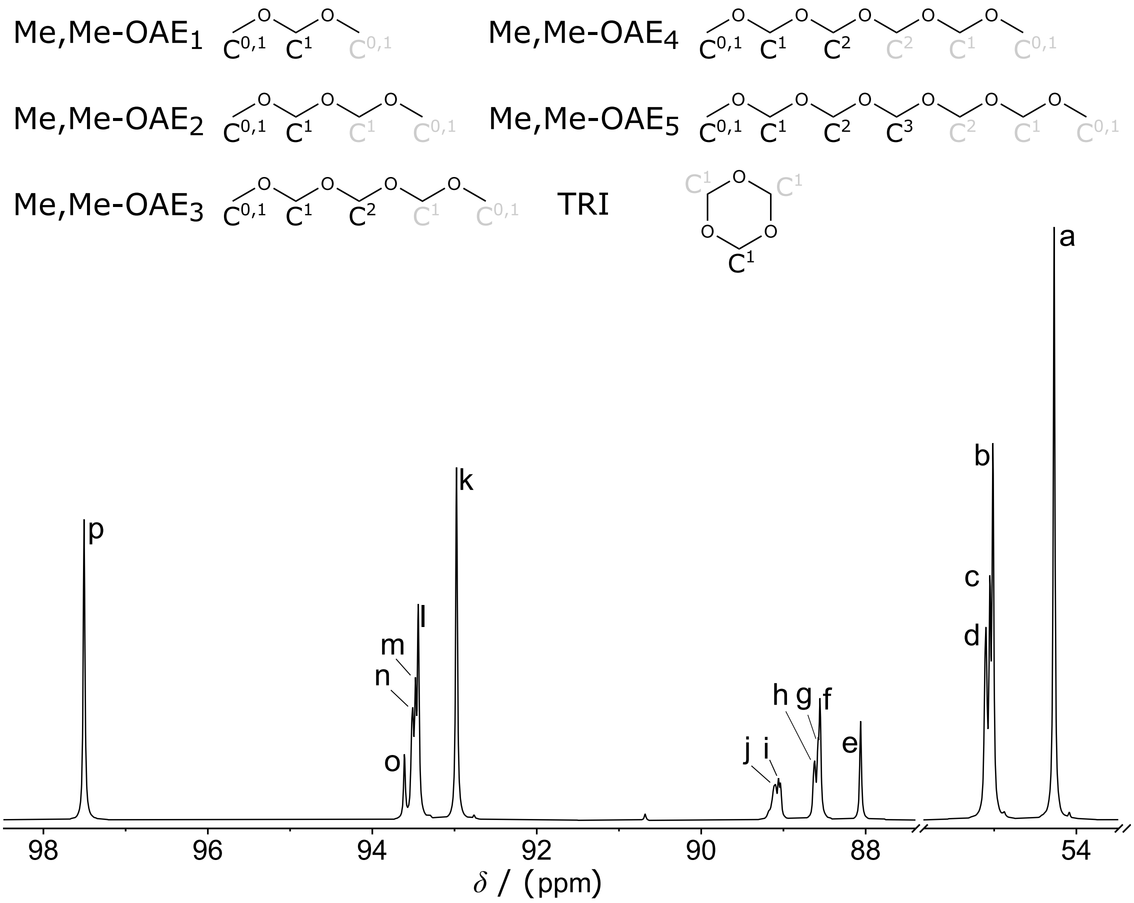

Figure 22: ^{13}C NMR spectrum and peak assignment for the system (Me,Me-OAE + TRI), reference = $CDCl_3$ (77.16 ppm (TMS)). Repeating carbon atoms are written in gray. Assigned peaks: a = $C^{0,1}_{\mathrm{Me,Me-OAE_1}}$, b = $C^{0,1}_{\mathrm{Me,Me-OAE_2}}$, c = $C^{0,1}_{\mathrm{Me,Me-OAE_3}}$, d = $C^{0,1}_{\mathrm{Me,Me-OAE_n}}(n \geq 4)$, e = $C^{2}_{\mathrm{Me,Me-OAE_3}}$, f = $C^{2}_{\mathrm{Me,Me-OAE_4}}$, g = $C^{2}_{\mathrm{Me,Me-OAE_5}}$, h = $C^{2}_{\mathrm{Me,Me-OAE_n}}(n \geq 6)$, i = $C^{3}_{\mathrm{Me,Me-OAE_5}}$, j = $C^{3}_{\mathrm{Me,Me-OAE_n}}(n \geq 6)$, k = $C^{1}_{\mathrm{Me,Me-OAE_2}}$, l = $C^{1}_{\mathrm{Me,Me-OAE_3}}$, m = $C^{1}_{\mathrm{Me,Me-OAE_4}}$, n = $C^{1}_{\mathrm{Me,Me-OAE_n}}(n \geq 5)$, o = C^{1}_{TRI}, p = $C^{1}_{\mathrm{Me,Me-OAE_1}}$.

4.3.3 Determination of Chemical Equilibrium Constants from NMR Data

In the presented model, cf. above, the equilibrium constant $K_{\mathrm{XIV}}^{\mathrm{R,R}',n}$ of the oligomerization reaction is assumed to be independent of the OAE considered and the chain length. In the experiments, the $K_{\mathrm{XIV}}^{\mathrm{R,R}',n}$ are determined individually for the various OAE and chain lengths to validate the model's assumption. These $K_{\mathrm{XIV}}^{\mathrm{R,R}',n}$ could however not be directly determined from NMR data using eq (38) as x_{FA} was not quantified from the NMR spectra. Using eq (37) and the well-known constant K_{XIII} [15], cf. Table 10, eq (38) was transformed to:

$$K_{\mathrm{XIV}}^{\mathrm{R,R}',n} = \frac{1}{K_{\mathrm{XIII}}^{1/3}} \cdot \frac{x_{\mathrm{R,R'\text{-}OAE}_n}}{x_{\mathrm{R,R'\text{-}OAE}_{n-1}} \cdot x_{\mathrm{TRI}}^{1/3}} \qquad \forall\, \mathrm{R,R}' \in G,\;\; n > 1 \tag{41}$$

Equation (41) allows the determination of $K_{\mathrm{XIV}}^{\mathrm{R,R}',n}$ from the mole fractions obtained from the NMR spectra.

4.3.4 Reaction Experiments

Two different types of reaction experiments with different setups were performed in the present work. The reaction experiments E1-E4 were performed to determine the chemical equilibrium constants of the oligomerization reaction with formaldehyde at varying temperature in systems with single alkyl groups ($N_G = 1$). The experiments were carried out in the 0.5 L stainless steel stirred reactor that was described earlier in Section 2.3.3 at elevated temperatures and pressure. The experiments were performed according to the following procedure. Trioxane was dissolved in the ether and the reactor was filled with the solution. The dry catalyst Amberlyst 46 was added and the reactor was sealed pressure-tight. Remaining oxygen in the reactor was removed by multiple flushing with nitrogen. Using nitrogen, the reactor was pressurized to avoid boiling. The reaction solution was stirred continuously at 350 rpm and the temperature was controlled using an oil double-jacket and a thermostat. Samples were taken through a riser pipe equipped with a filter to prevent the catalyst from entering the sampling line. Through consecutive sampling at the lowest temperature (303.15 K), it was found that the composition did not change anymore after a maximum of 12 h. Samples were taken not earlier than 16 h after the temperature was constant. The samples were cooled down in a refrigerator and analyzed promptly after the experiment was finished. The initial weights of the experiments E1-E4 are given in Table 11. For each system, (Et,Et-OAE + TRI) and (Bu,Bu-OAE + TRI), two mixtures with different ether to trioxane ratios were prepared. Each mixture was investigated at four different temperatures (303.15 / 323.15 / 343.15 / 363.15 K).

Table 11: Overview of initial weights of the components of reaction experiments E1–E11.

	$m^0_{\mathrm{Me,Me-OAE_1}}$ g	$m^0_{\mathrm{Et,Et-OAE_1}}$ g	$m^0_{\mathrm{Bu,Bu-OAE_1}}$ g	m^0_{TRI} g	m^0_{cat} g
E1	-	323.0	-	80.60	26.18
E2	-	332.7	-	66.55	30.04
E3	-	-	318.1	44.76	30.09
E4	-	-	319.3	38.91	29.56
E5	3.40	1.68	-	0.83	≈ 1
E6	2.25	9.56	-	2.01	≈ 1
E7	5.01	6.90	-	2.74	≈ 1
E8	7.69	-	5.31	3.17	≈ 1
E9	1.45	-	9.46	1.46	≈ 1
E10	3.21	-	6.72	1.91	≈ 1
E11	3.27	4.00	6.05	-	≈ 1

The second type of reaction experiment (E5-E11) focus on transacetalization ($N_G > 1$). These experiments were carried out in small glass vessels ($V \approx 20$ mL) at the constant temperature 298 K. After filling the initial mixture, around 1 g dry catalyst was added and the vessels were capped. The vessels were kept in a water bath at 298 K and stirred continuously with magnetic stirrers. At least two consecutive samples were taken at intervals of several hours to check if the chemical equilibrium was already reached. The first sample was taken not earlier than 72 h. Again, the samples were stored refrigerated and were analyzed promptly after the experiment was finished. The initial weights of the reaction mixtures for the experiments E5-E11 are given in Table 11.

4.4 Results and Discussion

4.4.1 Chemical Equilibrium of the Formaldehyde Oligomerization

The numerical results from the NMR analysis of the equilibrium compositions of the reaction experiments are tabulated in Appendix C.3. The chemical equilibrium constants for the oligomerization reactions of formaldehyde with $\mathrm{R,R'-OAE}_n$ were determined from the experimental results as described above. For reaction mixtures with single alkyl groups (E1-E4), OAE up to the chain length n = 5 could be analyzed with the presented NMR method. This results in four different values for the chemical equilibrium constant $K_{\mathrm{XIV}}^{\mathrm{R,R}',n}$ per mixture at each temperature. For reaction mixtures with more than one alkyl group present (E5-E10), OAE up to the chain length n = 3 could be analyzed resulting in two different values for the chemical equilibrium constant $K_{\mathrm{XIV}}^{\mathrm{R,R}',n}$ per mixture. All determined values for $K_{\mathrm{XIV}}^{\mathrm{R,R}',n}$ are depicted as symbols in Figure 23.

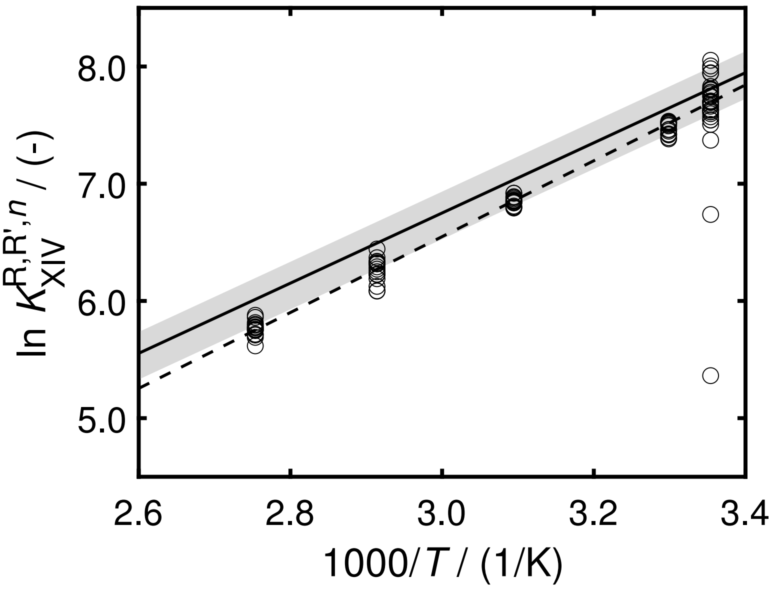

Figure 23: Van't Hoff plot for the mole fraction-based chemical equilibrium constant of the oligomerization reaction of $\mathrm{R,R}'$-OAE_n with formaldehyde. The symbols represent the values for $K_{\mathrm{XIV}}^{\mathrm{R,R}',n}$ determined from the experimental results of the reaction experiments E1-E10 for all alkyl groups and chain lengths. The solid line represents the correlation from Kircher et al. [92] including a relative error of ±20% (gray area). The dashed line represents the correlation fitted to the experimental results of the present work (see Table 12).

The figure illustrates that most of the values at each temperature, determined from the mole fractions of OAE with various alkyl groups and chain lengths, show only slight scattering. The large deviations of two individual values at T = 298 K originate from mole fraction values <0.01 mol/mol that are subject to large relative uncertainty. Despite these two outliers, the determined values for $K_{\mathrm{XIV}}^{\mathrm{R,R}',n}$ fit well together for all temperatures, even for asymmetric ethers. This indicates that neither the alkyl group nor the chain length significantly affects the chemical equilibrium of the oligomerization reaction. This is in line with the literature [14, 16, 92]. The values determined from the experiments of the present work were used to fit the parameters of the temperature-dependent correlation (eq (12)) by the least square method. The two outliers were excluded from the fit. The parameter values are shown in Table 12 and the resulting correlation is depicted as dashed line in Figure 23.

Table 12: Parameters for the calculation of the mole fraction-based chemical equilibrium constants $K_{\mathrm{XIV}}^{\mathrm{R,R}',n}$ using the correlation $\ln K_j = A_j + B_j/(T/K)$.

	A_j	B_j	Reference
$K_{XIV}^{\mathrm{R,R}',n}$	−3.162	3237	This work

The correlation for the generalized equilibrium constant from Kircher et al. [92] is also depicted in Figure 23 as solid line. The values for $K_{\mathrm{XIV}}^{\mathrm{R,R}',n}$ determined from the experiments of the present work are slightly smaller compared to the correlation. This systematic deviation was also reported for Me,Me-OAE$_n$ [92] and could indicate that ethers generally show slightly smaller values for $K_{\mathrm{XIV}}^{\mathrm{R,R}',n}$ compared to alcohols. (The correlation from Kircher et al. [92] was mainly derived from experiments with alcohols and water.) The temperature dependence of $K_{\mathrm{XIV}}^{\mathrm{R,R}',n}$, which is illustrated by the slope of both correlation lines, is, however, very similar. Comparing the reaction enthalpies, derived from the parameter values of both correlations in combination with eq (40), reveals—unsurprisingly—only a small difference between the correlation from Kircher et al. [92] ($\Delta_{\mathrm{R}} h_j = -24.9$ J/mol) and the correlation from the present work ($\Delta_{\mathrm{R}} h_j = -26.9$ J/mol). Both values show that the oligomerization reaction is slightly exothermic.

4.4.2 Model Sensitivity to Chemical Equilibrium Constants

Even though small deviations for $K_{\mathrm{XIV}}^{\mathrm{R,R}',n}$ between the correlation from Kircher et al. [92] and the experimental values of the present work have been detected in the previous section, their actual impact on the chemical equilibrium composition from model calculations is small as shown in the following. In a sensitivity study, the chemical equilibrium constant $K_{\mathrm{XIV}}^{\mathrm{R,R}',n}$ was systematically varied and the chemical equilibrium composition was calculated with the presented model. The general equilibrium constant from Kircher et al. [92] was used for the base case. A mixture of Me,Me-OAE$_1$, Et,Et-OAE$_1$, and TRI ($x^0_{\mathrm{Me,Me-OAE_1}} = x^0_{\mathrm{Et,Et-OAE_1}} = 0.414$ mol/mol, $x^0_{\mathrm{TRI}} = 0.172$ mol/mol) at $T = 298$ K was chosen for the study. The mole fraction ratio $x_i/x_{i,\mathrm{base}}$ of the considered case to the base case was used to illustrate the impact of the applied changes of $K_{\mathrm{XIV}}^{\mathrm{R,R}',n}$ in Figure 24. As all ethers (symmetric and asymmetric) are treated equally in the model regarding the oligomerization reaction, the relative impact of the chemical equilibrium constant $K_{\mathrm{XIV}}^{\mathrm{R,R}',n}$ is the same for all ethers. Therefore, the relative deviations in Figure 24 are condensed to only one ether per chain length.

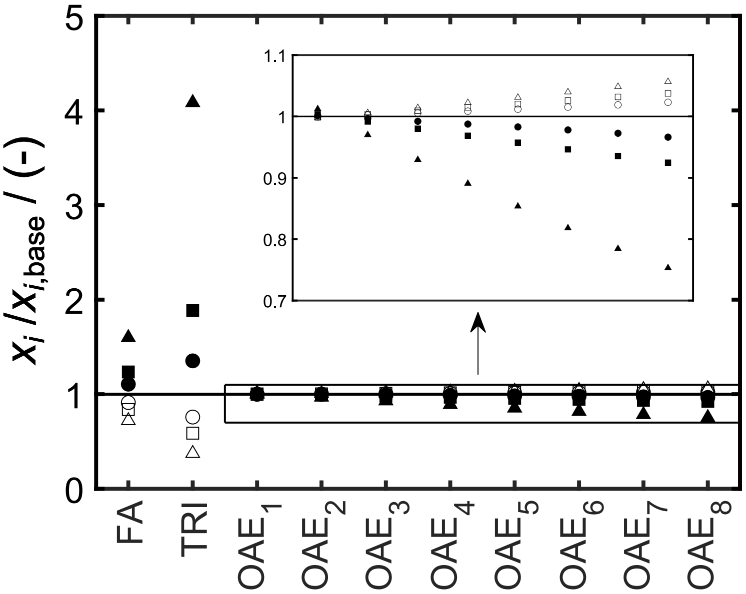

Figure 24: Model sensitivity to the chemical equilibrium constant $K_{\mathrm{XIV}}^{\mathrm{R,R'},n}$ along mole fraction ratios. The model results were obtained for a mixture of 1,1-OAE, 2,2-OAE, and TRI ($x^0_{\mathrm{Me,Me-OAE_1}}$ = $x^0_{\mathrm{Et,Et-OAE_1}}$ = 0.414 mol/mol, x^0_{TRI} = 0.172 mol/mol) at T = 298 K. Relative results are equivalent for all OAE independent of the end group. $1.4 \cdot K_{\mathrm{XIV}}^{\mathrm{R,R'},n}$(△), $1.2 \cdot K_{\mathrm{XIV}}^{\mathrm{R,R'},n}$(□), $1.1 \cdot K_{\mathrm{XIV}}^{\mathrm{R,R'},n}$(○), $0.9 \cdot K_{\mathrm{XIV}}^{\mathrm{R,R'},n}$ (●), $0.8 \cdot K_{\mathrm{XIV}}^{\mathrm{R,R'},n}$ (■), $0.6 \cdot K_{\mathrm{XIV}}^{\mathrm{R,R'},n}$ (▲).

The figure shows that the largest relative changes occur for the mole fractions of formaldehyde and trioxane. These large relative changes transfer, however, to relatively small absolute changes as these two mole fractions are typically <0.01 mol/mol. The relative impact of $K_{\mathrm{XIV}}^{\mathrm{R,R'},n}$ on the OAE is smaller compared to trioxane but rises with increasing chain length. That is not surprising as $K_{\mathrm{XIV}}^{\mathrm{R,R'},n}$ influences each subsequent chain prolongation. Nevertheless, the total impact of $K_{\mathrm{XIV}}^{\mathrm{R,R'},n}$ remains rather small for all chain lengths. Varying $K_{\mathrm{XIV}}^{\mathrm{R,R'},n}$ by ±20% results in the maximum relative and absolute deviations of the OAE mole fractions of 8% and 0.001 mol/mol, respectively.

The relative deviation of ±20% of $K_{\mathrm{XIV}}^{\mathrm{R,R'},n}$ is depicted in Figure 23 as a gray area for illustration. Most of the values obtained from the experiments in the present work lie within this range. This indicates that using the general equilibrium constant in model calculations results in sufficient accuracy when calculating mole fractions.

4.4.3 Chemical Equilibrium of the Transacetalization

In the model of the present work, it is assumed that the transacetalization reaction (XVII) is solely determined by statistical distribution of the alkyl groups leading to the constant value $K_{\mathrm{XVII}}^{\mathrm{R,R}',n}$ = 4, independent of the alkyl groups and the chain length. The values of $K_{\mathrm{XVII}}^{\mathrm{R,R}',n}$ determined from the experimental results of the present work are depicted in Figure 25 for n = 1–3 and three different alkyl group combinations. For chain lengths $n < 3$, the values slightly scatter around $K_{\mathrm{XVII}}^{\mathrm{R,R}',n}$ = 4, and all values but one are in the range ±20%. For n = 3, scattering is intensified and two values with large deviations are detected. These values ($K_{\mathrm{XVII}}^{\mathrm{R,R}',n}$ = 15.7/57.0) are not shown in the graph. As described earlier in the discussion of the oligomerization reaction (see Figure 23), these outliers originate from mole fraction values <0.01 mol/mol that are subject to large relative uncertainty. The intensified scattering for n = 3 and the strong outliers clearly illustrate that the evaluation of the NMR spectra is especially challenging for long-chain OAE with their small and overlapping peaks. However, based on the presented results, especially for chain lengths n = 1 and n = 2, the assumption of a statistical distribution of the alkyl groups is confirmed.

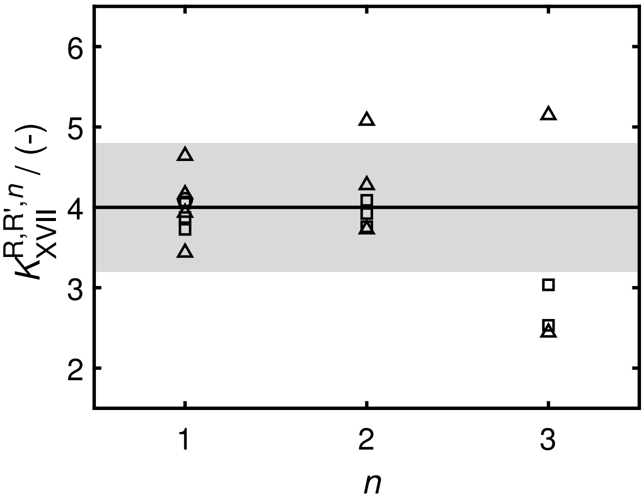

Figure 25: Values of K_{XVII} determined from the results of the experiments E5-E11 depicted for different alkyl group combinations (Me,Et-OAE$_n$ (△), Me,Bu-OAE$_n$ (□), Et,Bu-OAE$_n$ (○)) and chain lengths n. The solid line represents the constant value K_{XVII} = 4 including a relative error of ±20% (gray area).

Note that all the presented results in Figure 25 were obtained from experiments at T = 298.15 K (experiments E5-E11). The influence of the temperature could therefore not be examined. However, a temperature influence is not expected as the confirmed value $K_{\mathrm{XVII}}^{\mathrm{R,R}',n}$ = 4 is based solely on statistics.

4.4.4 Model Performance

To evaluate the overall performance of the model, the mole fractions of selected experiments are compared to model results in Figures 26 and 27. The diagrams of the remaining experiments are shown in Appendix C.4 as the qualitative results do not differ from the results shown in the main part.

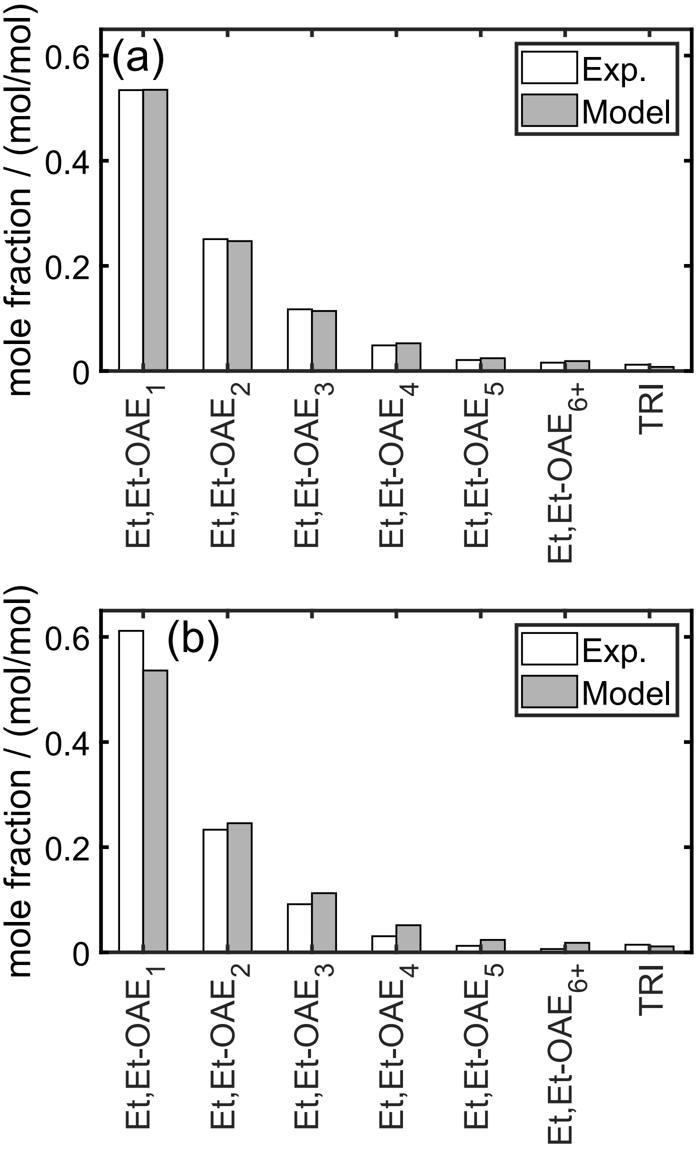

Figure 26: Comparison between the experiment and the model results for reaction experiment E1 ((a) T = 303.15 K, (b) T = 363.15 K).

Figure 26 shows the distribution of the mole fractions of Et,Et-OAE with different chain lengths from the reaction experiment E1 at two different temperatures. The experimental results at T = 303.15 K (diagram (a)) are well described by the model. However, larger deviations between experiment and model are revealed when comparing the results at T = 363.15 K (diagram (b)). The mole fractions from the model are too small for OAE_1 and rather too large for the other OAE. The more pronounced deviations with rising temperature between experiment and model are also detected for the reaction experiments E2–E4 (see Appendix). The deviations are in line with the findings for the chemical equilibrium constant of the oligomerization that were discussed along Figure 23. Using the correlation from the present work (see Table 12 for parameters) improved the agreement with the experimental data (see Appendix), but deviations were still present. The deviations can therefore rather be attributed to the uncertainty in the evaluation of the NMR spectra of the samples that were taken at high temperature. With rising temperature in the experiments, peak overlapping intensified and the spectra showed unknown peaks. This impeded the evaluation of long-chain OAE and could further indicate the formation of side products.

The first two diagrams in Figure 27 show systems with initially two symmetric ethers and trioxane. The resulting compositions in chemical equilibrium with the formed asymmetric ethers are well described by the model. Even mixtures of Me,Me-OAE and Bu,Bu-OAE (diagram (b)) are determined correctly, despite their strongly differing end groups. Furthermore, the cumulative mole fractions of long-chain ethers with $n \geq 4$, which cannot be obtained individually from the presented analysis, (designated as OAE_{4+} in Figure 27), are calculated properly. Beyond that, the model offers a detailed evaluation of individual long-chain ethers ($n > 3$) and their mole fractions and overcomes the limitations of the analysis. This is based on the assumption that the presented chemical equilibrium constants from Table 10 also hold for long-chain ethers, which is very likely based on the experimental results. The diagram in Figure 27(c) shows the equilibrium composition of reaction experiment E11 where three different symmetric ethers reacted. The perfect match between the experiment and the model composition further corroborates the statistical distribution of the alkyl groups that was assumed in the model.

All experimental results from E1-E11 are plotted against their respective model results in the parity plot in Figure 28. The plot shows that most of the mole fractions lie within a band of ±10% which illustrates the good quality of the model. Large relative deviations of more than 10% originate from the experiments at T = 363.15 K and small mole fractions including the summarized OAE_{4+} and OAE_{6+} fractions. The mean absolute deviation of all considered mole fractions is 0.007 mol/mol. Considering the entirely predictive nature of the model and the discussed challenges in the analysis, the performance of the model is remarkable.

In the present work, a limited number of alkyl groups were studied: saturated, linear, and

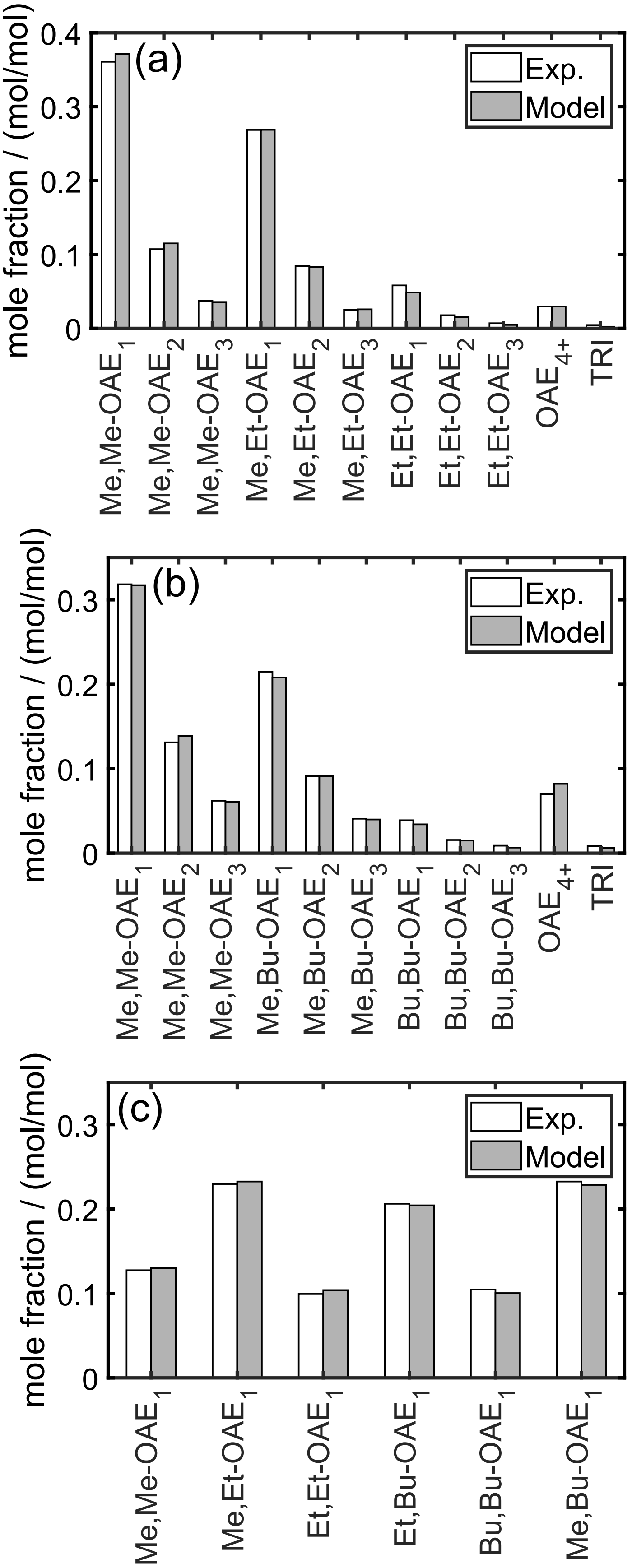

Figure 27: Comparison between the experiment and the model results for reaction experiments E5 (a), E8 (b), and E11 (c).

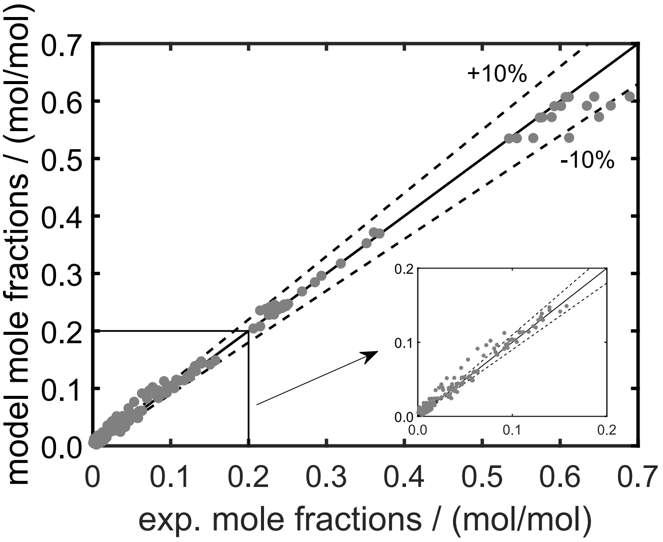

Figure 28: Parity plot to compare all experimental results from this work (E1-E11) with the model results.

short-chain alkyl groups that do not contain heteroatoms (Me, Et, Bu). The entirely predictive model performed very well in those systems. It remains open, how well the model can be also applied to more complex alkyl groups, e.g., branched groups containing functional groups. At some point, the alkyl groups are expected to influence the equilibrium through steric effects.

5 Conclusion

The transition of transportation is a major challenge on the way to sustainable use of resources that must be urgently addressed in light of the accelerating effects of global warming. The use of oxygenated compounds like poly(oxymethylene) dimethyl ethers in combustion engines instead of fossil fuels not just reduces CO_2 emissions but also substantially decreases the emission of harmful pollutants like soot and NO_x. Although promising process concepts to produce OME have been proposed, industrial-size plants are still scarce. The present work focused on the scale-up of a water-tolerant OME process and evaluates fundamental reactions of other ethers.

The formation of the side products methyl formate, formic acid, and trioxane was investigated in long-term reaction experiments in a laboratory-scale batch reactor with the ion-exchange resin Amberlyst 46 as heterogeneous catalyst. While trioxane is formed reversibly and is limited by the favorable chemical equilibrium, the formation of methyl formate and formic acid is unbound at the studied conditions, strongly linked, and more temperature-dependent than the formation of the main products. Enhanced formation of side products due to autocatalysis was observed at high concentrations of formic acid. A pseudo-homogeneous model was taken from literature [31] and extended to side product formation by introducing new reaction pathways and fitting the respective chemical equilibrium and kinetic parameters to the experimental data. The model calculations agree well with the experimental results and enable reliable process design. The developed kinetic model was used in a simulation of a water-tolerant OME process to examine the implications for the process design. The irreversibly formed side products methyl formate and formic acid accumulate within the recycle streams and, hence, their removal is indispensable. The level of the latter side products should be strictly limited to avoid their accelerated formation by autocatalysis. A purge stream was introduced to investigate the influence of the process conditions on the product loss. A trade-off between the required purge stream and the temperature in the reactor was detected. At a reactor temperature of 343.15 K around 2.7% of the product mass flow needs to be removed by the purge. The results demonstrate that the formation of side products needs to be considered in process design but is expected to be manageable by using selective removal methods or improved catalysts. Future work should focus on these measures and the evaluation of the implications for the other process units.

A continuous tubular reactor was built up as part of an $OME_{3–5}$ demo plant with a capacity of 8 t/a. The reactor shows ideal plug flow behavior for a wide range of operating conditions. $OME_{3–5}$ are successfully produced from feed mixtures containing methanol, aqueous formaldehyde, and large amounts of short-chain OME, and therefore feature similar compositions like in the OME process. Neither mass transfer limitations nor catalyst deactivation was observed during the reaction experiments with the tubular reactor. Further experimental studies regarding the stability of the ion-exchange resin Amberlyst 46 revealed that catalyst deactivation occurs by ion exchange when cations are present in the reacting solution. However, deactivation can most likely be avoided using a guard column, and the catalyst can be regenerated by acid treatment. Even though the consequences of repeated deactivation-regeneration cycles on the catalyst have not been investigated in the present work, the catalyst is expected to endure its performance as the deactivation originates from ion exchange, which is the standard application of the resin. An adjusted reaction model, whose parameters were fitted to the experimental results of the present work, is able to reliably describe the concentration profiles throughout the reactor for various operating conditions and feed compositions. A large-scale reactor with a capacity of 100 kt/a $OME_{3–5}$ was designed based on the adjusted model. The space–time yield was selected to be 10 $\mathrm{kg}/(\mathrm{kg}_{\mathrm{cat}} \cdot \mathrm{h})$, as a compromise between the required mass of catalyst and the necessary recycle streams. Heat transfer does not restrict the reactor design due to the small absolute value of the reaction enthalpy. Feasible reactor geometries with reasonable pressure drop are obtained when multitube reactors are considered. The presented model serves as a reliable starting point for the engineering of the industrial-scale reactor and therefore paves the way for the industrial-scale production of OME from methanol and formaldehyde. Future work should investigate the reactor performance during the combined operation of all process units to reveal potential implications that have not emerged from the separated reaction experiments. A special focus should be placed on the long-term catalyst stability.

A quantitative model to describe the chemical equilibrium of oligomerization and transacetalization reactions in OAE systems with various terminating alkyl groups was presented. The entirely predictive model is based on statistical considerations and the generalized equilibrium constant from Kircher et al. [92], and is applicable to oxymethylene oligomers with various terminating alkyl groups. Reaction experiments with mixtures comprising ethers with three different alkyl groups and trioxane were performed at different temperatures to elucidate the compositions in chemical equilibrium. The samples were analyzed by ^{13}C NMR spectroscopy and the peaks were assigned to the respective ethers. Even though the spectra were characterized by a multitude of overlapping peaks, oligomers with chain lengths up to $n = 5$ could be quantified from the spectra. The chemical equilibrium constants for the oligomerization reaction of the ethers with formaldehyde were determined from the experimental results of the present work. The comparison of the resulting values with the generalized equilibrium constant from Kircher et al. [92] revealed a good agreement independent of the chain length and the alkyl group. Despite slightly increasing deviations with rising temperature, the temperature dependence is still well represented by the generalized constant. The assumed statistical distribution of the alkyl groups in chemical equilibrium was confirmed by the experimental results of the present work. At some point, it is however expected that the alkyl group influences the equilibrium by steric effects, especially for highly branched groups containing functional groups. Finally, the mole fractions from the model calculations were compared to the experimental results of the present work. Despite slightly increasing deviations with rising temperature, the model well determined the composition in chemical equilibrium for various mixtures. Given its simplicity and the avoidance of any parameter fit, the model performance is remarkable. The presented model is able to reliably describe the chemical equilibrium of oligomerization and transacetalization reactions in OAE systems. Even though the model only covers water-free systems, it serves as a reliable base for future extensions with regard to more complex alkyl groups and systems containing alcohols and water. Including the latter components is expected to be particularly challenging as the resulting mixtures likely show non-ideal behavior. Future work should extend the model to reaction kinetics and phase equilibria, e.g., vapor-liquid, to be able to use it for the process design of novel production routes toward auspicious fuel candidates.

To summarize, the present work describes essential findings on the continuous production of OME from methanol and formaldehyde. The extensive experimental work served as a reliable base for model development, parameter fits, and process simulations. Setting up the continuous tubular reactor as part of the pilot plant was a major step toward the industrial application of the water-tolerant process route. It will be interesting to see which additional findings emerge from the continuous operation of the full pilot plant. In addition, by the evaluation and modeling of the chemical equilibrium in OAE systems, new research directions have been pointed out.

Literature

[1] European Environment Agency: Annual European Union greenhouse gas inventory 1990–2020 and inventory report 2022: Submission to the UNFCCC Secretariat, Copenhagen, Denmark, 2022.

[2] IPCC: Climate Change 2014: Synthesis Report. Contribution of Working Groups I, II and III to the Fifth Assessment Report of the Intergovernmental Panel on Climate Change, Geneva, Switzerland, 2014.

[3] I. Mead: International energy outlook 2017, US Energy Information Administration (2017).

[4] C. Hank, L. Lazar, F. Mantei, M. Ouda, R. J. White, T. Smolinka, A. Schaadt, C. Hebling, H.-M. Henning: Comparative well–to–wheel life cycle assessment of OME $_{3\text{–}5}$ synfuel production *via* the power-to-liquid pathway, Sustain. Energy Fuels 3 (2019) 3219–3233.

[5] J. Burger, M. Siegert, E. Ströfer, H. Hasse: Poly(oxymethylene) dimethyl ethers as components of tailored diesel fuel: Properties, synthesis and purification concepts, Fuel 89 (2010) 3315–3319.

[6] M. Härtl, P. Seidenspinner, E. Jacob, G. Wachtmeister: Oxygenate screening on a heavy-duty diesel engine and emission characteristics of highly oxygenated oxymethylene ether fuel OME 1, Fuel 153 (2015) 328–335.

[7] S. E. Iannuzzi, C. Barro, K. Boulouchos, J. Burger: POMDME-diesel blends: Evaluation of performance and exhaust emissions in a single cylinder heavy-duty diesel engine, Fuel 203 (2017) 57–67.

[8] M. Münz, A. Mokros, D. Töpfer, C. Beidl: OME-Assessment of Particle Emissions in Real Driving Conditions, MTZ worldwide 79 (2018) 16–21.

[9] A. D. Gelner, H. A. Beck, C. Pastoetter, M. Härtl, G. Wachtmeister: Ultra-low emissions of a heavy-duty engine powered with oxymethylene ethers (OME) under stationary and transient driving conditions, Int. J. Engine Res. (2021) 738–753.

[10] European Environment Agency: Air quality in Europe: 2018 report., Publications Office, LU, 2018.

[11] H. Liu, Z. Wang, Y. Li, Y. Zheng, T. He, J. Wang: Recent progress in the application in compression ignition engines and the synthesis technologies of polyoxymethylene dimethyl ethers, Appl. Energy 233-234 (2019) 599–611.

[12] A. Omari, B. Heuser, S. Pischinger, C. Rüdinger: Potential of long-chain oxymethylene ether and oxymethylene ether-diesel blends for ultra-low emission engines, Applied Energy 239 (2019) 1242–1249.

[13] D. Pélerin, K. Gaukel, M. Härtl, E. Jacob, G. Wachtmeister: Potentials to simplify the engine system using the alternative diesel fuels oxymethylene ether OME1 and OME3-6 on a heavy-duty engine, Fuel 259 (2020) 116231.

[14] N. Schmitz, F. Homberg, J. Berje, J. Burger, H. Hasse: Chemical Equilibrium of the Synthesis of Poly(oxymethylene) Dimethyl Ethers from Formaldehyde and Methanol in Aqueous Solutions, Ind. Eng. Chem. Res. 54 (2015) 6409–6417.

[15] D. Oestreich, L. Lautenschütz, U. Arnold, J. Sauer: Reaction kinetics and equilibrium parameters for the production of oxymethylene dimethyl ethers (OME) from methanol and formaldehyde, Chem. Eng. Sci. 163 (2017) 92–104.

[16] J. Burger, E. Ströfer, H. Hasse: Chemical Equilibrium and Reaction Kinetics of the Heterogeneously Catalyzed Formation of Poly(oxymethylene) Dimethyl Ethers from Methylal and Trioxane, Ind. Eng. Chem. Res. 51 (2012) 12751–12761.

[17] L. Lautenschütz, D. Oestreich, P. Haltenort, U. Arnold, E. Dinjus, J. Sauer: Efficient synthesis of oxymethylene dimethyl ethers (OME) from dimethoxymethane and trioxane over zeolites, Fuel Process. Technol. 165 (2017) 27–33.

[18] C. F. Breitkreuz, N. Schmitz, E. Ströfer, J. Burger, H. Hasse: Design of a Production Process for Poly(oxymethylene) Dimethyl Ethers from Dimethyl Ether and Trioxane, Chem. Ing. Tech. 90 (2018) 1489–1496.

[19] P. Haltenort, K. Hackbarth, D. Oestreich, L. Lautenschütz, U. Arnold, J. Sauer: Heterogeneously catalyzed synthesis of oxymethylene dimethyl ethers (OME) from dimethyl ether and trioxane, Catal. Commun. 109 (2018) 80–84.

[20] C. F. Breitkreuz, N. Hevert, N. Schmitz, J. Burger, H. Hasse: Synthesis of Methylal and Poly(oxymethylene) Dimethyl Ethers from Dimethyl Ether and Trioxane, Ind. Eng. Chem. Res. 61 (2022) 7810–7822.

[21] C. J. Baranowski, A. M. Bahmanpour, O. Kröcher: Catalytic synthesis of polyoxymethylene dimethyl ethers (OME): A review, Appl. Catal., B 217 (2017) 407–420.

[22] K. Hackbarth, P. Haltenort, U. Arnold, J. Sauer: Recent Progress in the Production, Application and Evaluation of Oxymethylene Ethers, Chem. Ing. Tech. 90 (2018) 1520–1528.

[23] M. Held, Y. Tönges, D. Pélerin, M. Härtl, G. Wachtmeister, J. Burger: On the energetic efficiency of producing polyoxymethylene dimethyl ethers from CO_2 using electrical energy, Energy Environ. Sci. 12 (2019) 1019–1034.

[24] S. Voelker, S. Deutz, J. Burre, D. Bongartz, A. Omari, B. Lehrheuer, A. Mitsos, S. Pischinger, A. Bardow, N. von der Assen: Blend for all or pure for few? Well-to-wheel life cycle assessment of blending electricity-based $OME_{3\text{-}5}$ with fossil diesel, Sustain. Energy Fuels 6 (2022) 1959–1973.

[25] F. Mantei, R. E. Ali, C. Baensch, S. Voelker, P. Haltenort, J. Burger, R.-U. Dietrich, N. v. d. Assen, A. Schaadt, J. Sauer, O. Salem: Techno-economic assessment and carbon footprint of processes for the large-scale production of oxymethylene dimethyl ethers from carbon dioxide and hydrogen, Sustain. Energy Fuels 6 (2022) 528–549.

[26] A. Peter, G. Stebens, J. F. Baumgärtner, E. Jacob, F. K. Mantei, M. Ouda, I. Krossing: Facile two-phase Catalysis: From Dimethoxymethane and Monomeric Formaldehyde towards Oxymethylene Ethers (OMEs), ChemCatChem 12 (2020) 2416–2420.

[27] R. Sun, C. Mebrahtu, J. P. Hofmann, D. Bongartz, J. Burre, C. H. Gierlich, P. J. C. Hausoul, A. Mitsos, R. Palkovits: Hydrogen-efficient non-oxidative transformation of methanol into dimethoxymethane over a tailored bifunctional Cu catalyst, Sustain. Energy Fuels 5 (2021) 117–126.

[28] M. Merko, G. W. Busser, M. Muhler: Non-oxidative Dehydrogenation of Methanol to Formaldehyde over Bulk β-Ga_2O_3, ChemCatChem (2022).

[29] J. Burre, D. Bongartz, S. Deutz, C. Mebrahtu, O. Osterthun, R. Sun, S. Völker, A. Bardow, J. Klankermayer, R. Palkovits, A. Mitsos: Comparing pathways for electricity-based production of dimethoxymethane as a sustainable fuel, Energy Environ. Sci. 14 (2021) 3686–3699.

[30] R. Sun, I. Delidovich, R. Palkovits: Dimethoxymethane as a Cleaner Synthetic Fuel: Synthetic Methods, Catalysts, and Reaction Mechanism, ACS Catal. 9 (2019) 1298–1318.

[31] N. Schmitz, J. Burger, H. Hasse: Reaction Kinetics of the Formation of Poly(oxymethylene) Dimethyl Ethers from Formaldehyde and Methanol in Aqueous Solutions, Ind. Eng. Chem. Res. 54 (2015) 12553–12560.

[32] R. Peláez, P. Marín, S. Ordóñez: Synthesis of poly(oxymethylene) dimethyl ethers from methylal and trioxane over acidic ion exchange resins: A kinetic study, Chem. Eng. J. 396 (2020) 125305.

[33] C. J. Baranowski, T. Fovanna, M. Roger, M. Signorile, J. McCaig, A. M. Bahmanpour, D. Ferri, O. Kröcher: Water Inhibition of Oxymethylene Dimethyl Ether Synthesis over Zeolite H-Beta: A Combined Kinetic and *in Situ* ATR-IR Study, ACS Catal. 10 (2020) 8106–8119.

[34] J. Zhang, D. Fang, D. Liu: Evaluation of Zr-Alumina in Production of Polyoxymethylene Dimethyl Ethers from Methanol and Formaldehyde: Performance Tests and Kinetic Investigations, Ind. Eng. Chem. Res. 53 (2014) 13589–13597.

[35] N. Schmitz, E. Ströfer, J. Burger, H. Hasse: Conceptual Design of a Novel Process for the Production of Poly(oxymethylene) Dimethyl Ethers from Formaldehyde and Methanol, Ind. Eng. Chem. Res. 56 (2017) 11519–11530.

[36] N. Schmitz, C. F. Breitkreuz, E. Ströfer, J. Burger, H. Hasse: Vapor-liquid equilibrium and distillation of mixtures containing formaldehyde and poly(oxymethylene) dimethyl ethers, Chem. Eng. Process. 131 (2018) 116–124.

[37] N. Schmitz, C. F. Breitkreuz, E. Ströfer, J. Burger, H. Hasse: Separation of water from mixtures containing formaldehyde, water, methanol, methylal, and poly(oxymethylene) dimethyl ethers by pervaporation, J. Membr. Sci. 564 (2018) 806–812.

[38] N. Schmitz, J. Burger, E. Ströfer, H. Hasse: From methanol to the oxygenated diesel fuel poly(oxymethylene) dimethyl ether: An assessment of the production costs, Fuel 185 (2016) 67–72.

[39] D. F. Rodríguez-Vallejo, A. Valente, G. Guillén-Gosálbez, B. Chachuat: Economic and life-cycle assessment of OME $_{3–5}$ as transport fuel: a comparison of production pathways, Sustain. Energy Fuels 5 (2021) 2504–2516.

[40] A. Ferre, J. Voggenreiter, Y. Tönges, J. Burger: Demonstration Plant for the Synthesis of OME Fuels, MTZ worldwide 82 (2021) 26–31.

[41] Y. Guan, W. Liu, D. Han: Comparative Study on Spray Auto-Ignition of Di-n-Butyl Ether and Diesel Blends at Engine-Like Conditions, J. Energy Resour. Technol. 143 (2021) 042302.

[42] L. Cai, F. vom Lehn, H. Pitsch: Higher Alcohol and Ether Biofuels for Compression-Ignition Engine Application: A Review with Emphasis on Combustion Kinetics, Energy Fuels 35 (2021) 1890–1917.

[43] L. Lautenschütz, D. Oestreich, P. Seidenspinner, U. Arnold, E. Dinjus, J. Sauer: Physico-chemical properties and fuel characteristics of oxymethylene dialkyl ethers, Fuel 173 (2016) 129–137.

[44] D. L. Bartholet, M. A. Arellano-Treviño, F. L. Chan, S. Lucas, J. Zhu, P. C. St. John, T. L. Alleman, C. S. McEnally, L. D. Pfefferle, D. A. Ruddy, B. Windom, T. D. Foust, K. F. Reardon: Property predictions demonstrate that structural diversity can improve the performance of polyoxymethylene ethers as potential bio-based diesel fuels, Fuel 295 (2021) 120509.

[45] M. A. Arellano-Treviño, D. Bartholet, A. T. To, A. W. Bartling, F. G. Baddour, T. L. Alleman, E. D. Christensen, G. M. Fioroni, C. Hays, J. Luecke, J. Zhu, C. S. McEnally, L. D. Pfefferle, K. F. Reardon, T. D. Foust, D. A. Ruddy: Synthesis of Butyl-Exchanged Polyoxymethylene Ethers as Renewable Diesel Blendstocks with Improved Fuel Properties, ACS Sustainable Chem. Eng. 9 (2021) 6266–6273.

[46] M. A. Arellano-Treviño, T. L. Alleman, R. Brim, A. T. To, J. Zhu, C. S. McEnally, C. Hays, J. Luecke, L. D. Pfefferle, T. D. Foust, D. A. Ruddy: Blended fuel property analysis of butyl-exchanged polyoxymethylene ethers as renewable diesel blendstocks, Fuel 322 (2022) 124220.

[47] C. J. Baranowski, A. M. Bahmanpour, F. Héroguel, J. S. Luterbacher, O. Kröcher: Prominent role of mesopore surface area and external acid sites for the synthesis of polyoxymethylene dimethyl ethers (OME) on a hierarchical H-ZSM-5 zeolite, Catal. Sci. Technol. 9 (2019) 366–376.

[48] J. Wu, H. Zhu, Z. Wu, Z. Qin, L. Yan, B. Du, W. Fan, J. Wang: High Si/Al ratio HZSM-5 zeolite: an efficient catalyst for the synthesis of polyoxymethylene dimethyl ethers from dimethoxymethane and trioxymethylene, Green Chem. 17 (2015) 2353–2357.

[49] J. Wu, S. Wang, H. Li, Y. Zhang, R. Shi, Y. Zhao: The Synergistic Effect of Acidic Properties and Channel Systems of Zeolites on the Synthesis of Polyoxymethylene Dimethyl Ethers from Dimethoxymethane and Trioxymethylene, Nanomaterials 9 (2019) 1192.

[50] Y. Liu, Y. Wang, W. Cai: A Synthesis, Process Optimization, and Mechanism Investigation for the Formation of Polyoxymethylene Dimethyl Ethers, Trans. Tianjin Univ. 25 (2019) 1–8.

[51] A. Zhenova, A. Pellis, R. A. Milescu, C. R. McElroy, R. J. White, J. H. Clark: Solvent Applications of Short-Chain Oxymethylene Dimethyl Ether Oligomers, ACS Sustainable Chem. Eng. 7 (2019) 14834–14840.

[52] G. de Gonzalo, A. R. Alcántara, P. Domínguez de María: Cyclopentyl Methyl Ether (CPME): A Versatile Eco-Friendly Solvent for Applications in Biotechnology and Biorefineries, ChemSusChem 12 (2019) 2083–2097.

[53] I. Hahnenstein, H. Hasse, C. G. Kreiter, G. Maurer: 1H- and 13C-NMR-Spectroscopic Study of Chemical Equilibria in Solutions of Formaldehyde in Water, Deuterium Oxide, and Methanol, Ind. Eng. Chem. Res. 33 (1994) 1022–1029.

[54] I. Hahnenstein, M. Albert, H. Hasse, C. G. Kreiter, G. Maurer: NMR Spectroscopic and Densimetric Study of Reaction Kinetics of Formaldehyde Polymer Formation in Water, Deuterium Oxide, and Methanol, Ind. Eng. Chem. Res. 34 (1995) 440–450.

[55] M. Maiwald, H. H. Fischer, M. Ott, R. Peschla, C. Kuhnert, C. G. Kreiter, G. Maurer, H. Hasse: Quantitative NMR Spectroscopy of Complex Liquid Mixtures: Methods and Results for Chemical Equilibria in Formaldehyde-Water-Methanol at Temperatures up to 383 K, Ind. Eng. Chem. Res. 42 (2003) 259–266.

[56] J. F. Walker: Formaldehyde, Reinhold Publ. Corp., 1964.

[57] M. Maiwald, T. Grützner, E. Ströfer, H. Hasse: Quantitative NMR spectroscopy of complex technical mixtures using a virtual reference: chemical equilibria and reaction kinetics of formaldehyde-water-1,3,5-trioxane, Anal. Bioanal. Chem. 385 (2006) 910–917.

[58] A. L. Balashov, V. L. Krasnov, S. M. Danov, A. Y. Chernov, A. V. Sulimov: Formation of Cyclic Oligomers in Concentrated Aqueous Solutions of Formaldehyde, J. Struct. Chem. 42 (2001) 398–403.

[59] T. Grützner, H. Hasse, N. Lang, M. Siegert, E. Ströfer: Development of a new industrial process for trioxane production, Chem. Eng. Sci. 62 (2007) 5613–5620.

[60] O. P. Törmäkangas, A. M. Koskinen: The Tishchenko reaction and its modifications in organic synthesis, Recent Res. Dev. Org. Chem 100 (2001) 225–255.

[61] R. Wang, Z. Wu, Z. Qin, C. Chen, H. Zhu, J. Wu, G. Chen, W. Fan, J. Wang: Graphene oxide: an effective acid catalyst for the synthesis of polyoxymethylene dimethyl ethers from methanol and trioxymethylene, Catal. Sci. Technol. 6 (2016) 993–997.

[62] J. Zhang, D. Liu: Preparation of a hydrophobic-hydrophilic adjustable catalyst surface for the controlled synthesis of polyoxymethylene dimethyl ethers: A potential replacement of diesel fuel, Int. J. Energy Res. 42 (2018) 1237–1246.

[63] B. Indu, W. R. Ernst, L. T. Gelbaum: Methanol-formic acid esterification equilibrium in sulfuric acid solutions: influence of sodium salts, Ind. Eng. Chem. Res. 32 (1993) 981–985.

[64] R. F. Schultz: Studies in Ester Hydrolysis Equilibria-Formic Acid Esters, J. Am. Chem. Soc. 61 (1939) 1443–1447.

[65] C. G. Swain, A. L. Powell, W. A. Sheppard, C. R. Morgan: Mechanism of the Cannizzaro reaction, J. Am. Chem. Soc. 101 (1979) 3576–3583.

[66] A. E. Russell, S. P. Miller, J. P. Morken: Efficient Lewis Acid Catalyzed Intramolecular Cannizzaro Reaction, J. Org. Chem. 65 (2000) 8381–8383.

[67] E. von Harbou, A. Yazdani, M. Schmitt, C. Großmann, H. Hasse: Reaction Kinetics for Reactive Distillation Using Different Laboratory Reactors, Ind. Eng. Chem. Res. 52 (2013) 624–637.

[68] S. D. Alexandratos: Ion-Exchange Resins: A Retrospective from *Industrial and Engineering Chemistry Research*, Ind. Eng. Chem. Res. 48 (2009) 388–398.

[69] J.-O. Drunsel, M. Renner, H. Hasse: Experimental study and model of reaction kinetics of heterogeneously catalyzed methylal synthesis, Chem. Eng. Res. Des. 90 (2012) 696–703.

[70] U. Weidlich, J. Gmehling: A modified UNIFAC model. 1. Prediction of VLE, hE, and. gamma.. infin., Ind. Eng. Chem. Res. 26 (1987) 1372–1381.

[71] D. Constantinescu, J. Gmehling: Further Development of Modified UNIFAC (Dortmund): Revision and Extension 6, J. Chem. Eng. Data 61 (2016) 2738–2748.

[72] O. Jogunola, T. Salmi, K. Eränen, J. Wärnå, M. Kangas, J.-P. Mikkola: Reversible Autocatalytic Hydrolysis of Alkyl Formate: Kinetic and Reactor Modeling, Ind. Eng. Chem. Res. 49 (2010) 4099–4106.

[73] O. Jogunola, T. Salmi, J. Wärnå, J.-P. Mikkola: Kinetic studies of alkyl formate hydrolysis using formic acid as a catalyst, J. Chem. Technol. Biotechnol. 87 (2012) 286–293.

[74] H. D. Ta, A. Seidel-Morgenstern: Impact of Liquid-Phase Volume Changes on Estimating Reaction Rate Parameters: The Homogeneously Catalyzed Hydrolysis of Methyl Formate, Ind. Eng. Chem. Res. 56 (2017) 13086–13095.

[75] D. Painer, S. Lux: Intramolecular Catalysis in Carboxylic Acid Esterification: Modeling of Single- and Multi-Acid Esterification, Ind. Eng. Chem. Res. 58 (2019) 1133–1141.

[76] B. E. Poling, J. M. Prausnitz, J. P. O'Connell: The properties of gases and liquids, 5 ed., McGraw-Hill, New York, 2001.

[77] A. Chakrabarti, M. Sharma: Cationic ion exchange resins as catalyst, Reactive Polymers 20 (1993) 1–45.

[78] L. Petrus, E. J. Stamhuis, G. E. Joosten: Thermal deactivation of strong-acid ion-exchange resins in water, Ind. Eng. Chem. Prod. Res. Dev. 20 (1981) 366–371.

[79] V. Malshe, E. Sujatha: Regeneration and reuse of cation-exchange resin catalyst used in alkylation of phenol, React. Funct. Polym. 35 (1997) 159–168.

[80] M. D. Girolamo, M. Marchionna: Acidic and basic ion exchange resins for industrial applications, J. Mol. Catal. A Chem. 177 (2001) 33–40.

[81] R. Aris: On the dispersion of a solute in a fluid flowing through a tube, Proc. R. Soc. A: Math. Phys. Eng. Sci. 235 (1956) 67–77.

[82] G. I. Taylor: Dispersion of soluble matter in solvent flowing slowly through a tube, Proc. R. Soc. A: Math. Phys. Eng. Sci. 219 (1953) 186–203.

[83] P. V. Danckwerts: Continuous flow systems: distribution of residence times, Chem. Eng. Sci. 2 (1953) 1–13.

[84] O. Levenspiel: Chemical reaction engineering, 3rd ed ed., Wiley, New York, 1999.

[85] G. Sampath, S. Kannan: Fructose dehydration to 5-hydroxymethylfurfural: Remarkable solvent influence on recyclability of Amberlyst-15 catalyst and regeneration studies, Catal. Commun. 37 (2013) 41–44.

[86] M. R. Nanda, Z. Yuan, W. Qin, H. S. Ghaziaskar, M.-A. Poirier, C. C. Xu: Catalytic conversion of glycerol to oxygenated fuel additive in a continuous flow reactor: Process optimization, Fuel 128 (2014) 113–119.

[87] S. Ergun: Fluid flow through packed columns, Chem. Eng. Prog. 48 (1952) 89–94.

[88] K. Bischoff, O. Levenspiel: Fluid dispersion-generalization and comparison of mathematical models-II comparison of models, Chem. Eng. Sci. 17 (1962) 257–264.

[89] L. C. Young, B. A. Finlayson: Axial dispersion in nonisothermal packed bed chemical reactors, Ind. Eng. Chem. Fundam. 12 (1973) 412–422.

[90] P. Haltenort, L. Lautenschütz, U. Arnold, J. Sauer: (Trans)acetalization Reactions for the Synthesis of Oligomeric Oxymethylene Dialkyl Ethers Catalyzed by Zeolite BEA25, Top. Catal. (2019) 551–559.

[91] M. Drexler, P. Haltenort, T. A. Zevaco, U. Arnold, J. Sauer: Synthesis of tailored oxymethylene ether (OME) fuels via transacetalization reactions, Sustain. Energy Fuels 5 (2021) 4311–4326.

[92] R. Kircher, N. Schmitz, J. Berje, K. Münnemann, W. R. Thiel, J. Burger, H. Hasse: Generalized Chemical Equilibrium Constant of Formaldehyde Oligomerization, Ind. Eng. Chem. Res. 59 (2020) 11431–11440.

[93] M. Dyga, A. Keller, H. Hasse: Vapor-Liquid Equilibria and Chemical Equilibria in the System (Formaldehyde + Water + Isoprenol), Ind. Eng. Chem. Res. 60 (2021) 4471–4483.

[94] J. Berje, J. Burger, H. Hasse, J. Baldamus: NMR spectroscopic study of chemical equilibria in solutions of formaldehyde, water, and butynediol, AIChE J. 63 (2017) 4442–4450.

[95] Y. Matviychuk, E. von Harbou, D. J. Holland: An experimental validation of a Bayesian model for quantification in NMR spectroscopy, J. Magn. Reson. 285 (2017) 86–100.

[96] Y. Matviychuk, E. Steimers, E. von Harbou, D. J. Holland: Bayesian approach for automated quantitative analysis of benchtop NMR data, J. Magn. Reson. 319 (2020) 106814.

[97] E. Steimers, Y. Matviychuk, A. Friebel, K. Münnemann, E. Harbou, D. J. Holland: A comparison of non-uniform sampling and model-based analysis of NMR spectra for reaction monitoring, Magn. Reson. Chem. 59 (2021) 221–236.

[98] T.-P. Mai: Experimental investigation of heterogeneously catalyzed hydrolysis of esters, Ph.D. thesis, Otto-von-Guericke-Universität Magdeburg, Magdeburg, 2006.

[99] A. Brächer: Advances in Flow NMR Spectroscopy in Chemical Reaction Engineering, Ph.D. thesis, Technische Universität Kaiserslauterny, Laboratory of Engineering Thermodynamics, 2017.

[100] W. V. Wilding, T. A. Knotts, N. F. Giles, R. L. Rowley: DIPPR Data Compilation of Pure Chemical Properties, Design Institute for Physical Properties, AIChE: New York, NY, 2020.

[101] H. W. Xiang, A. Laesecke, M. L. Huber: A New Reference Correlation for the Viscosity of Methanol, J. Phys. Chem. Ref. Data 35 (2006) 1597–1620.

[102] J. Kestin, M. Sokolov, W. A. Wakeham: Viscosity of liquid water in the range -8 °C to 150 °C, J. Phys. Chem. Ref. Data 7 (1978) 941–948.

[103] A. Ferre, J. Burger: Coadsorption Equilibria on Molecular Sieves 3A and Densities of Liquid Mixtures Containing Formaldehyde, Methanol, and Water at 295.15 and 313.15 K, Ind. Eng. Chem. Res. 60 (2021) 15256–15263.

[104] J. G. M. Winkelman, A. A. C. M. Beenackers: Correlations for the Density and Viscosity of Aqueous Formaldehyde Solutions, Ind. Eng. Chem. Res. 39 (2000) 557–562.

[105] J. Burger: A novel Process for the Production of Diesel Fuel Additives by Hierarchical Design, Ph.D. thesis, Technische Universität Kaiserslautern, Kaiserslautern, 2012.

Appendix

A Formation of Side Products and Implications for Process Design

A.1 True and Overall Composition

A general description of the conversion between true, neutral overall, and acidic overall mole and mass fractions is listed below. Vectors and matrices are denoted by bold small or bold capital letters, respectively. Different types of matrix operations are used and described in the following.

$\cdot$	multiplication scalar with matrix
$\times$	matrix multiplication
$\circ$	element-wise multiplication
$\mathbf{m}^{-1}$	element-wise inverted matrix

Definition of mole and mass fraction vectors:

$$\mathbf{x},\mathbf{w} = \begin{pmatrix} x_{\mathrm{FA}}, w_{\mathrm{FA}} \\ x_{\mathrm{WA}}, w_{\mathrm{WA}} \\ x_{\mathrm{ME}}, w_{\mathrm{ME}} \\ x_{\mathrm{MG_1}}, w_{\mathrm{MG_1}} \\ \vdots \\ x_{\mathrm{MG_P}}, w_{\mathrm{MG_P}} \\ x_{\mathrm{HF_1}}, w_{\mathrm{HF_1}} \\ \vdots \\ x_{\mathrm{HF_Q}}, w_{\mathrm{HF_Q}} \\ x_{\mathrm{OME_1}}, w_{\mathrm{OME_1}} \\ \vdots \\ x_{\mathrm{OME_O}}, w_{\mathrm{OME_O}} \\ x_{\mathrm{TRI}}, w_{\mathrm{TRI}} \\ x_{\mathrm{MEFO}}, w_{\mathrm{MEFO}} \\ x_{\mathrm{FOAC}}, w_{\mathrm{FOAC}} \end{pmatrix} \quad \tilde{\mathbf{x}},\tilde{\mathbf{w}} = \begin{pmatrix} \tilde{x}_{\mathrm{FA}}, \tilde{w}_{\mathrm{FA}} \\ \tilde{x}_{\mathrm{WA}}, \tilde{w}_{\mathrm{WA}} \\ \tilde{x}_{\mathrm{ME}}, \tilde{w}_{\mathrm{ME}} \\ \tilde{x}_{\mathrm{OME_1}}, \tilde{w}_{\mathrm{OME_1}} \\ \vdots \\ \tilde{x}_{\mathrm{OME_O}}, \tilde{w}_{\mathrm{OME_O}} \\ \tilde{x}_{\mathrm{TRI}}, \tilde{w}_{\mathrm{TRI}} \\ \tilde{x}_{\mathrm{MEFO}}, \tilde{w}_{\mathrm{MEFO}} \\ \tilde{x}_{\mathrm{FOAC}}, \tilde{w}_{\mathrm{FOAC}} \end{pmatrix} \quad \hat{\mathbf{x}},\hat{\mathbf{w}} = \begin{pmatrix} \hat{x}_{\mathrm{FA}}, \hat{w}_{\mathrm{FA}} \\ \hat{x}_{\mathrm{WA}}, \hat{w}_{\mathrm{WA}} \\ \hat{x}_{\mathrm{ME}}, \hat{w}_{\mathrm{ME}} \\ \hat{x}_{\mathrm{TRI}}, \hat{w}_{\mathrm{TRI}} \\ \hat{x}_{\mathrm{MEFO}}, \hat{w}_{\mathrm{MEFO}} \\ \hat{x}_{\mathrm{FOAC}}, \hat{w}_{\mathrm{FOAC}} \end{pmatrix}$$

Definition of molar mass vectors:

$$\mathbf{m} = \begin{pmatrix} M_{\mathrm{FA}} \\ M_{\mathrm{WA}} \\ M_{\mathrm{ME}} \\ M_{\mathrm{MG_1}} \\ \vdots \\ M_{\mathrm{MG_P}} \\ M_{\mathrm{HF_1}} \\ \vdots \\ M_{\mathrm{HF_Q}} \\ M_{\mathrm{OME_1}} \\ \vdots \\ M_{\mathrm{OME_O}} \\ M_{\mathrm{TRI}} \\ M_{\mathrm{MEFO}} \\ M_{\mathrm{FOAC}} \end{pmatrix} \qquad \tilde{\mathbf{m}} = \begin{pmatrix} M_{\mathrm{FA}} \\ M_{\mathrm{WA}} \\ M_{\mathrm{ME}} \\ M_{\mathrm{OME_1}} \\ \vdots \\ M_{\mathrm{OME_O}} \\ M_{\mathrm{TRI}} \\ M_{\mathrm{MEFO}} \\ M_{\mathrm{FOAC}} \end{pmatrix} \qquad \hat{\mathbf{m}} = \begin{pmatrix} M_{\mathrm{FA}} \\ M_{\mathrm{WA}} \\ M_{\mathrm{ME}} \\ M_{\mathrm{TRI}} \\ M_{\mathrm{MEFO}} \\ M_{\mathrm{FOAC}} \end{pmatrix}$$

Definition of identity matrix $\mathbf{I}_i$:

$$\mathbf{I}_i = \begin{pmatrix} 1 & 0 & \cdots & 0 \\ 0 & 1 & \cdots & 0 \\ \vdots & \vdots & \ddots & \vdots \\ 0 & 0 & \cdots & 1 \end{pmatrix}_{i \times i}$$

Definition of zero matrix $0_{i \times j}$:

$$0_{i \times j} = \begin{pmatrix} 0 & \cdots & 0 \\ \vdots & \ddots & \vdots \\ 0 & \cdots & 0 \end{pmatrix}_{i \times j}$$

Definition of stoichiometric vector $\mathbf{s}_j$:

$$\mathbf{s}_j = \begin{pmatrix} 1 & 2 & 3 & \cdots & j \end{pmatrix}_{1 \times j}$$

Definition of vector of ones $\mathbf{j}_j$:

$$\mathbf{j}_j = \begin{pmatrix} 1 & 1 & \cdots & 1 \end{pmatrix}_{1\times j}$$

Definition of the stoichiometric matrices $\tilde{\mathbf{S}}$ and $\hat{\mathbf{S}}$:

$$\tilde{\mathbf{S}} = \left(\begin{array}{ccccc|c} 1 & 0 & 0 & \mathbf{s}_P & \mathbf{s}_Q & \\ 0 & 1 & 0 & \mathbf{j}_P & 0_{1\times Q} & 0_{3\times(3+O)} \\ 0 & 0 & 1 & 0_{1\times P} & \mathbf{j}_Q & \\ \hline \multicolumn{5}{c|}{0_{(3+O)\times(3+P+Q)}} & \mathbf{I}_{(3+O)} \end{array}\right) \qquad \hat{\mathbf{S}} = \left(\begin{array}{cccccc|c} 1 & 0 & 0 & \mathbf{s}_P & \mathbf{s}_Q & \mathbf{s}_O & \\ 0 & 1 & 0 & \mathbf{j}_N & 0_{1\times Q} & (-1)\cdot\mathbf{j}_O & 0_{3\times 3} \\ 0 & 0 & 1 & 0_{1\times P} & \mathbf{j}_Q & 2\cdot\mathbf{j}_O & \\ \hline \multicolumn{6}{c|}{0_{3\times(3+P+Q+O)}} & \mathbf{I}_3 \end{array}\right)$$

O, P, Q define the maximum chain length of $\mathrm{OME_n}$, $\mathrm{MG_n}$, and $\mathrm{HF_n}$, respectively.

Definition of molar correction terms $\tilde{\boldsymbol{\delta}}$ and $\hat{\boldsymbol{\delta}}$ to account for non-equimolar stoichiometry:

$$\tilde{\boldsymbol{\delta}} = \begin{pmatrix} 0 & 0 & 0 & \mathbf{s}_P & \mathbf{s}_Q & 0_{1\times(3+O)} \end{pmatrix}$$
$$\hat{\boldsymbol{\delta}} = \begin{pmatrix} 0 & 0 & 0 & \mathbf{s}_P & \mathbf{s}_Q & \mathbf{s}_O & 0_{1\times 3} \end{pmatrix}$$

Conversion between mole and mass fraction vectors (equivalent for $\mathbf{x}$, $\tilde{\mathbf{x}}$, $\hat{\mathbf{x}}$ and $\mathbf{w}$, $\tilde{\mathbf{w}}$, $\hat{\mathbf{w}}$, respectively):

$$\mathbf{w} = \frac{\mathbf{m} \circ \mathbf{x}}{\mathbf{m}^T \times \mathbf{x}} \qquad \mathbf{x} = \frac{\mathbf{m}^{-1} \circ \mathbf{w}}{(\mathbf{m}^{-1})^T \times \mathbf{w}}$$

Generalization of true mole and mass fractions $\mathbf{x}$, $\mathbf{w}$ to neutral overall mole and mass fractions $\tilde{\mathbf{x}}$, $\tilde{\mathbf{w}}$, respectively:

$$\tilde{\mathbf{x}} = \frac{1}{1 + (\tilde{\boldsymbol{\delta}} \times \mathbf{x})} \cdot \left(\tilde{S} \times \mathbf{x}\right)$$
$$\tilde{\mathbf{w}} = \tilde{\mathbf{m}} \circ \left(\tilde{S} \times \left(\tilde{\mathbf{m}}^{-1} \circ \mathbf{w}\right)\right)$$

Generalization of true mole and mass fractions $\mathbf{x}$, $\mathbf{w}$ to acidic overall mole and mass fractions $\hat{\mathbf{x}}$, $\hat{\mathbf{w}}$, respectively:

$$\hat{\mathbf{x}} = \frac{1}{1 + (\hat{\boldsymbol{\delta}} \times \mathbf{x})} \cdot \left(\hat{S} \times \mathbf{x}\right)$$
$$\hat{\mathbf{w}} = \hat{\mathbf{m}} \circ \left(\hat{S} \times \left(\hat{\mathbf{m}}^{-1} \circ \mathbf{w}\right)\right)$$

A.2 Chemical Equilibrium of the Esterification Reaction

Comparison of the chemical equilibrium constant K_{XI} (esterification of formic acid with methanol to methyl formate and water) obtained from the fit to experimental data of this work with literature in Figure 29. The shown values for K_{XI} are based on mole fractions or molar concentrations, invariably. As written in Section 2.4.1, the values for K_{XI} scatter strongly with composition. K_{XI} was therefore fitted to experimental data of this work.

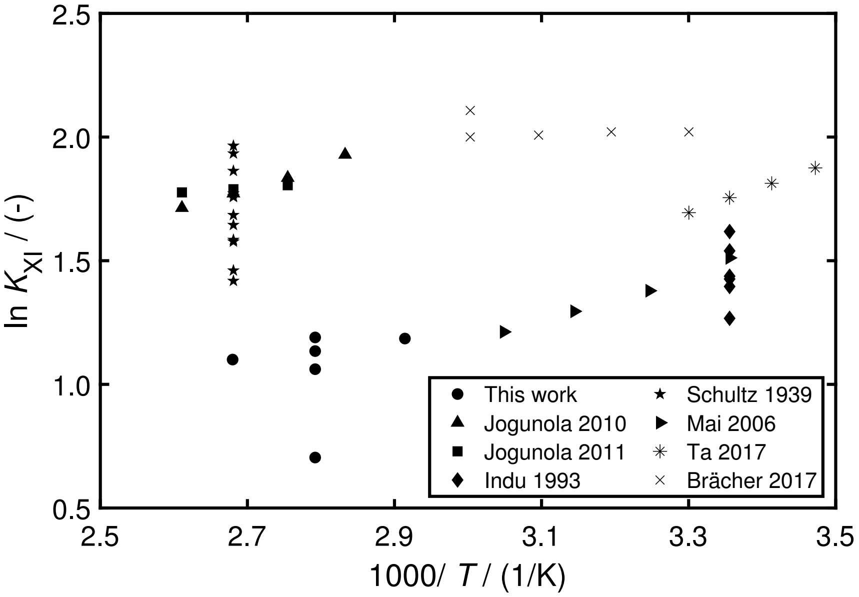

Figure 29: Comparison of resulting chemical equilibrium constant K_{XI} of the esterification of formic acid to methyl formate from this work (•) with literature [63, 64, 72–74, 98, 99].

A.3 Determination of K_{IXa} and K_{IXb}

The chemical equilibrium constant K_{IXa} for reaction (IXa) (formation of trioxane from OME_4) and K_{IXb} for reaction (IXb) (formation of trioxane from MG_3) are calculated by the Arrhenius type equation ($\ln K_i = A_i + \frac{B_i}{T/\mathrm{K}}$). The parameters are derived from literature [15, 54] as follows.

Chemical equilibrium constant K_{IXa} Oestreich et al. [15] use reactions (VIII) (with $n \geq 2$) and (IXc). The respective chemical equilibrium constants K_{VIII} and K_{IXc} are defined mole-fraction-based and reported. K_{IXa} is then determined by

$$K_{\mathrm{IXa}} = \frac{x_{\mathrm{TRI}} \cdot x_{\mathrm{OME}_1}}{x_{\mathrm{OME}_4}} = \frac{K_{\mathrm{IXc}}}{(K_{\mathrm{VIII}})^3} \tag{42}$$

The Arrhenius parameters A_{IXa} ($= A_{\mathrm{IXc}} - 3 \cdot A_{\mathrm{VIII}}$) and B_{IXa} ($= B_{\mathrm{IXc}} - 3 \cdot B_{\mathrm{VIII}}$) are calculated, accordingly.

Chemical equilibrium constant K_{IXb} The oligomerization of formaldehyde in water according to Hahnenstein et al. [54] is described along reactions (I) and (II). The respective chemical equilibrium constants K_{I} and $K_{\mathrm{II},n}$ are defined mole-fraction-based and reported. K_{IXb} is then determined by

$$K_{\mathrm{IXb}} = \frac{x_{\mathrm{TRI}} \cdot x_{\mathrm{WA}}}{x_{\mathrm{MG}_3}} = \frac{K_{\mathrm{IXc}}}{K_{\mathrm{I}} \cdot K_{\mathrm{II,2}} \cdot K_{\mathrm{II,3}}} \tag{43}$$

The Arrhenius parameters A_{IXb} ($= A_{\mathrm{IXc}} - (A_{\mathrm{I}} + A_{\mathrm{II,2}} + A_{\mathrm{II,3}})$) and B_{IXb} ($= B_{\mathrm{IXc}} - (B_{\mathrm{I}} + B_{\mathrm{II,2}} + B_{\mathrm{II,3}})$) are calculated, accordingly.

A.4 Experimental Data

The measured neutral overall mass fractions of the components are given in Tables 13–18 for experiments KIN-S1-KIN-S6. The experimental conditions, the measured catalyst activities and the average catalyst activity are listed in the tables' captions.

Table 13: Neutral overall mass fractions over time for kinetic experiment KIN-S1. $\hat{m}_{\mathrm{FA}}/\hat{m}_{\mathrm{ME}}$ = 0.88 g/g, $\hat{w}_{\mathrm{WA}}$ = −0.067 g/g, $m_{\mathrm{cat}}/m_{\mathrm{L,0}}$ = 0.024 g/g, T = 343.15 K, catalyst activity after experiment: $c_{\mathrm{cat,final}}^{\mathrm{H^+}}$ = 0.892 mmol $\mathrm{H^+}$/g, average catalyst activity used in the model: $\bar{c}_{\mathrm{cat}}^{\mathrm{H^+}}$ = 0.946 mmol $\mathrm{H^+}$/g

	overall mass fractions												
t	FA	WA	ME	OME1	OME2	OME3	OME4	OME5	OME6	TRI	MEFO	FOAC	m_{L}
h	g/g	g/g	g/g	g/g	g/g	g/g	g/g	g/g	g/g	g/g	10^{-1}g/g	10^{-1}g/g	g
0.0	0.3661	0.0141	0.2787	0.3410	0.0000	0.0000	0.0000	0.0000	0.0000	0.0000	0.0007	0.0006	370.3
7.8	0.1868	0.0516	0.1267	0.3232	0.1722	0.0825	0.0355	0.0146	0.0057	0.0010	0.0008	0.0006	356.7
23.3	0.1866	0.0518	0.1227	0.3286	0.1728	0.0811	0.0342	0.0140	0.0054	0.0027	0.0010	0.0007	342.7
47.6	0.1861	0.0533	0.1212	0.3250	0.1725	0.0821	0.0351	0.0144	0.0055	0.0046	0.0012	0.0008	329.1
72.5	0.1858	0.0526	0.1188	0.3286	0.1726	0.0816	0.0346	0.0139	0.0054	0.0058	0.0014	0.0010	315.3
97.1	0.1859	0.0533	0.1168	0.3279	0.1729	0.0818	0.0348	0.0141	0.0054	0.0068	0.0017	0.0011	301.9
121.6	0.1865	0.0531	0.1172	0.3271	0.1731	0.0812	0.0347	0.0139	0.0055	0.0074	0.0019	0.0013	287.9
142.2	0.1851	0.0520	0.1194	0.3276	0.1722	0.0814	0.0346	0.0143	0.0054	0.0077	0.0021	0.0014	274.3

Table 14: Overall mass fractions over time for kinetic experiment KIN-S2. $\hat{m}_{\mathrm{FA}}/\hat{m}_{\mathrm{ME}} = 0.92$ g/g, $\hat{w}_{\mathrm{WA}} = -0.064$ g/g, $m_{\mathrm{cat}}/m_{\mathrm{L},0} = 0.025$ g/g, $T = 358.15$ K, catalyst activity after experiment: $c^{\mathrm{H}^+}_{\mathrm{cat,final}} = 0.726$ mmol H^+/g, average catalyst activity used in the model: $\bar{c}^{\mathrm{H}^+}_{\mathrm{cat}} = 0.863$ mmol H^+/g

	overall mass fractions												
t h	FA g/g	WA g/g	ME g/g	OME1 g/g	OME2 g/g	OME3 g/g	OME4 g/g	OME5 g/g	OME6 g/g	TRI g/g	MEFO 10^{-1}g/g	FOAC 10^{-1}g/g	m_{L} g
0.0	0.3788	0.0146	0.2728	0.3329	0.0004	0.0002	0.0000	0.0000	0.0000	0.0000	0.0020	0.0013	353.8
9.2	0.1916	0.0527	0.1210	0.3226	0.1704	0.0808	0.0346	0.0141	0.0056	0.0061	0.0032	0.0021	340.3
23.7	0.1900	0.0534	0.1197	0.3231	0.1704	0.0806	0.0343	0.0137	0.0054	0.0089	0.0040	0.0026	326.9
48.0	0.1893	0.0544	0.1199	0.3239	0.1700	0.0799	0.0337	0.0134	0.0052	0.0094	0.0054	0.0035	314.0
72.4	0.1900	0.0546	0.1185	0.3225	0.1702	0.0805	0.0342	0.0136	0.0053	0.0096	0.0069	0.0045	300.8
95.9	0.1904	0.0534	0.1191	0.3211	0.1706	0.0809	0.0344	0.0138	0.0053	0.0096	0.0083	0.0056	287.6
130.8	0.1905	0.0543	0.1192	0.3204	0.1699	0.0806	0.0345	0.0138	0.0053	0.0096	0.0108	0.0071	274.0
143.9	0.1920	0.0549	0.1182	0.3201	0.1697	0.0804	0.0342	0.0136	0.0053	0.0096	0.0119	0.0076	260.4

Table 15: Overall mass fractions over time for kinetic experiment KIN-S3. $\hat{m}_{\mathrm{FA}}/\hat{m}_{\mathrm{ME}}$ = 0.86 g/g, $\hat{w}_{\mathrm{WA}}$ = 0.041 g/g, $m_{\mathrm{cat}}/m_{\mathrm{L},0}$ = 0.020 g/g, T = 358.15 K, catalyst activity after experiment: $c^{\mathrm{H}^+}_{\mathrm{cat,final}}$ = 0.850 mmol H$^+$/g, average catalyst activity used in the model: $\bar{c}^{\mathrm{H}^+}_{\mathrm{cat}}$ = 0.925 mmol H$^+$/g

	overall mass fractions												
t	FA	WA	ME	OME1	OME2	OME3	OME4	OME5	OME6	TRI	MEFO	FOAC	m_{L}
h	g/g	g/g	g/g	g/g	g/g	g/g	g/g	g/g	g/g	g/g	10^{-1}g/g	10^{-1}g/g	g
0.0	0.4416	0.0416	0.5143	0.0015	0.0007	0.0000	0.0000	0.0000	0.0000	0.0000	0.0017	0.0010	462.5
8.1	0.2251	0.1385	0.1706	0.2810	0.1183	0.0441	0.0148	0.0048	0.0015	0.0011	0.0015	0.0016	435.6
31.2	0.2247	0.1357	0.1718	0.2817	0.1182	0.0438	0.0146	0.0047	0.0014	0.0029	0.0021	0.0024	422.5
57.8	0.2234	0.1380	0.1718	0.2816	0.1175	0.0433	0.0144	0.0045	0.0013	0.0037	0.0029	0.0032	408.5
82.1	0.2228	0.1394	0.1724	0.2799	0.1173	0.0433	0.0144	0.0044	0.0013	0.0041	0.0035	0.0040	395.2
102.8	0.2240	0.1361	0.1727	0.2811	0.1176	0.0432	0.0144	0.0045	0.0013	0.0043	0.0042	0.0046	380.9
126.9	0.2277	0.1408	0.1763	0.2658	0.1191	0.0443	0.0147	0.0045	0.0013	0.0045	0.0045	0.0059	367.4

Table 16: Overall mass fractions over time for kinetic experiment KIN-S4. $\hat{m}_{\mathrm{FA}}/\hat{m}_{\mathrm{ME}}$ = 0.58 g/g, $\hat{w}_{\mathrm{WA}}$ = −0.072 g/g, $m_{\mathrm{cat}}/m_{\mathrm{L},0}$ = 0.025 g/g, T = 358.15 K, catalyst activity after experiment: $c^{\mathrm{H}^+}_{\mathrm{cat,final}}$ = 0.476 mmol H^+/g, average catalyst activity used in the model: $\bar{c}^{\mathrm{H}^+}_{\mathrm{cat}}$ = 0.738 mmol H^+/g

	overall mass fractions												
t	FA	WA	ME	OME1	OME2	OME3	OME4	OME5	OME6	TRI	MEFO	FOAC	m_{L}
h	g/g	g/g	g/g	g/g	g/g	g/g	g/g	g/g	g/g	g/g	10^{-1}g/g	10^{-1}g/g	g
0.0	0.2552	0.0103	0.3870	0.3472	0.0001	0.0000	0.0000	0.0000	0.0000	0.0000	0.0012	0.0007	347.7
2.0	0.1041	0.0749	0.1411	0.5393	0.1145	0.0215	0.0035	0.0006	0.0001	0.0002	0.0016	0.0011	335.9
7.9	0.1042	0.0749	0.1435	0.5360	0.1148	0.0216	0.0036	0.0007	0.0001	0.0003	0.0019	0.0013	325.5
24.1	0.1052	0.0756	0.1410	0.5364	0.1148	0.0217	0.0036	0.0007	0.0001	0.0005	0.0020	0.0013	312.8
32.5	0.1042	0.0752	0.1408	0.5388	0.1141	0.0217	0.0036	0.0007	0.0001	0.0005	0.0021	0.0014	301.3
53.1	0.1055	0.0758	0.1412	0.5360	0.1145	0.0216	0.0036	0.0007	0.0001	0.0007	0.0024	0.0015	289.2
115.0	0.1058	0.0756	0.1460	0.5300	0.1157	0.0215	0.0035	0.0006	0.0001	0.0007	0.0031	0.0022	277.9
128.1	0.1065	0.0756	0.1450	0.5295	0.1162	0.0217	0.0035	0.0006	0.0001	0.0007	0.0032	0.0024	265.8

Table 17: Overall mass fractions over time for kinetic experiment KIN-S5. $\hat{m}_{\mathrm{FA}}/\hat{m}_{\mathrm{ME}}$ = 0.94 g/g, $\hat{w}_{\mathrm{WA}}$ = −0.062 g/g, $m_{\mathrm{cat}}/m_{\mathrm{L},0}$ = 0.023 g/g, T = 373.15 K, catalyst activity after experiment: $c_{\mathrm{cat,final}}^{\mathrm{H}^+}$ = 0.370 mmol H$^+$/g, average catalyst activity used in the model: $\bar{c}_{\mathrm{cat}}^{\mathrm{H}^+}$ = 0.685 mmol H$^+$/g

	overall mass fractions												
t h	FA g/g	WA g/g	ME g/g	OME1 g/g	OME2 g/g	OME3 g/g	OME4 g/g	OME5 g/g	OME6 g/g	TRI g/g	MEFO 10^{-1}g/g	FOAC 10^{-1}g/g	m_{L} g
0.0	0.3786	0.0188	0.2613	0.3411	0.0000	0.0000	0.0000	0.0000	0.0000	0.0000	0.0003	0.0004	393.4
1.8	0.1957	0.0579	0.1192	0.3217	0.1678	0.0787	0.0333	0.0135	0.0052	0.0060	0.0059	0.0040	380.3
6.8	0.1945	0.0565	0.1201	0.3233	0.1672	0.0772	0.0323	0.0132	0.0048	0.0095	0.0073	0.0053	366.9
24.1	0.1931	0.0574	0.1197	0.3238	0.1670	0.0771	0.0322	0.0129	0.0048	0.0098	0.0118	0.0085	353.7
48.0	0.1939	0.0583	0.1173	0.3234	0.1677	0.0772	0.0319	0.0129	0.0047	0.0099	0.0170	0.0115	340.1
73.1	0.1927	0.0572	0.1172	0.3247	0.1671	0.0769	0.0318	0.0128	0.0049	0.0099	0.0290	0.0187	326.9
96.9	0.1908	0.0584	0.1163	0.3228	0.1673	0.0772	0.0319	0.0130	0.0048	0.0099	0.0458	0.0299	313.7
121.2	0.1890	0.0588	0.1149	0.3276	0.1664	0.0753	0.0307	0.0122	0.0046	0.0099	0.0674	0.0387	300.1
143.9	0.1872	0.0579	0.1146	0.3290	0.1657	0.0744	0.0302	0.0119	0.0044	0.0099	0.0926	0.0570	287.1

Table 18: Overall mass fractions over time for kinetic experiment KIN-S6. $\hat{m}_{\mathrm{FA}}/\hat{m}_{\mathrm{ME}} = 0.90$ g/g, $\hat{w}_{\mathrm{WA}} = -0.065$ g/g, $m_{\mathrm{cat}}/m_{\mathrm{L,0}} = 0.033$ g/g, $T = 358.15$ K, catalyst activity after experiment: $c^{\mathrm{H}^+}_{\mathrm{cat,final}} = 0.444$ mmol H^+/g, average catalyst activity used in the model: $\bar{c}^{\mathrm{H}^+}_{\mathrm{cat}} = 0.722$ mmol H^+/g

	overall mass fractions												
t	FA	WA	ME	OME1	OME2	OME3	OME4	OME5	OME6	TRI	MEFO	FOAC	m_{L}
h	g/g	g/g	g/g	g/g	g/g	g/g	g/g	g/g	g/g	g/g	10^{-1}g/g	10^{-1}g/g	g
0.0	0.3663	0.0180	0.2630	0.3518	0.0004	0.0002	0.0000	0.0000	0.0000	0.0000	0.0012	0.0011	400.4
4.4	0.1852	0.0564	0.1177	0.3425	0.1705	0.0764	0.0308	0.0122	0.0044	0.0035	0.0015	0.0011	387.2
34.6	0.1830	0.0561	0.1176	0.3439	0.1697	0.0753	0.0302	0.0117	0.0041	0.0078	0.0033	0.0022	374.9
55.3	0.1834	0.0574	0.1163	0.3427	0.1699	0.0754	0.0302	0.0119	0.0043	0.0079	0.0042	0.0027	361.2
76.5	0.1833	0.0574	0.1153	0.3430	0.1702	0.0755	0.0301	0.0119	0.0043	0.0080	0.0054	0.0038	348.3
97.6	0.1843	0.0559	0.1154	0.3419	0.1702	0.0759	0.0304	0.0121	0.0043	0.0079	0.0093	0.0069	335.5
119.7	0.1828	0.0578	0.1147	0.3422	0.1697	0.0755	0.0301	0.0119	0.0043	0.0080	0.0195	0.0117	322.9
141.7	0.1819	0.0568	0.1138	0.3436	0.1698	0.0751	0.0297	0.0117	0.0041	0.0080	0.0357	0.0197	309.8

A.5 Experimental Profiles

In Figures 30 and 31, the measured overall concentration profiles of methyl formate from the reaction experiments KIN-S1-KIN-S4 and KIN-S5-KIN-S6 are compared to the model calculations, respectively. Figure 32 shows the measured overall concentration profiles of formic acid for reaction experiments KIN-S1-KIN-S4 in comparison to the model calculations.

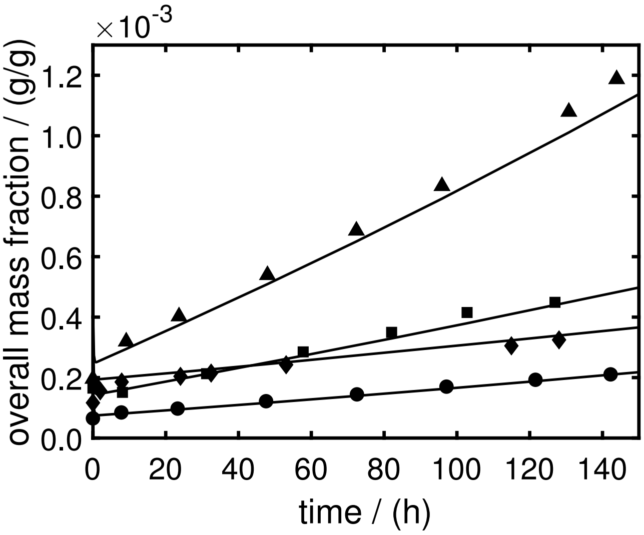

Figure 30: Measured overall concentration profiles of methyl formate under varied reaction conditions (symbol, T_R / K, ($\hat{m}_\mathrm{FA}/\hat{m}_\mathrm{ME}$) / (g/g), $\hat{w}_\mathrm{WA}$ / (g/g)): KIN-S1(•, 343.15, 0.88, −0.067), KIN-S2(▲, 358.15, 0.92, −0.064), KIN-S3(■, 358.15, 0.86, 0.041) and KIN-S4(⧫, 358.15, 0.58, −0.072). Kinetic model: solid lines(-).

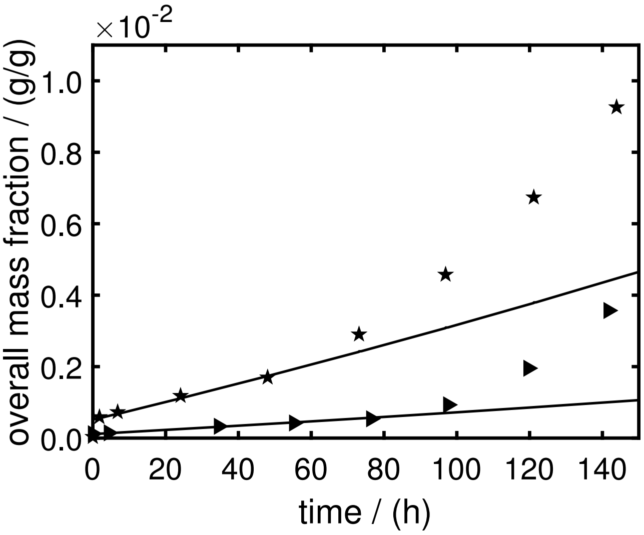

Figure 31: Measured overall concentration profiles of methyl formate under varied reaction conditions (symbol, T_R / K, $(\hat{m}_\mathrm{FA}/\hat{m}_\mathrm{ME})$ / (g/g), $\hat{w}_\mathrm{WA}$ / (g/g)): KIN-S5(★, 373.15, 0.94, −0.062), and KIN-S6(▸, 358.15, 0.90, −0.065). Kinetic model: solid lines(-).

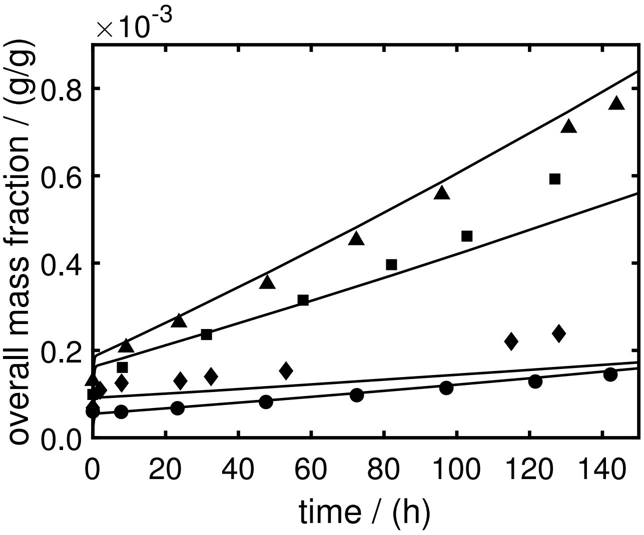

Figure 32: Measured overall concentration profiles of formic acid under varied reaction conditions (symbol, T_R / K, $(\hat{m}_\mathrm{FA}/\hat{m}_\mathrm{ME})$ / (g/g), $\hat{w}_\mathrm{WA}$ / (g/g)): KIN-S1(•, 343.15, 0.88, −0.067), KIN-S2(▲, 358.15, 0.92, −0.064), KIN-S3(■, 358.15, 0.86, 0.041) and KIN-S4(⧫, 358.15, 0.58, −0.072). Kinetic model: solid lines(-).

A.6 Trioxane Level in Recycle

Figure 33 shows the mass fraction of trioxane in the recycle (stream 9) plotted against the reactor temperature T_R. The plotted values were obtained from the process simulation with a constant purge stream $\dot{m}_\mathrm{purge}$ = 0.01 kg/h. The formation of trioxane was modeled according to reaction (IXb) (formation from MG_3).

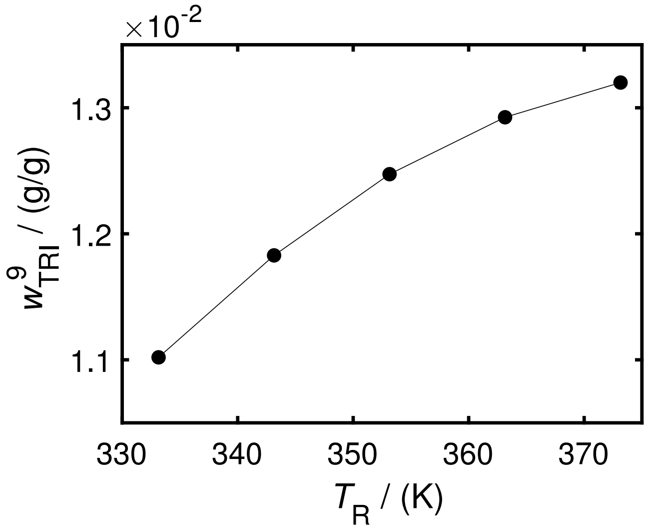

Figure 33: Mass fraction of trioxane in recycle stream 9 against reactor temperature obtained from process simulation at a constant purge stream of $\dot{m}_\mathrm{purge}$ = 0.01 kg/h (trioxane formation modeled from MG_3).

A.7 Stream Table of the OME Process with Purge

Table 19 shows the stream table obtained from the process simulation at a constant reactor temperature T_R = 343.15 K. The purge (stream 10) was adjusted to meet a side product level (methyl formate + formic acid) of 0.001 g/g in the recycle (stream 9). The labeling of the streams follows the process scheme in Figure 1.

Table 19: Stream table of the OME process for $T_\mathrm{R} = 343.15$ K and the side product level $\bar{w}^{9}_{\mathrm{side}} = 0.001$ g/g in stream 9.

stream	1	2	3	4	5	6	7	8	9	10	11
$\dot{m}$ / kg/h	1.276	8.024	8.024	6.876	1.148	1.000	0.148	0.248	6.628	0.027	6.601
neutral overall mass fractions / g/g											
FA	0.560	0.296	0.207	0.242	0.000	0.000	0.000	0.000	0.251	0.251	0.251
WA	0.100	0.021	0.036	0.042	0.000	0.000	0.000	1.000	0.007	0.007	0.007
ME	0.340	0.175	0.121	0.142	0.000	0.000	0.000	0.000	0.147	0.147	0.147
OME_1	0.000	0.285	0.287	0.334	0.000	0.000	0.000	0.000	0.347	0.347	0.347
OME_2	0.000	0.167	0.168	0.196	0.000	0.000	0.000	0.000	0.203	0.203	0.203
OME_3	0.000	0.026	0.088	0.031	0.430	0.493	0.000	0.000	0.032	0.032	0.032
OME_4	0.000	0.000	0.043	0.000	0.298	0.342	0.000	0.000	0.000	0.000	0.000
OME_5	0.000	0.000	0.020	0.000	0.143	0.164	0.000	0.000	0.000	0.000	0.000
$\mathrm{OME}_{n\geq 6}$	0.000	0.018	0.018	0.000	0.129	0.000	1.000	0.000	0.000	0.000	0.000
neutral overall mass fractions / $10^{-1}\cdot$ g/g											
TRI	0.000	0.100	0.100	0.117	0.000	0.000	0.000	0.000	0.122	0.122	0.122
MEFO	0.000	0.005	0.005	0.006	0.000	0.000	0.000	0.000	0.006	0.006	0.006
FOAC	0.000	0.003	0.003	0.004	0.000	0.000	0.000	0.000	0.004	0.004	0.004
acidic overall mass fractions / g/g											
FA	0.560	0.546	0.546	0.518	0.714	0.700	0.810	0.000	0.538	0.538	0.538
WA	0.100	−0.079	−0.079	−0.074	−0.112	−0.118	−0.074	1.000	−0.114	−0.114	−0.114
ME	0.340	0.533	0.533	0.556	0.398	0.418	0.265	0.000	0.577	0.577	0.577
FA/ME	1.647	1.024	1.024	0.932	1.793	1.674	3.061	–	0.932	0.932	0.932

B Scale-up of a Tubular Reactor for the Production of OME

B.1 Catalyst Swelling Properties

The swelling behavior of the ion-exchange resin Amberlyst 46 was investigated experimentally. A weighed mass of Amberlyst 46 was stored for 24 h in various solutions. Values did not change even after storage for five more days. Besides the pure solvents water, methanol, and methylal (OME_1), the mixture Mix 1 (0.19 g/g FA, 0.12 g/g ME, 0.05 g/g WA, 0.33 g/g OME_1, 0.17 g/g OME_2, 0.14 g/g OME_{3+}) was examined. The volume of the catalyst was then measured with a measuring cylinder. The resulting catalyst density ρ_{cat} and the specific volume ν_{cat} are given in Table 20.

Table 20: Measured specific catalyst volume in different solvents.

Solvent	m_{cat} / g	V_{cat} / mL	ρ_{cat} / g/L	ν_{cat} / mL/g
Water	3.97	10.0	397	2.52
Methanol	4.02	11.0	366	2.73
Methylal	3.77	11.5	327	3.06
Mix 1	4.03	12.5	323	3.09

B.2 Details on the Feed Preparation

The feed for the reaction experiments was prepared by combining different ratios of methanolic formaldehyde solution ($\tilde{w}_{\mathrm{FA}}/\tilde{w}_{\mathrm{ME}}/\tilde{w}_{\mathrm{WA}} \approx 0.55/0.40/0.05$ g/g) and OME. In most experiments, OME_1 was added. In two experiments, KIN-T7 and KIN-T8, also higher OME were added. The higher OME were formed in a prereaction. OME_1 and trioxane were mixed in a vessel and dry catalyst Amberlyst 46 was added. The mixture was stirred at ambient temperature until chemical equilibrium was reached. The catalyst was removed and the liquid mixture was used for feed preparation. The chemical equilibrium of the reaction OME + trioxane is far on the product side. The remaining trioxane mass fraction in the feed mixtures KIN-T7 and KIN-T8 was therefore < 0.0005 g/g.

B.3 Experimental Data

The measured overall mass fractions of the components for the experiments KIN-T1-KIN-T8 and KINB-1 are given in Tables 21-29. The pseudo residence time τ is used to specify the position in the reactor. The operating conditions of each reaction experiment are listed in the tables' captions.

Table 21: Overall mass fractions throughout the tubular reactor for kinetic experiment KIN-T1. T_R = 311 K, $\dot{m}$ = 1.6 kg/h.

	overall mass fractions								
τ min	FA g/g	ME g/g	WA g/g	OME1 g/g	OME2 g/g	OME3 g/g	OME4 g/g	OME5 g/g	OME6 g/g
0.000	0.2260	0.1731	0.0214	0.5795	0.0000	0.0000	0.0000	0.0000	0.0000
1.981	0.1772	0.1255	0.0342	0.5826	0.0554	0.0177	0.0054	0.0015	0.0004
3.962	0.1512	0.1104	0.0396	0.5575	0.0973	0.0312	0.0094	0.0026	0.0007
5.942	0.1371	0.1059	0.0404	0.5409	0.1207	0.0391	0.0118	0.0032	0.0009
7.923	0.1302	0.1034	0.0405	0.5288	0.1359	0.0435	0.0131	0.0035	0.0010
9.904	0.1258	0.1023	0.0406	0.5183	0.1463	0.0474	0.0143	0.0039	0.0011
11.885	0.1221	0.1013	0.0410	0.5129	0.1531	0.0496	0.0149	0.0040	0.0011

Table 22: Overall mass fractions throughout the tubular reactor for kinetic experiment KIN-T2. T_R = 311 K, $\dot{m}$ = 2.1 kg/h.

	overall mass fractions								
τ min	FA g/g	ME g/g	WA g/g	OME1 g/g	OME2 g/g	OME3 g/g	OME4 g/g	OME5 g/g	OME6 g/g
0.000	0.2191	0.1703	0.0210	0.5893	0.0002	0.0000	0.0000	0.0000	0.0000
1.500	0.1776	0.1235	0.0312	0.6037	0.0445	0.0139	0.0041	0.0012	0.0003
3.000	0.1511	0.1080	0.0371	0.5803	0.0856	0.0270	0.0080	0.0022	0.0006
4.500	0.1394	0.1029	0.0402	0.5606	0.1084	0.0346	0.0103	0.0028	0.0008
6.000	0.1298	0.1012	0.0401	0.5468	0.1255	0.0402	0.0120	0.0033	0.0009
7.500	0.1250	0.1002	0.0409	0.5355	0.1369	0.0440	0.0131	0.0035	0.0010
9.000	0.1212	0.0992	0.0407	0.5310	0.1442	0.0454	0.0136	0.0036	0.0010

Table 23: Overall mass fractions throughout the tubular reactor for kinetic experiment KIN-T3. T_R = 325 K, $\dot{m}$ = 4.2 kg/h.

overall mass fractions									
τ	FA	ME	WA	OME1	OME2	OME3	OME4	OME5	OME6
min	g/g	g/g	g/g	g/g	g/g	g/g	g/g	g/g	g/g
0.000	0.2141	0.1635	0.0200	0.6024	0.0000	0.0000	0.0000	0.0000	0.0000
0.743	0.1629	0.1203	0.0322	0.5990	0.0591	0.0188	0.0056	0.0016	0.0005
1.486	0.1327	0.1067	0.0360	0.5686	0.1083	0.0341	0.0101	0.0027	0.0008
2.228	0.1200	0.1026	0.0373	0.5487	0.1334	0.0416	0.0122	0.0032	0.0009
2.971	0.1107	0.1022	0.0384	0.5366	0.1484	0.0458	0.0133	0.0035	0.0009
3.714	0.1072	0.1007	0.0383	0.5288	0.1574	0.0486	0.0141	0.0037	0.0010
4.457	0.1058	0.1010	0.0390	0.5216	0.1629	0.0502	0.0145	0.0038	0.0010

Table 24: Overall mass fractions throughout the tubular reactor for kinetic experiment KIN-T4. T_R = 324 K, $\dot{m}$ = 5.0 kg/h.

overall mass fractions									
τ	FA	ME	WA	OME1	OME2	OME3	OME4	OME5	OME6
min	g/g	g/g	g/g	g/g	g/g	g/g	g/g	g/g	g/g
0.000	0.2141	0.1635	0.0200	0.6024	0.0000	0.0000	0.0000	0.0000	0.0000
0.623	0.1722	0.1243	0.0306	0.6040	0.0472	0.0152	0.0047	0.0013	0.0004
1.246	0.1375	0.1051	0.0357	0.5822	0.0974	0.0301	0.0088	0.0024	0.0007
1.869	0.1227	0.1038	0.0377	0.5559	0.1254	0.0391	0.0115	0.0031	0.0008
2.492	0.1145	0.1016	0.0382	0.5437	0.1410	0.0439	0.0128	0.0034	0.0009
3.115	0.1077	0.1006	0.0377	0.5404	0.1509	0.0455	0.0130	0.0034	0.0009
3.738	0.1078	0.1002	0.0389	0.5305	0.1567	0.0476	0.0137	0.0036	0.0010

Table 25: Overall mass fractions throughout the tubular reactor for kinetic experiment KIN-T5. T_R = 341 K, $\dot{m}$ = 9.3 kg/h.

overall mass fractions									
τ	FA	ME	WA	OME1	OME2	OME3	OME4	OME5	OME6
min	g/g	g/g	g/g	g/g	g/g	g/g	g/g	g/g	g/g
0.000	0.2092	0.1627	0.0195	0.6086	0.0000	0.0000	0.0000	0.0000	0.0000
0.331	0.1650	0.1244	0.0329	0.5780	0.0679	0.0223	0.0069	0.0020	0.0006
0.662	0.1226	0.1099	0.0375	0.5305	0.1377	0.0440	0.0131	0.0036	0.0010
0.993	0.1120	0.1081	0.0383	0.5130	0.1591	0.0497	0.0147	0.0039	0.0011
1.323	0.1087	0.1082	0.0390	0.5072	0.1658	0.0509	0.0150	0.0040	0.0011
1.654	0.1079	0.1079	0.0390	0.5052	0.1683	0.0516	0.0150	0.0039	0.0011
1.985	0.1093	0.1089	0.0387	0.5014	0.1692	0.0521	0.0152	0.0040	0.0011

Table 26: Overall mass fractions throughout the tubular reactor for kinetic experiment KIN-T6. T_R = 337 K, $\dot{m}$ = 11.5 kg/h.

	overall mass fractions								
τ min	FA g/g	ME g/g	WA g/g	OME1 g/g	OME2 g/g	OME3 g/g	OME4 g/g	OME5 g/g	OME6 g/g
0.000	0.2092	0.1627	0.0195	0.6086	0.0000	0.0000	0.0000	0.0000	0.0000
0.268	0.1747	0.1306	0.0281	0.6082	0.0396	0.0131	0.0041	0.0012	0.0004
0.536	0.1300	0.1088	0.0351	0.5703	0.1078	0.0341	0.0103	0.0028	0.0008
0.805	0.1140	0.1061	0.0367	0.5430	0.1396	0.0434	0.0128	0.0034	0.0010
1.073	0.1055	0.1059	0.0367	0.5305	0.1553	0.0476	0.0139	0.0036	0.0010
1.341	0.1036	0.1049	0.0372	0.5235	0.1624	0.0493	0.0143	0.0037	0.0010
1.609	0.1023	0.1041	0.0372	0.5241	0.1650	0.0489	0.0139	0.0035	0.0010

Table 27: Overall mass fractions throughout the tubular reactor for kinetic experiment KIN-T7. T_R = 327 K, $\dot{m}$ = 2.6 kg/h.

	overall mass fractions								
τ min	FA g/g	ME g/g	WA g/g	OME1 g/g	OME2 g/g	OME3 g/g	OME4 g/g	OME5 g/g	OME6 g/g
0.000	0.2162	0.1548	0.0199	0.4634	0.1129	0.0255	0.0054	0.0010	0.0002
1.170	0.1690	0.1123	0.0318	0.4663	0.1531	0.0475	0.0142	0.0040	0.0012
2.341	0.1366	0.1036	0.0351	0.4457	0.1800	0.0665	0.0228	0.0069	0.0022
3.511	0.1297	0.1026	0.0345	0.4406	0.1852	0.0710	0.0253	0.0079	0.0025
4.682	0.1272	0.1021	0.0353	0.4395	0.1860	0.0721	0.0262	0.0083	0.0027
5.852	0.1278	0.1022	0.0356	0.4380	0.1859	0.0722	0.0265	0.0085	0.0028
7.023	0.1287	0.1019	0.0349	0.4377	0.1855	0.0723	0.0268	0.0086	0.0029

Table 28: Overall mass fractions throughout the tubular reactor for kinetic experiment KIN-T8. T_R = 327 K, $\dot{m}$ = 5.2 kg/h.

	overall mass fractions								
τ min	FA g/g	ME g/g	WA g/g	OME1 g/g	OME2 g/g	OME3 g/g	OME4 g/g	OME5 g/g	OME6 g/g
0.000	0.2152	0.1550	0.0202	0.4644	0.1130	0.0254	0.0053	0.0010	0.0002
0.591	0.1844	0.1252	0.0277	0.4755	0.1367	0.0371	0.0098	0.0025	0.0007
1.182	0.1483	0.1067	0.0340	0.4585	0.1688	0.0575	0.0185	0.0055	0.0017
1.772	0.1375	0.1041	0.0352	0.4477	0.1787	0.0653	0.0222	0.0067	0.0021
2.363	0.1324	0.1032	0.0345	0.4429	0.1835	0.0692	0.0242	0.0074	0.0023
2.954	0.1310	0.1023	0.0357	0.4398	0.1848	0.0707	0.0251	0.0078	0.0025
3.545	0.1282	0.1024	0.0358	0.4393	0.1857	0.0717	0.0258	0.0081	0.0026

Table 29: Overall mass fractions over time for kinetic experiment KINB-1. T_R = 333 K, $m_\mathrm{cat}/m_\mathrm{L,0}$=0.016 g/g.

	overall mass fractions									
t	FA	ME	WA	OME1	OME2	OME3	OME4	OME5	OME6	m_L
min	g/g	g/g	g/g	g/g	g/g	g/g	g/g	g/g	g/g	g
0.0	0.2076	0.1460	0.0194	0.6264	0.0004	0.0000	0.0000	0.0000	0.0000	435.64
1.7	0.1986	0.1372	0.0217	0.6242	0.0122	0.0041	0.0013	0.0004	0.0001	427.12
3.7	0.1878	0.1293	0.0232	0.6238	0.0242	0.0080	0.0026	0.0008	0.0002	419.26
5.3	0.1808	0.1247	0.0247	0.6213	0.0327	0.0109	0.0035	0.0010	0.0003	410.66
9.8	0.1673	0.1164	0.0273	0.6131	0.0512	0.0171	0.0054	0.0016	0.0005	401.09
20.0	0.1488	0.1063	0.0305	0.5946	0.0807	0.0271	0.0086	0.0025	0.0008	390.27
40.1	0.1256	0.1001	0.0319	0.5721	0.1152	0.0385	0.0121	0.0034	0.0010	380.92
81.7	0.1079	0.0967	0.0334	0.5453	0.1483	0.0483	0.0148	0.0041	0.0012	371.42
164.0	0.1005	0.0951	0.0342	0.5295	0.1674	0.0522	0.0156	0.0042	0.0012	361.04

B.4 Experimental Profiles

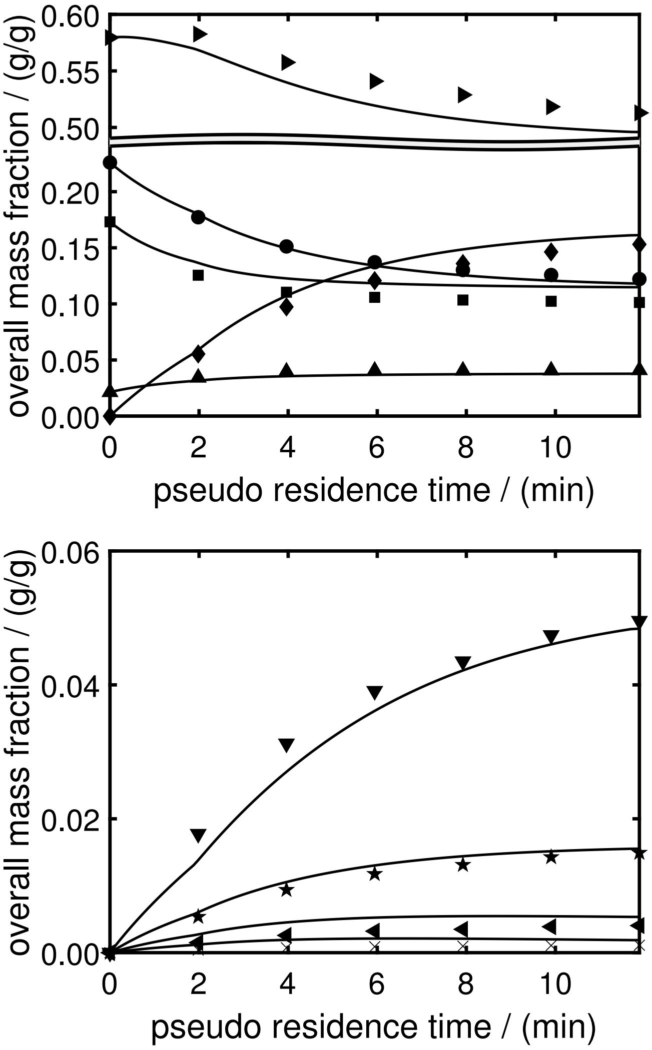

Figure 34: Measured overall concentration profiles of reaction experiment KIN-T1 (formaldehyde (•), methanol (■), water (▲), OME_1 (▸), OME_2 (⧫), OME_3 (▾), OME_4 (★), OME_5 (◂), OME_6 (×), Kinetic model (–)).

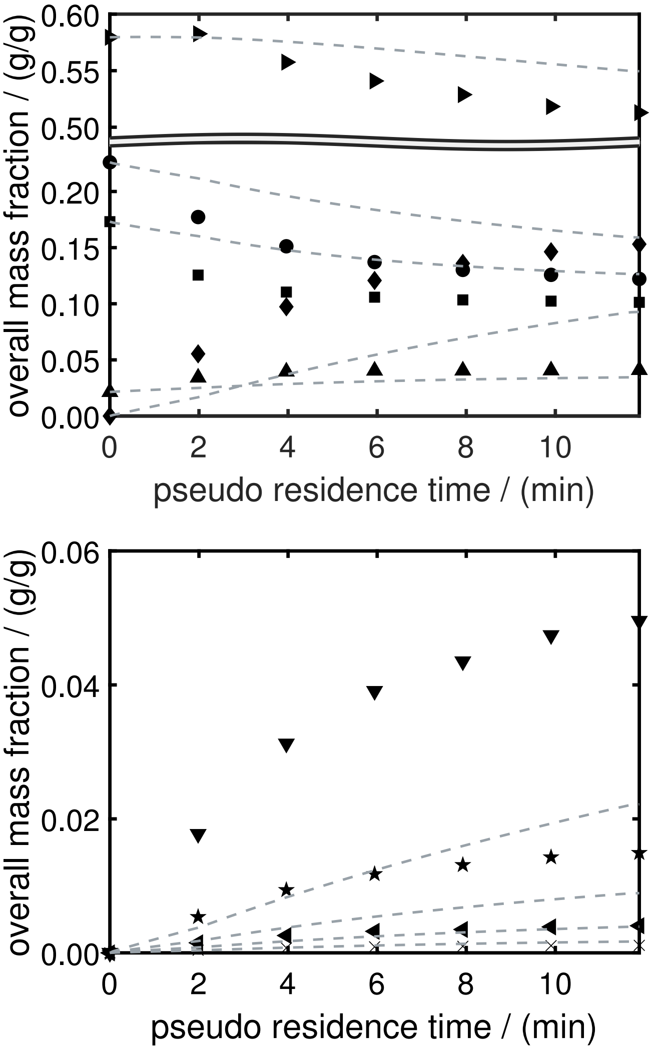

Figure 35: Measured overall concentration profiles of reaction experiment KIN-T1 (formaldehyde (•), methanol (■), water (▲), OME_1 (▸), OME_2 (⧫), OME_3 (▾), OME_4 (★), OME_5 (◂), OME_6 (×), Original kinetic model[31] (– –).

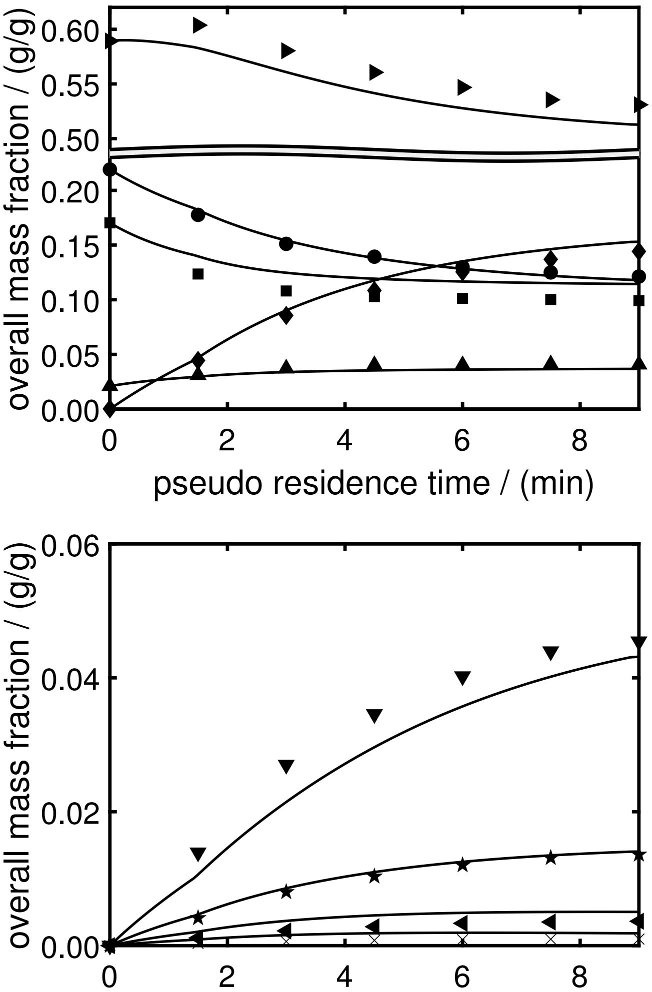

Figure 36: Measured overall concentration profiles of reaction experiment KIN-T2 (formaldehyde (•), methanol (■), water (▲), OME_1 (▸), OME_2 (⧫), OME_3 (▾), OME_4 (⋆), OME_5 (◂), OME_6 (×), Kinetic model (–)).

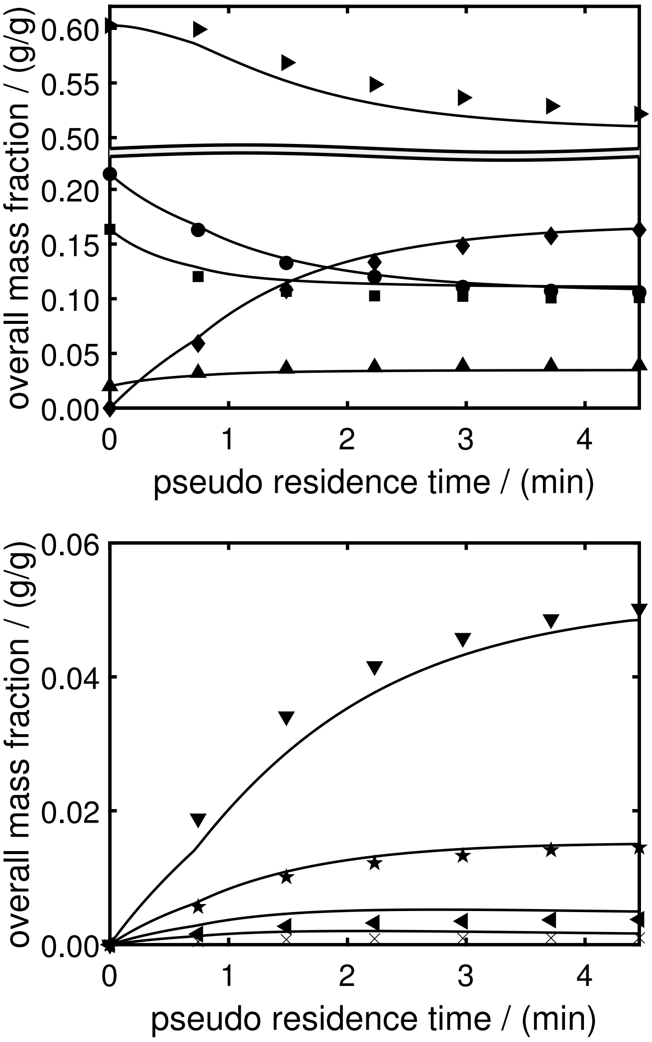

Figure 37: Measured overall concentration profiles of reaction experiment KIN-T3 (formaldehyde (•), methanol (■), water (▲), OME_1 (▸), OME_2 (⧫), OME_3 (▾), OME_4 (⋆), OME_5 (◂), OME_6 (×), Kinetic model (–)).

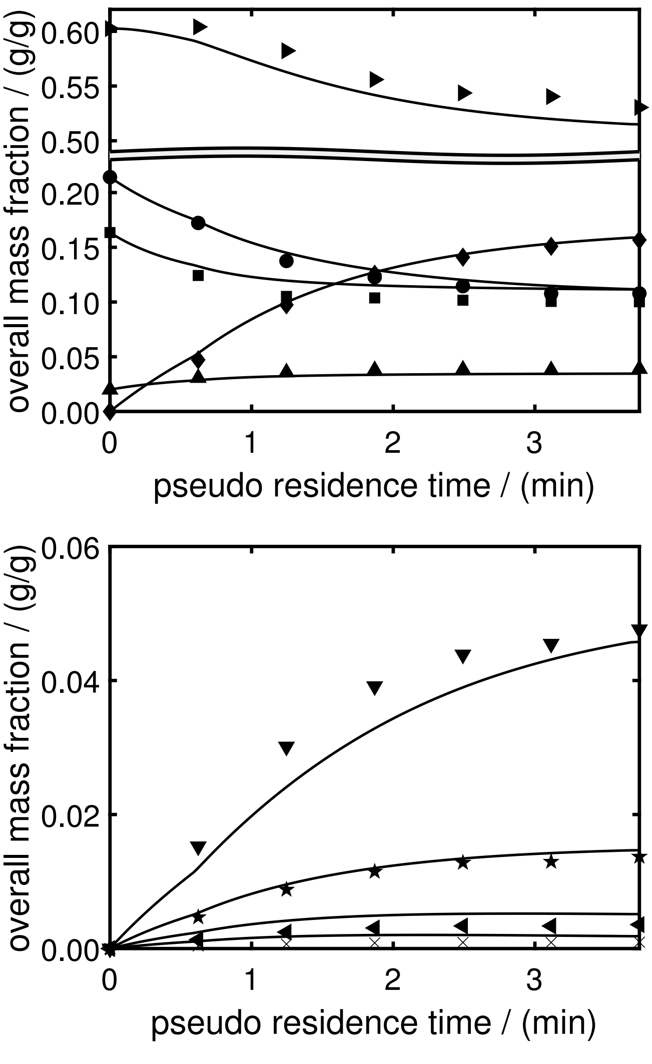

Figure 38: Measured overall concentration profiles of reaction experiment KIN-T4 (formaldehyde (•), methanol (■), water (▲), OME_1 (▸), OME_2 (⧫), OME_3 (▾), OME_4 (★), OME_5 (◂), OME_6 (×), Kinetic model (–)).

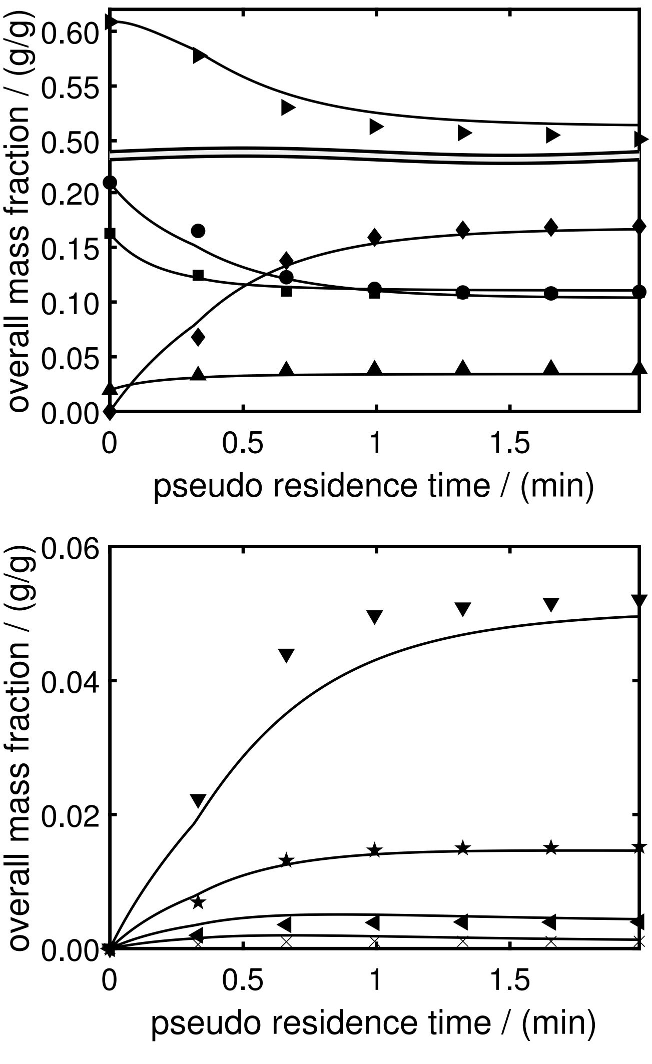

Figure 39: Measured overall concentration profiles of reaction experiment KIN-T5 (formaldehyde (•), methanol (■), water (▴), OME$_1$ (▸), OME$_2$ (⧫), OME$_3$ (▾), OME$_4$ (⋆), OME$_5$ (◂), OME$_6$ (×), Kinetic model (–)).

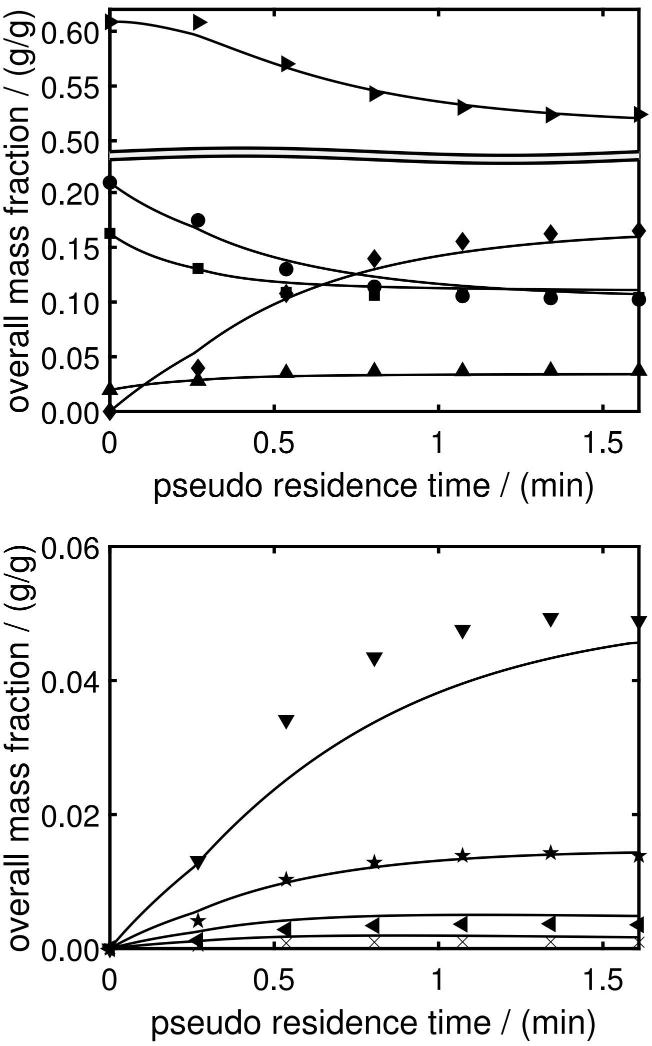

Figure 40: Measured overall concentration profiles of reaction experiment KIN-T6 (formaldehyde (•), methanol (■), water (▲), OME$_1$ (▸), OME$_2$ (⧫), OME$_3$ (▾), OME$_4$ (⋆), OME$_5$ (◂), OME$_6$ (×), Kinetic model (–)).

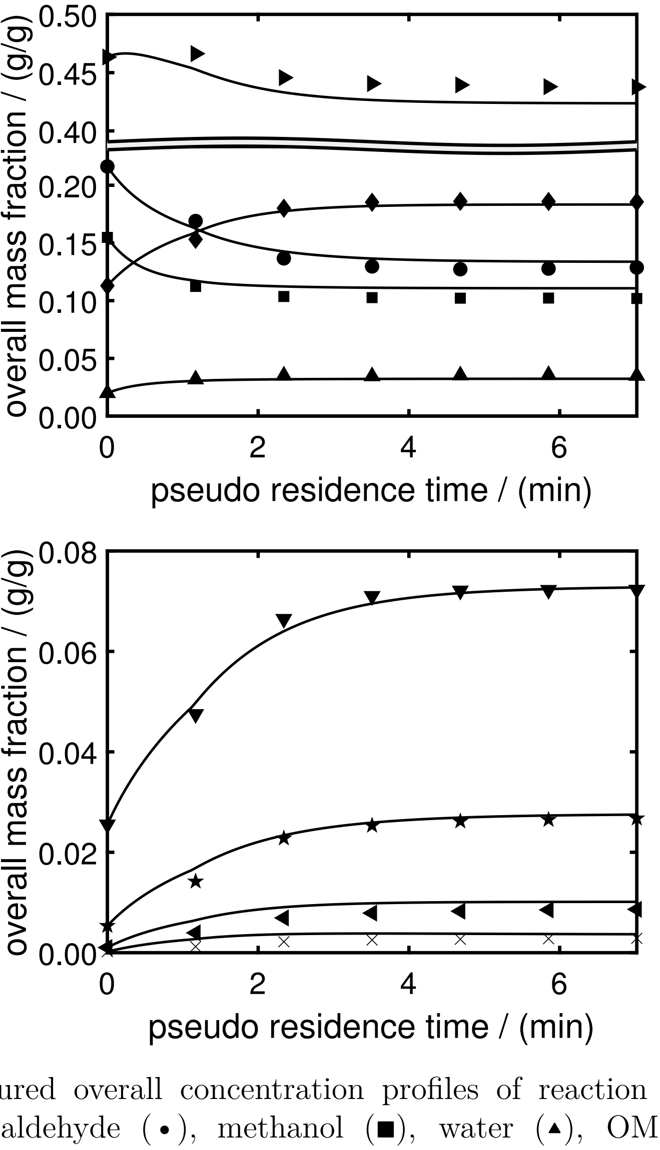

Figure 41: Measured overall concentration profiles of reaction experiment KIN-T7 (formaldehyde (•), methanol (■), water (▴), OME$_1$ (▸), OME$_2$ (⧫), OME$_3$ (▾), OME$_4$ (⋆), OME$_5$ (◂), OME$_6$ (×), Kinetic model (–)).

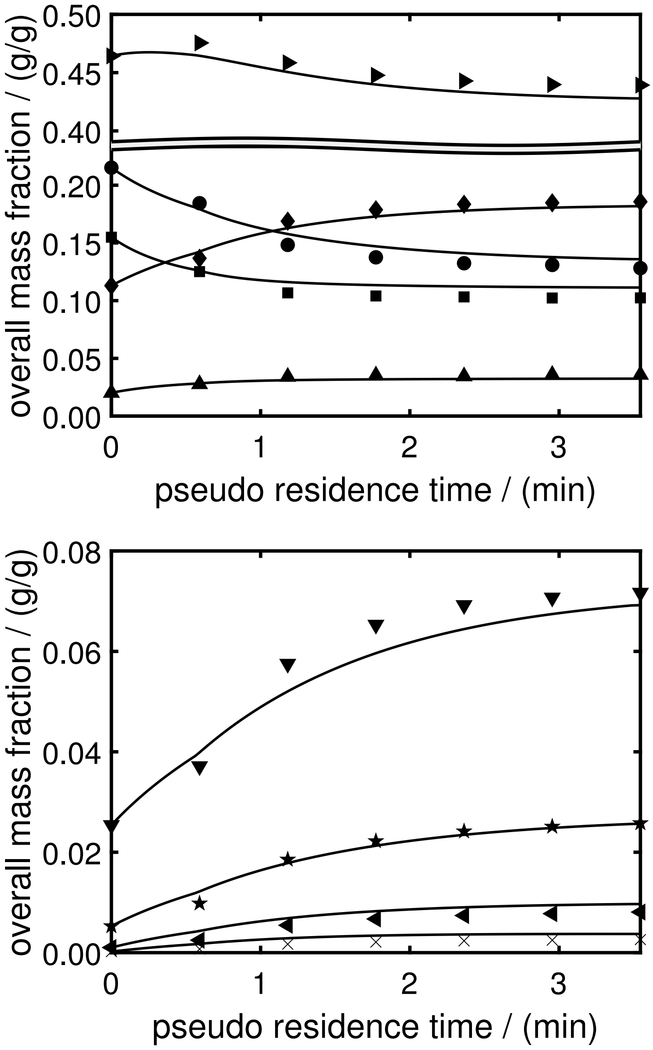

Figure 42: Measured overall concentration profiles of reaction experiment KIN-T8 (formaldehyde (•), methanol (■), water (▴), OME$_1$ (▸), OME$_2$ (⧫), OME$_3$ (▾), OME$_4$ (⋆), OME$_5$ (◂), OME$_6$ (×), Kinetic model (–)).

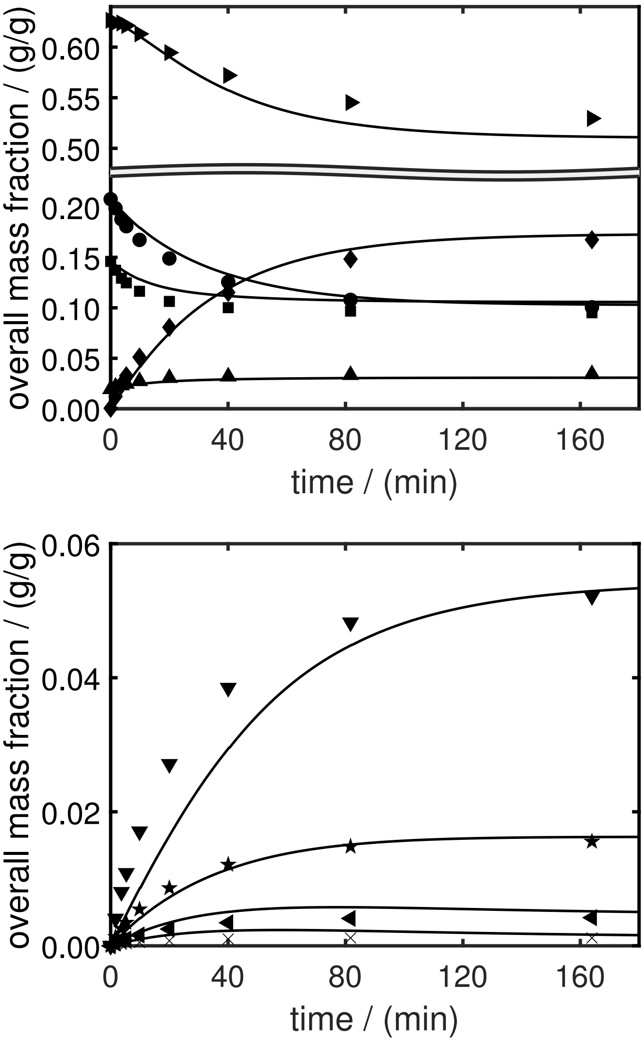

Figure 43: Measured overall concentration profiles of reaction experiment KINB-1 (formaldehyde (•), methanol (■), water (▲), OME_1 (▸), OME_2 (♦), OME_3 (▾), OME_4 (★), OME_5 (◂), OME_6 (×), Kinetic model (–)).

B.5 Catalyst Activity in the Tubular Reactor

In experiments prior to the present work, we have observed that the catalyst was partly contaminated with sodium ions and therefore partly deactivated. The measured catalyst activities throughout the reactor are shown in Figure 44. In addition, the applied catalyst activity in the reactor model is visualized as solid line.

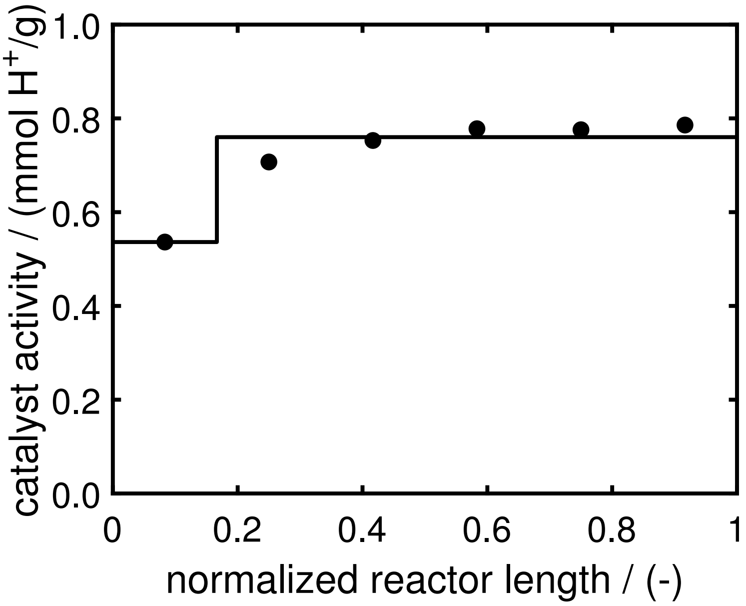

Figure 44: Measured catalyst activity profile over the reactor (Measured values (•), catalyst activity in the model (–)).

B.6 Reaction Kinetic Constants - Comparison between Experiments

The reaction kinetic constants $k_\mathrm{A}(T)$ and $k_\mathrm{G}(T)$ were fitted to the results from each single reaction experiment KIN-T1-KIN-T6. The resulting values were used to determine the parameters a_j and b_j of the correlation $\ln k_j = a_j + b_j/(T/K)$. Figure 45 depicts the ratio of $k_j^{\mathrm{single\,exp.}}$, determined from the single experiments, to k_j^{model} that was determined with the latter correlation and the parameters a_j and b_j given in the main part. The reaction experiments KIN-T1-KIN-T6 were performed in ascending order, so first KIN-T1 and last KIN-T6. No clear trend is observed in Figure 45. This indicates that the catalyst in the reactor did not substantially deactivate during these experiments.

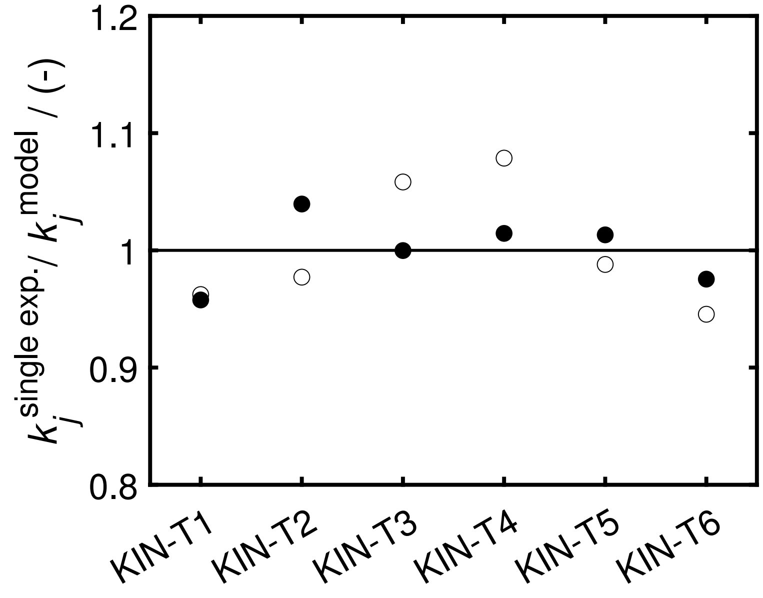

Figure 45: Comparison of $k_j^{\mathrm{single\,exp.}}$ determined from the single experiments to k_j^{model} that was determined with the correlation $\ln k_j = a_j + b_j/(T/K)$ for reaction experiments KIN-T1–KIN-T6 ($k_\mathrm{A}(T)(\bullet)$, $k_\mathrm{G}(T)(\circ)$).

B.7 Long-term Catalyst Deactivation

The ion-exchange resin Amberlyst 46 was stored in a methanolic formaldehyde solution (0.55 g/g FA, 0.40 g/g ME, 0.05 g/g WA). The measured catalyst activity results are depicted in Figure 46.

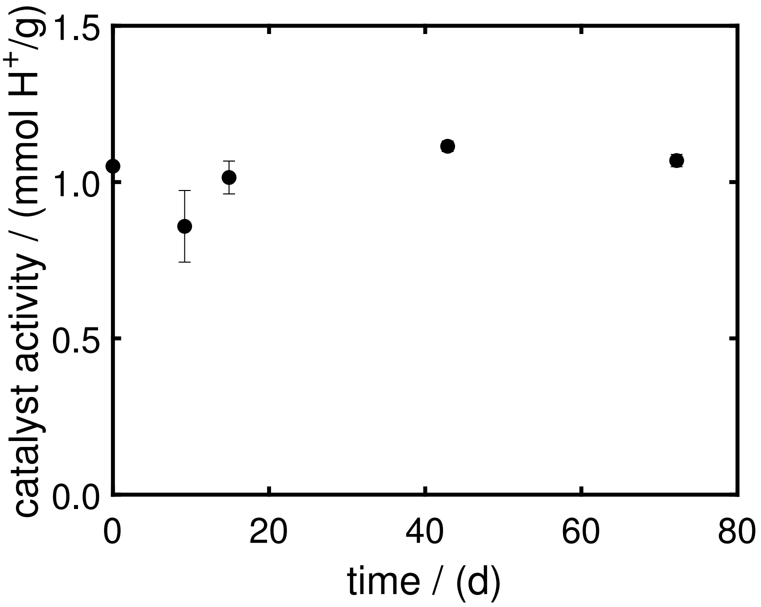

Figure 46: Measured catalyst activity over time during storage in methanolic formaldehyde solution. Errorbars indicate the standard deviation of the measured values.

B.8 Parameter Estimation for Scale-up

To evaluate the Ergun equation for the OME reactor (see main part), values for the liquid density ρ and the liquid dynamic viscosity η are needed. These values are not easily obtained experimentally as they are needed at the reactor temperature T_R = 343 K. Therefore, we used the avalaible pure component data listed in Table 30.

Table 30: Physical property data for the parameter estimation for the scale-up. The parameter values that are taken from literature are followed by the respective reference.

	ρ / kg/m^3				η / mPa s			
	20 °C		70°C		25°C		70°C	
ME	792.3	[100]	743.3	[100]	0.53	[101]	0.32	[101]
WA	1002.1	[100]	969.1	[100]	0.89	[102]	0.41	[102]
OME_1	859.3	[43]	–		0.31	[43]	–	
OME_2	977.5	[43]	–		0.64	[43]	–	
OME_3	1030.5	[43]	–		1.11	[43]	–	
OME_4	1073.7	[43]	–		1.85	[43]	–	
Estimate	–		1000.0		–		0.40	

The feed stream of the reactor consists of many different components (OME, methanol, water and additionally formaldehyde, methylenglycols, and hemiformals). Parameter values for OME were not available for T_R = 343 K. In addition, the dissolved formaldehyde most likely increases the values of both parameters [103, 104], ρ and η, but the quantitative effect is hard to determine reliably, especially in mixtures with OME. Therefore, we estimated the parameter values based on the available data. The estimated values are given in Table 30.

B.9 Calculation of the Adiabatic Temperature Change

To evaluate and visualize the total amount of heat that needs to be removed from the tubular reactor in the process, the adiabatic temperature rise is calculated for an example case. A mixture of formaldehyde and methanol (0.6 g/g FA, 0.4 g/g ME) reacts at $T = 298$ K to OME until chemical equilibrium is reached. The starting and final mass fractions are listed in Table 31. The adiabatic temperature rise ΔT_{ad} is then calculated to

$$\Delta T_{\text{ad}} = \frac{\sum_{i=1}^{N_C} M_i \cdot \Delta h^0_{f,i} \cdot (\tilde{w}_{i,\text{out}} - \tilde{w}_{i,\text{in}})}{\sum_{i=1}^{N_C} c^l_{p,i} \cdot M_i \cdot \tilde{w}_{i,\text{out}}} = +12.39\text{K} \tag{44}$$

with N_C as the number of components, M_i as the molar mass of component i, $\Delta h^0_{f,i}$ as the standard heat of formation, $\tilde{w}_i$ as the overall mass fraction of component i, and $c^l_{p,i}$ as the molar liquid heat capacity of component i. Standard heats of formation and molar liquid heat capacities are taken from [76] and [105] and are listed in Table 31.

Table 31: Physical property data for the calculation of the adiabatic temperature change. The parameter values that are taken from literature are followed by the respective reference.

	$\tilde{w}_{i,\text{in}}$ g/g	$\tilde{w}_{i,\text{out}}$ g/g	M_i g/mol	$\Delta h^0_{f,i}$ kJ/mol		$c^l_{p,i}$ J/(mol K)	
FA	0.600	0.348	30.03	−129.5	[105]	91.46	[105]
ME	0.400	0.154	32.04	−239.1	[76]	81.08	[76]
WA	0.000	0.075	18.02	−286.0	[76]	75.29	[76]
OME1	0.000	0.161	76.09	−379.8	[105]	158.67	[105]
OME2	0.000	0.111	106.12	−553.5	[105]	182.04	[105]
OME3	0.000	0.070	136.15	−727.2	[105]	201.57	[105]
OME4	0.000	0.042	166.17	−900.9	[105]	245.15	[105]
OME5	0.000	0.025	196.20	−1074.7	[105]	276.92	[105]
OME6	0.000	0.014	226.22	−1248.4	[105]	309.60	[105]

C Chemical Equilibrium of Transacetalization and Oligomerization Reactions

C.1 Model Equations and Implementation

In addition to the equations describing the chemical equilbrium of all reactions, which are given in the main part, mole balance equations are needed to solve the system of equations. The general mole balance of each component i in a batch reactor

$$n_i^{\mathrm{EQ}} - n_i^0 = \Delta n_i = \sum_{j=1}^{N_R} \nu_{ij} \cdot \xi_j \tag{45}$$

describes the mole change from initial to equilibrium state $n_i^{\mathrm{EQ}} - n_i^0$. This difference originates from chemical reactions and is determined from the sum over all reactions N_{R}, the stoichiometric coefficients ν_{ij} and the molar extent ξ_j of reaction j. The mole fraction of component i is then calculated from

$$x_i = \frac{n_i}{\sum_{i=1}^{N_C} n_i} \tag{46}$$

The resulting system of nonlinear equations needs to be solved numerically. In order to reduce the number of variables and equations, and consequently reduce the computational effort, mole balance equations were condensed.

The mathematical transformation of model equations is shown along an example system containing FA, TRI and the ethers Me,Me-OAE$_n$, Me,Et-OAE$_n$, and Et,Et-OAE$_n$ with chain lengths $n = 1-8$. Including additional ethers follows the described procedure, but complicates the clear presentation.

The example system includes the following reactions:

$$\mathrm{Me,Me-OAE}_{n-1} + \mathrm{FA} \xrightleftharpoons{\mathrm{H}^+} \mathrm{Me,Me-OAE}_n \qquad n = 2-8 \tag{ia}$$

$$\mathrm{Me,Et-OAE}_{n-1} + \mathrm{FA} \xrightleftharpoons{\mathrm{H}^+} \mathrm{Me,Et-OAE}_n \qquad n = 2-8 \tag{ib}$$

$$\mathrm{Et,Et-OAE}_{n-1} + \mathrm{FA} \xrightleftharpoons{\mathrm{H}^+} \mathrm{Et,Et-OAE}_n \qquad n = 2-8 \tag{ic}$$

$$\mathrm{TRI} \xrightleftharpoons{\mathrm{H}^+} 3\,\mathrm{FA} \tag{ii}$$

$$\mathrm{Me,Me-OAE}_1 + \mathrm{Et,Et-OAE}_1 \xrightleftharpoons{\mathrm{H}^+} 2\ \mathrm{Me,Et-OAE}_1 \tag{iii}$$

Using the general mole balance equation (eq (45)) for all components i introduces additional unknown variables to the model, the molar extent ξ_j of each reaction j. The nomenclature of ξ_j follows the numbering of the reactions and the chain length n, if necessary.

Applying eq (45) to formaldehyde results in

$$\Delta n_{\mathrm{FA}} = -\sum_{n=2}^{8} \left(\xi_{\mathrm{ia},n} + \xi_{\mathrm{ib},n} + \xi_{\mathrm{ic},n}\right) + 3 \cdot \xi_{\mathrm{ii}} \tag{47}$$

This equation visualises that formaldehyde is consumed by the oligomerization reactions of all three ethers groups and is produced from trioxane decomposition. Similarly, eq (45) can be applied to all ethers, depicted exemplary for Me,Me-OAE$_\mathrm{n}$:

$$\Delta n_{\mathrm{Me,Me-OAE_1}} = -\xi_{\mathrm{ia,2}} - \xi_{\mathrm{iii}} \tag{48}$$

$$\Delta n_{\mathrm{Me,Me-OAE_2}} = \xi_{\mathrm{ia,2}} - \xi_{\mathrm{ia,3}} \tag{49}$$

$$\Delta n_{\mathrm{Me,Me-OAE_3}} = \xi_{\mathrm{ia,3}} - \xi_{\mathrm{ia,4}} \tag{50}$$

$$\Delta n_{\mathrm{Me,Me-OAE_4}} = \xi_{\mathrm{ia,4}} - \xi_{\mathrm{ia,5}} \tag{51}$$

$$\Delta n_{\mathrm{Me,Me-OAE_5}} = \xi_{\mathrm{ia,5}} - \xi_{\mathrm{ia,6}} \tag{52}$$

$$\Delta n_{\mathrm{Me,Me-OAE_6}} = \xi_{\mathrm{ia,6}} - \xi_{\mathrm{ia,7}} \tag{53}$$

$$\Delta n_{\mathrm{Me,Me-OAE_7}} = \xi_{\mathrm{ia,7}} - \xi_{\mathrm{ia,8}} \tag{54}$$

$$\Delta n_{\mathrm{Me,Me-OAE_8}} = \xi_{\mathrm{ia,8}} \tag{55}$$

Eqs (48)-(55) are similar to the resulting equations when considering Me,Et-OAE$_\mathrm{n}$ and

Me,Et-OAE$_\mathrm{n}$. The respective equation for trioxane is

$$\Delta n_\mathrm{TRI} = -\xi_\mathrm{ii} \tag{56}$$

Using these equations to replace all ξ_j in eq (47) step by step results in

$$\Delta n_\mathrm{FA} = -\sum_{n=2}^{8}\left[(n-1)\cdot\left(\Delta n_\mathrm{Me,Me-OAE_n} + \Delta n_\mathrm{Me,Et-OAE_n} + \Delta n_\mathrm{Et,Et-OAE_n}\right)\right] - 3\cdot\Delta n_\mathrm{TRI} \tag{57}$$

Similarily, the procedure can be applied to Me,Me-OAE$_1$ and Et,Et-OAE$_1$.

$$\Delta n_\mathrm{Me,Me-OAE_1} = -\frac{1}{2}\Delta n_\mathrm{Me,Et-OAE_1} - \sum_{n=2}^{8}\left(\Delta n_\mathrm{Me,Me-OAE_n} + \frac{1}{2}\cdot\Delta n_\mathrm{Me,Et-OAE_n}\right) \tag{58}$$

$$\Delta n_\mathrm{Et,Et-OAE_1} = -\frac{1}{2}\Delta n_\mathrm{Me,Et-OAE_1} - \sum_{n=2}^{8}\left(\Delta n_\mathrm{Et,Et-OAE_n} + \frac{1}{2}\cdot\Delta n_\mathrm{Me,Et-OAE_n}\right) \tag{59}$$

Using eqs (57)-(59) instead of eqs(47)-(56) reduces the number of mole balance equations from 23 to 3 by elimating all molar extents ξ_j and therefore simplifies the system of equations.

The system of nonlinear equations was implemented in the software Matlab (R2020a, The MathWorks Inc.). The integrated solver fsolve was applied with its standard parameters and the chain length was limited to $n = 8$ for all ethers (symmetric and asymmetric). Considering ethers with $n > 8$ was not necessary due to their negligible respective mole fractions and therefore would not have significantly changed the model results.

C.2 NMR Peak Assignment

C.2.1 System (Me,Me-OAE + trioxane)

The NMR spectrum of the system (Me,Me-OAE + trioxane) is shown in Figure 47. All assigned peaks are additionally listed in Table 32 along with their respective chemical shifts. The chemical shifts in the NMR spectra were referenced to the solvent $CDCl_3$ (δ = 77.16 ppm (TMS)). Peaks were assigned based on NMR measurement with pure substances Me,Me-OAE_1 to Me,Me-OAE_4, and TRI. In addition, peak assignment was compared to predictions from ChemDraw 17 (PerkinElmer Informatics, Inc.) and consistency was tested in a series of preliminary samples containing known ratios of the different ethers leading to unambigiously assigned peaks.

Table 32: ^{13}C-peak assignment and chemical shifts for the system (Me,Me-OAE + trioxane), reference = $CDCl_3$ (77.16 ppm (TMS)).

δ / ppm	Assignment		δ / ppm	Assignment	
54.26	$C^{0,1}_{\text{Me,Me-OAE}_1}$		89.03	$C^{3}_{\text{Me,Me-OAE}_5}$	
55.01	$C^{0,1}_{\text{Me,Me-OAE}_2}$		89.06	$C^{3}_{\text{Me,Me-OAE}_n}$	$(n \geq 6)$
55.05	$C^{0,1}_{\text{Me,Me-OAE}_3}$		92.98	$C^{1}_{\text{Me,Me-OAE}_2}$	
55.10	$C^{0,1}_{\text{Me,Me-OAE}_n}$	$(n \geq 4)$	93.44	$C^{1}_{\text{Me,Me-OAE}_3}$	
88.06	$C^{2}_{\text{Me,Me-OAE}_3}$		93.48	$C^{1}_{\text{Me,Me-OAE}_4}$	
88.55	$C^{2}_{\text{Me,Me-OAE}_4}$		93.51	$C^{1}_{\text{Me,Me-OAE}_n}$	$(n \geq 5)$
88.58	$C^{2}_{\text{Me,Me-OAE}_5}$		93.61	C^{1}_{TRI}	
88.62	$C^{2}_{\text{Me,Me-OAE}_n}$	$(n \geq 6)$	97.51	$C^{1}_{\text{Me,Me-OAE}_1}$	

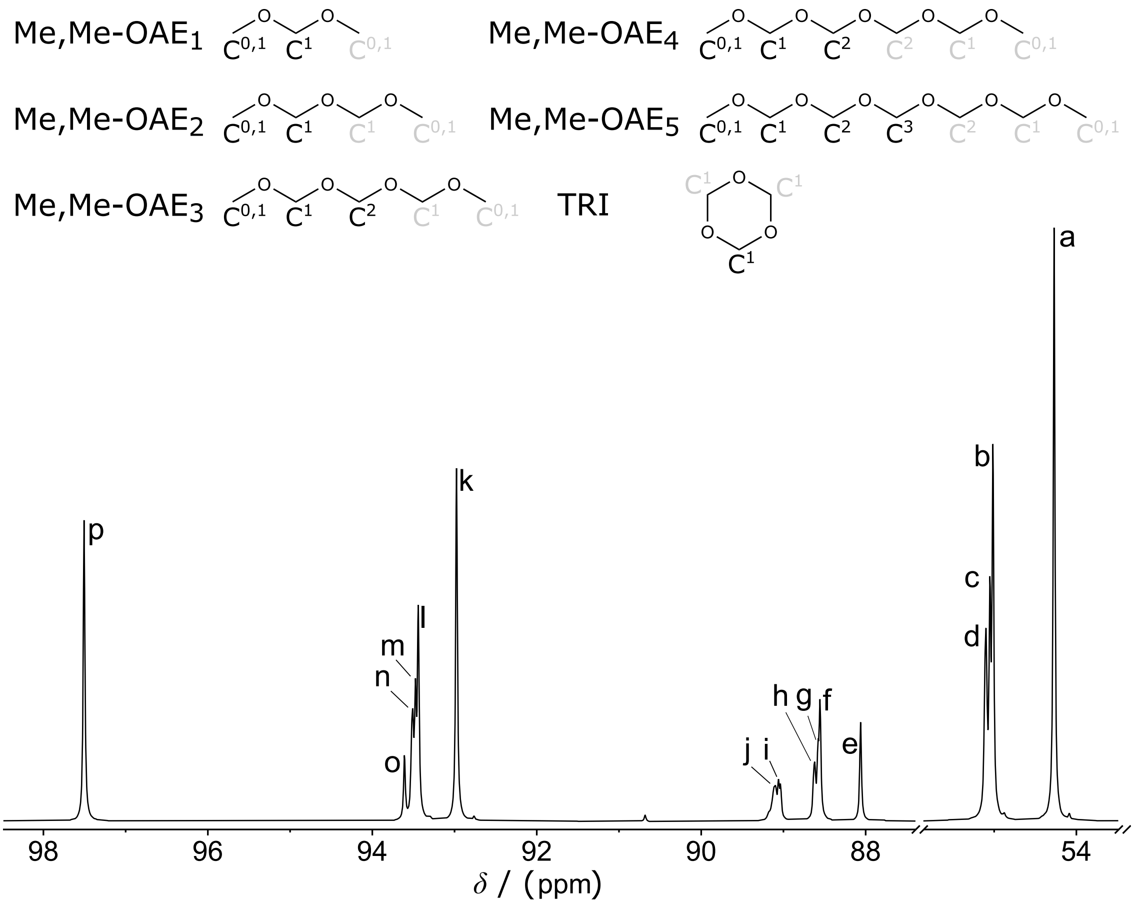

Figure 47: ^{13}C NMR spectrum and peak assignment for the system (Me,Me-OAE + TRI), reference = CDCl$_3$ (77.16 ppm (TMS)). Repeating carbon atoms are written in grey. Assigned peaks: a = $\mathrm{C}^{0,1}_{\mathrm{Me,Me-OAE_1}}$, b = $\mathrm{C}^{0,1}_{\mathrm{Me,Me-OAE_2}}$, c = $\mathrm{C}^{0,1}_{\mathrm{Me,Me-OAE_3}}$, d = $\mathrm{C}^{0,1}_{\mathrm{Me,Me-OAE_n}}(n \geq 4)$, e = $\mathrm{C}^{2}_{\mathrm{Me,Me-OAE_3}}$, f = $\mathrm{C}^{2}_{\mathrm{Me,Me-OAE_4}}$, g = $\mathrm{C}^{2}_{\mathrm{Me,Me-OAE_5}}$, h = $\mathrm{C}^{2}_{\mathrm{Me,Me-OAE_n}}(n \geq 6)$, i = $\mathrm{C}^{3}_{\mathrm{Me,Me-OAE_5}}$, j = $\mathrm{C}^{3}_{\mathrm{Me,Me-OAE_n}}(n \geq 6)$, k = $\mathrm{C}^{1}_{\mathrm{Me,Me-OAE_2}}$, l = $\mathrm{C}^{1}_{\mathrm{Me,Me-OAE_3}}$, m = $\mathrm{C}^{1}_{\mathrm{Me,Me-OAE_4}}$, n = $\mathrm{C}^{1}_{\mathrm{Me,Me-OAE_n}}(n \geq 5)$, o = $\mathrm{C}^{1}_{\mathrm{TRI}}$, p = $\mathrm{C}^{1}_{\mathrm{Me,Me-OAE_1}}$.

C.2.2 System (Et,Et-OAE + trioxane)

The NMR spectrum of the system (Et,Et-OAE + trioxane) is shown in Figure 48. All assigned peaks are additionally listed in Table 33 along with their respective chemical shifts. Peaks were assigned based on NMR measurement with the pure substance Et,Et-OAE$_1$ and the findings from the system (Me,Me-OAE + trioxane) due to the chemical similarity. In addition, the consistency was tested in a series of preliminary reaction samples, containing varying ratios of Et,Et-OAE$_1$ and trioxane, that were reacted to chemical equilibrium.

Table 33: ^{13}C-peak assignment and chemical shifts for the system (Et,Et-OAE + trioxane), reference = CDCl$_3$ (77.16 ppm (TMS)).

δ / ppm	Assignment	
14.98	$C^{0,1}_{\mathrm{Et,Et-OAE_2}}$	
15.01	$C^{0,1}_{\mathrm{Et,Et-OAE_n}}$	($n \geq 3$)
15.08	$C^{0,1}_{\mathrm{Et,Et-OAE_1}}$	
62.85	$C^{0,2}_{\mathrm{Et,Et-OAE_1}}$	
63.52	$C^{0,2}_{\mathrm{Et,Et-OAE_2}}$	
63.61	$C^{0,2}_{\mathrm{Et,Et-OAE_3}}$	
63.67	$C^{0,2}_{\mathrm{Et,Et-OAE_n}}$	($n \geq 4$)
87.81	$C^{2}_{\mathrm{Et,Et-OAE_3}}$	
88.31	$C^{2}_{\mathrm{Et,Et-OAE_4}}$	
88.35	$C^{2}_{\mathrm{Et,Et-OAE_5}}$	
88.40	$C^{2}_{\mathrm{Et,Et-OAE_n}}$	($n \geq 6$)
88.79	$C^{3}_{\mathrm{Et,Et-OAE_5}}$	
88.84 – 88.91	$C^{3}_{\mathrm{Et,Et-OAE_n}}$	($n \geq 6$)
91.48	$C^{1}_{\mathrm{Et,Et-OAE_2}}$	
91.92	$C^{1}_{\mathrm{Et,Et-OAE_3}}$	
91.98	$C^{1}_{\mathrm{Et,Et-OAE_4}}$	
92.03	$C^{1}_{\mathrm{Et,Et-OAE_n}}$	($n \geq 5$)
93.61	C^{1}_{TRI}	
94.92	$C^{1}_{\mathrm{Et,Et-OAE_1}}$	

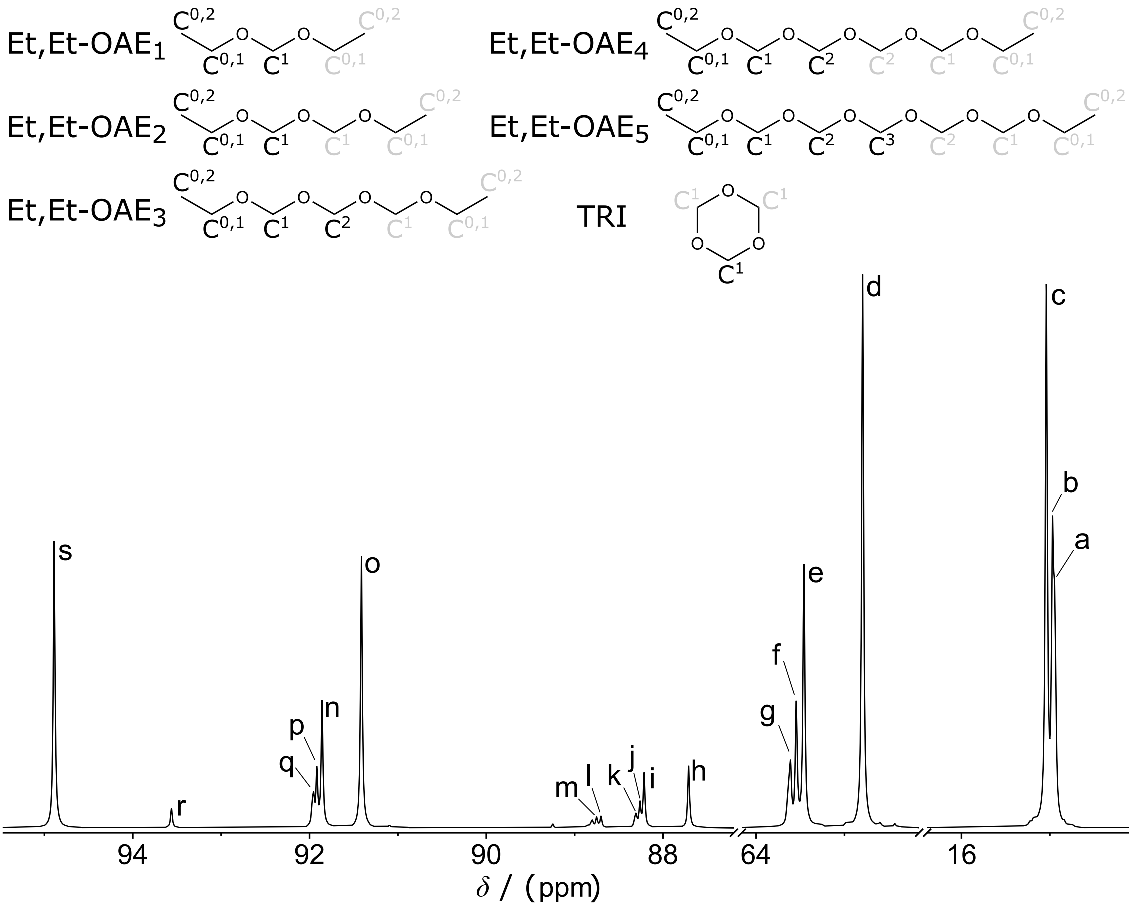

Figure 48: ^{13}C NMR spectrum and peak assignment for the system (Et,Et-OAE + TRI), reference = $CDCl_3$ (77.16 ppm (TMS)). Repeating carbon atoms are written in grey. Assigned peaks: a = $C^{0,1}_{\mathrm{Et,Et-OAE_2}}$, b = $C^{0,1}_{\mathrm{Et,Et-OAE_n}}$ $(n \geq 3)$, c = $C^{0,1}_{\mathrm{Et,Et-OAE_1}}$, d = $C^{0,2}_{\mathrm{Et,Et-OAE_1}}$, e = $C^{0,2}_{\mathrm{Et,Et-OAE_2}}$, f = $C^{0,2}_{\mathrm{Et,Et-OAE_3}}$, g = $C^{0,2}_{\mathrm{Et,Et-OAE_n}}$ $(n \geq 4)$, h = $C^{2}_{\mathrm{Et,Et-OAE_3}}$, i = $C^{2}_{\mathrm{Et,Et-OAE_4}}$, j = $C^{2}_{\mathrm{Et,Et-OAE_5}}$, k = $C^{2}_{\mathrm{Et,Et-OAE_n}}$ $(n \geq 6)$, l = $C^{3}_{\mathrm{Et,Et-OAE_5}}$, m = $C^{3}_{\mathrm{Et,Et-OAE_n}}$ $(n \geq 6)$, n = $C^{1}_{\mathrm{Et,Et-OAE_2}}$, o = $C^{1}_{\mathrm{Et,Et-OAE_3}}$, p = $C^{1}_{\mathrm{Et,Et-OAE_4}}$,q = $C^{1}_{\mathrm{Et,Et-OAE_n}}$ $(n \geq 5)$, r = C^{1}_{TRI}, s = $C^{1}_{\mathrm{Et,Et-OAE_1}}$.

C.2.3 System (Bu,Bu-OAE + trioxane)

The NMR spectrum of the system (Bu,Bu-OAE + trioxane) is shown in Figure 49. All assigned peaks are additionally listed in Table 34 along with their respective chemical shifts. Peaks were assigned similarly to the system (Et,Et-OAE + trioxane).

Table 34: ^{13}C-peak assignment and chemical shifts for the system (Bu,Bu-OAE + trioxane), reference = $CDCl_3$ (77.16 ppm (TMS)).

δ / ppm	Assignment	
13.82	$C^{0,1}_{\mathrm{Bu,Bu-OAE_n}}$	$(n \geq 2)$
13.86	$C^{0,1}_{\mathrm{Bu,Bu-OAE_1}}$	
19.69	$C^{0,2}_{\mathrm{Bu,Bu-OAE_n}}$	$(n \geq 2)$
19.77	$C^{0,2}_{\mathrm{Bu,Bu-OAE_1}}$	
32.25	$C^{0,3}_{\mathrm{Bu,Bu-OAE_n}}$	$(n \geq 2)$
32.33	$C^{0,3}_{\mathrm{Bu,Bu-OAE_1}}$	
67.28	$C^{0,4}_{\mathrm{Bu,Bu-OAE_1}}$	
67.95	$C^{0,4}_{\mathrm{Bu,Bu-OAE_2}}$	
68.01	$C^{0,4}_{\mathrm{Bu,Bu-OAE_3}}$	
68.07	$C^{0,4}_{\mathrm{Bu,Bu-OAE_n}}$	$(n \geq 4)$
87.49	$C^{2}_{\mathrm{Bu,Bu-OAE_3}}$	
88.03	$C^{2}_{\mathrm{Bu,Bu-OAE_4}}$	
88.08	$C^{2}_{\mathrm{Bu,Bu-OAE_5}}$	
88.12	$C^{2}_{\mathrm{Bu,Bu-OAE_n}}$	$(n \geq 6)$
88.57	$C^{3}_{\mathrm{Bu,Bu-OAE_5}}$	
88.63 – 88.69	$C^{3}_{\mathrm{Bu,Bu-OAE_n}}$	$(n \geq 6)$
91.50	$C^{1}_{\mathrm{Bu,Bu-OAE_2}}$	
92.00	$C^{1}_{\mathrm{Bu,Bu-OAE_3}}$	
92.05	$C^{1}_{\mathrm{Bu,Bu-OAE_4}}$	
92.10	$C^{1}_{\mathrm{Bu,Bu-OAE_n}}$	$(n \geq 5)$
93.61	C^{1}_{TRI}	
95.33	$C^{1}_{\mathrm{Bu,Bu-OAE_1}}$	

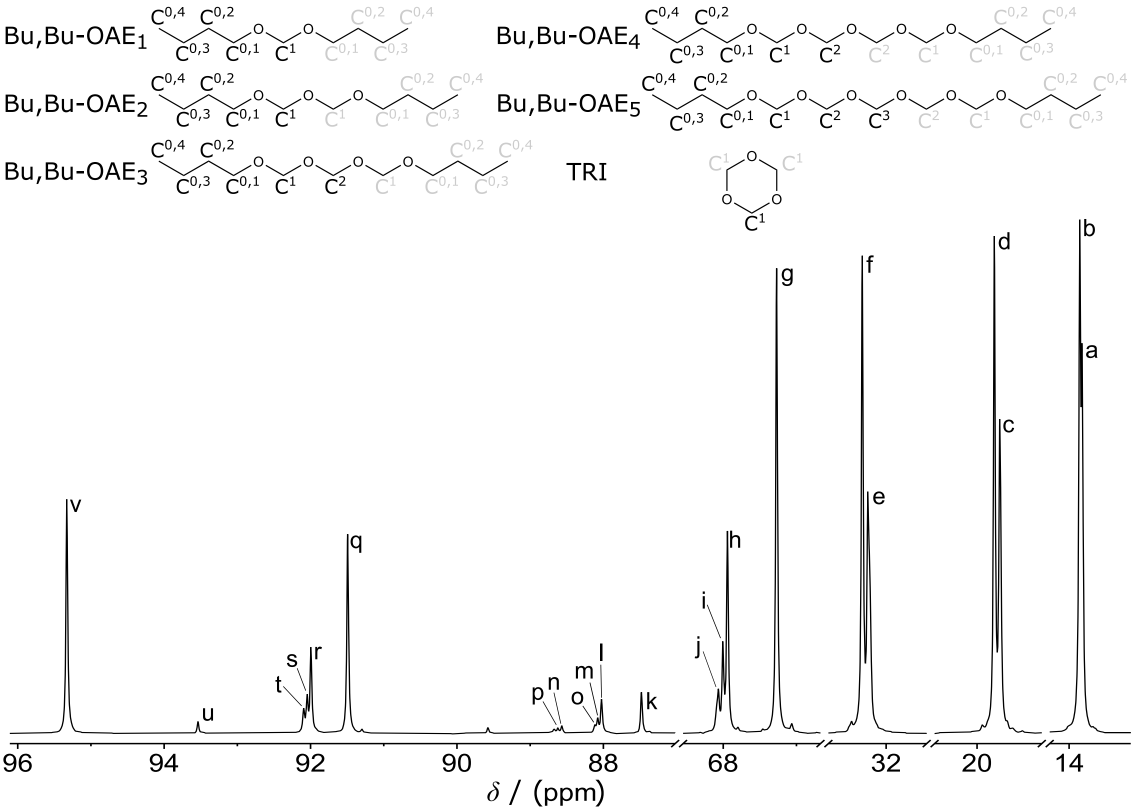

Figure 49: ^{13}C NMR spectrum and peak assignment for the system (Bu,Bu-OAE + TRI), reference = CDCl$_3$ (77.16 ppm (TMS)). Repeating carbon atoms are written in grey. Assigned peaks: a = $C^{0,1}_{\text{Bu,Bu-OAE}_n}$ ($n \geq 2$), b = $C^{0,1}_{\text{Bu,Bu-OAE}_1}$, c = $C^{0,2}_{\text{Bu,Bu-OAE}_n}$ ($n \geq 2$), d = $C^{0,2}_{\text{Bu,Bu-OAE}_1}$, e = $C^{0,3}_{\text{Bu,Bu-OAE}_n}$ ($n \geq 2$), f = $C^{0,3}_{\text{Bu,Bu-OAE}_1}$, g = $C^{0,4}_{\text{Bu,Bu-OAE}_1}$, h = $C^{0,4}_{\text{Bu,Bu-OAE}_2}$, i = $C^{0,4}_{\text{Bu,Bu-OAE}_3}$, j = $C^{0,4}_{\text{Bu,Bu-OAE}_n}$ ($n \geq 4$), k = $C^{2}_{\text{Bu,Bu-OAE}_3}$, l = $C^{2}_{\text{Bu,Bu-OAE}_4}$, m = $C^{2}_{\text{Bu,Bu-OAE}_5}$, n = $C^{2}_{\text{Bu,Bu-OAE}_n}$ ($n \geq 6$), o = $C^{3}_{\text{Bu,Bu-OAE}_5}$, p = $C^{3}_{\text{Bu,Bu-OAE}_n}$ ($n \geq 6$),q = $C^{1}_{\text{Bu,Bu-OAE}_2}$, r = $C^{1}_{\text{Bu,Bu-OAE}_3}$, s = $C^{1}_{\text{Bu,Bu-OAE}_4}$, t = $C^{1}_{\text{Bu,Bu-OAE}_n}$ ($n \geq 5$), u = C^{1}_{TRI}, v = $C^{1}_{\text{Bu,Bu-OAE}_1}$.

C.2.4 System (Me,Me-OAE + Me,Et-OAE + Et,Et-OAE + trioxane)

The NMR spectrum of the system (Me,Me-OAE + Me,Et-OAE + Et,Et-OAE + trioxane) is shown in Figure 50. All assigned peaks are additionally listed in Table 35 along with their respective chemical shifts. Note that the chemical shifts of the symmetic ethers slightly changed compared to Tables 32 and 33. This is attributed to the altered chemical environment.

The peak assignment in the described system was particularly challenging. The peaks of the asymmetric ethers strongly overlap with the symmetric ethers due to their similar chemical structure. In addition, only mixtures of asymmetric and symmetric ethers were obtained from the reaction experiments. Peaks were assigned stepwise from mixtures with varying amounts of symmetric and asymmetric ethers. The resulting spectra were then compared to mixtures comprising (Me,Me-OAE + Et,Et-OAE + trioxane) that were prepared individually beforehand. The peaks from the asymmetric ethers were therefore unambigiously identified. However, only ethers with chain lengths up to $n \leq 3$ showed individual peaks thus limiting the analysis.

Table 35: ^{13}C-peak assignment and chemical shifts for the system (Me,Me-OAE + Me,Et-OAE + Et,Et-OAE + trioxane), reference = $CDCl_3$ (77.16 ppm (TMS)).

δ / ppm	Assignment
14.91	$C^{0,1'}_{\text{Me,Et-OAE}_\text{n}}$ / $C^{0,1}_{\text{Et,Et-OAE}_\text{n}}$ $(n \geq 2)$
14.97	$C^{0,1'}_{\text{Me,Et-OAE}_1}$ / $C^{0,1}_{\text{Et,Et-OAE}_1}$
54.27	$C^{0,1}_{\text{Me,Me-OAE}_1}$
54.32	$C^{0,1}_{\text{Me,Et-OAE}_1}$
54.98	$C^{0,1}_{\text{Me,Et-OAE}_2}$
55.02	$C^{0,1}_{\text{Me,Me-OAE}_2}$
55.05	$C^{0,1}_{\text{Me,Et-OAE}_\text{n}}$ $(n \geq 3)$
55.10	$C^{0,1}_{\text{Me,Me-OAE}_\text{n}}$ $(n \geq 3)$
62.83	$C^{0,2'}_{\text{Me,Et-OAE}_1}$ / $C^{0,2}_{\text{Et,Et-OAE}_1}$
63.50	$C^{0,2}_{\text{Et,Et-OAE}_2}$
63.55	$C^{0,2'}_{\text{Me,Et-OAE}_2}$
63.58	$C^{0,2}_{\text{Et,Et-OAE}_\text{n}}$ $(n \geq 3)$
63.64	$C^{0,2'}_{\text{Me,Et-OAE}_\text{n}}$ $(n \geq 3)$
87.82	$C^{2}_{\text{Et,Et-OAE}_3}$
87.84	$C^{2}_{\text{Me,Et-OAE}_3}$
87.86	$C^{2}_{\text{Me,Me-OAE}_3}$
91.46	$C^{1}_{\text{Et,Et-OAE}_2}$
91.47	$C^{1'}_{\text{Me,Et-OAE}_2}$
91.91	$C^{1}_{\text{Et,Et-OAE}_3}$
91.95	$C^{1'}_{\text{Me,Et-OAE}_3}$
92.84	$C^{1}_{\text{Me,Et-OAE}_2}$
92.86	$C^{1}_{\text{Me,Me-OAE}_2}$
93.31	$C^{1}_{\text{Me,Et-OAE}_3}$
93.35	$C^{1}_{\text{Me,Me-OAE}_3}$
93.58	C^{1}_{TRI}
94.92	$C^{1}_{\text{Et,Et-OAE}_1}$
96.21	$C^{1}_{\text{Me,Et-OAE}_1}$
97.51	$C^{1}_{\text{Me,Me-OAE}_1}$

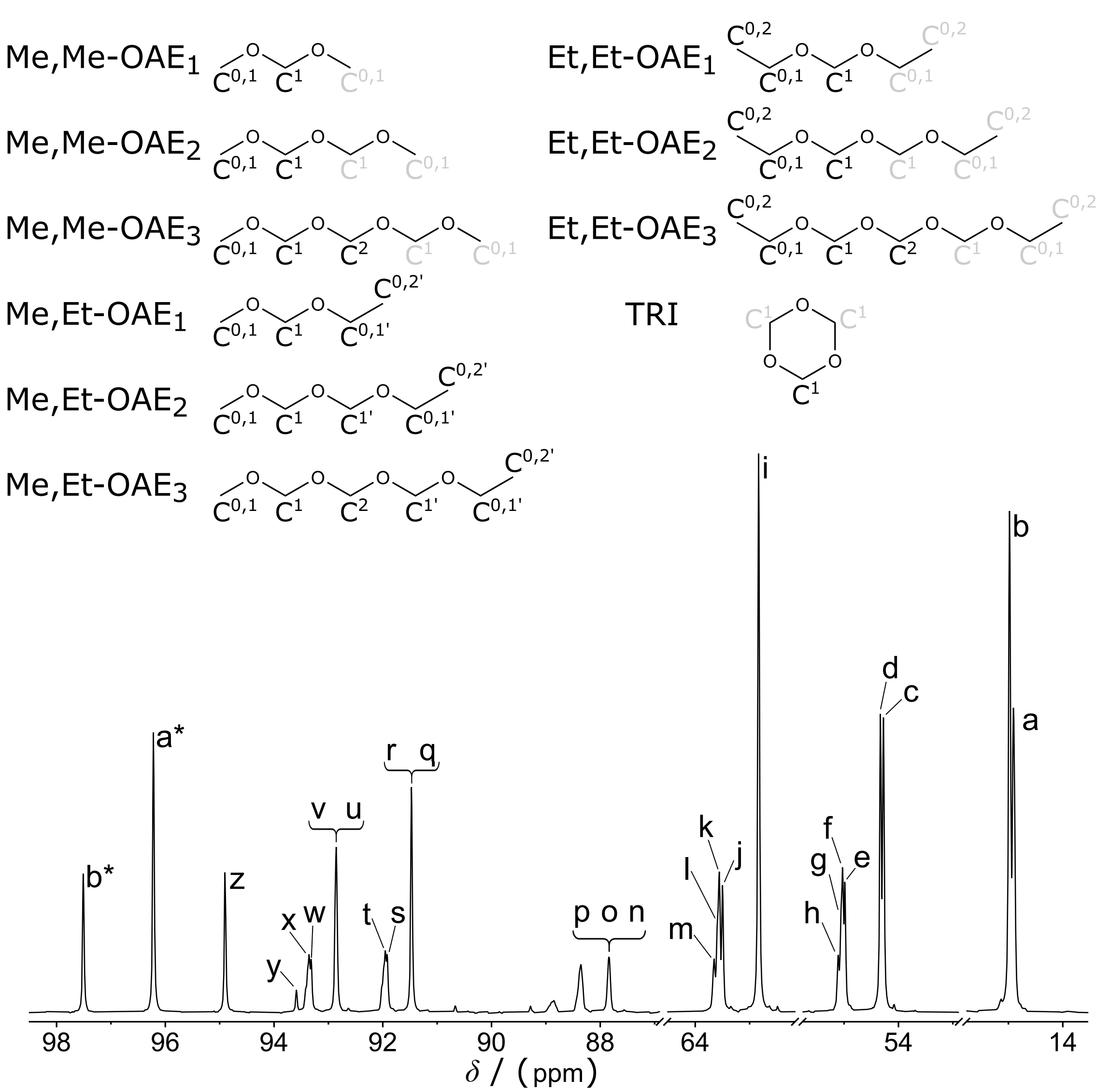

Figure 50: ^{13}C NMR spectrum and peak assignment for the system (Me,Me-OAE + Me,Et-OAE + Et,Et-OAE + trioxane), reference = $CDCl_3$ (77.16 ppm (TMS)). Repeating carbon atoms are written in grey. Assigned peaks: a = $C^{0,1'}_{\text{Me,Et-OAE}_\text{n}}$ / $C^{0,1}_{\text{Et,Et-OAE}_\text{n}}$ ($n \geq 2$), b = $C^{0,1'}_{\text{Me,Et-OAE}_1}$ / $C^{0,1}_{\text{Et,Et-OAE}_1}$, c = $C^{0,1}_{\text{Me,Me-OAE}_1}$, d = $C^{0,1}_{\text{Me,Et-OAE}_1}$, e = $C^{0,1}_{\text{Me,Et-OAE}_2}$, f = $C^{0,1}_{\text{Me,Me-OAE}_2}$, g = $C^{0,1}_{\text{Me,Et-OAE}_\text{n}}$ ($n \geq 3$), h = $C^{0,1}_{\text{Me,Me-OAE}_\text{n}}$ ($n \geq 3$), i = $C^{0,2'}_{\text{Me,Et-OAE}_1}$ / $C^{0,2}_{\text{Et,Et-OAE}_1}$, j = $C^{0,2}_{\text{Et,Et-OAE}_2}$, k = $C^{0,2'}_{\text{Me,Et-OAE}_2}$, l = $C^{0,2}_{\text{Et,Et-OAE}_\text{n}}$ ($n \geq 3$), m = $C^{0,2'}_{\text{Me,Et-OAE}_\text{n}}$ ($n \geq 3$), n = $C^{2}_{\text{Et,Et-OAE}_3}$, o = $C^{2}_{\text{Me,Et-OAE}_3}$, p = $C^{2}_{\text{Me,Me-OAE}_3}$,q = $C^{1}_{\text{Et,Et-OAE}_2}$, r = $C^{1'}_{\text{Me,Et-OAE}_2}$, s = $C^{1}_{\text{Et,Et-OAE}_3}$, t = $C^{1'}_{\text{Me,Et-OAE}_3}$, u = $C^{1}_{\text{Me,Et-OAE}_2}$, v = $C^{1}_{\text{Me,Me-OAE}_2}$, w = $C^{1}_{\text{Me,Et-OAE}_3}$, x = $C^{1}_{\text{Me,Me-OAE}_3}$, y = C^{1}_{TRI}, z = $C^{1}_{\text{Et,Et-OAE}_1}$, a* = $C^{1}_{\text{Me,Et-OAE}_1}$, b* = $C^{1}_{\text{Me,Me-OAE}_1}$.

C.2.5 System (Me,Me-OAE + Me,Bu-OAE + Bu,Bu-OAE + trioxane)

The NMR spectrum of the system (Me,Me-OAE + Me,Bu-OAE + Bu,Bu-OAE + trioxane) is shown in Figure 51. All assigned peaks are additionally listed in Table 36 along with their respective chemical shifts. Note that the chemical shifts of the symmetic ethers slightly changed compared to Tables 32 and 34. This is attributed to the altered chemical environment. Peaks were assigned similarly to the system (Me,Me-OAE + Me,Et-OAE + Et,Et-OAE + trioxane).

Table 36: ^{13}C-peak assignment and chemical shifts for the system (Me,Me-OAE + Me,Bu-OAE + Bu,Bu-OAE + trioxane), reference = $CDCl_3$ (77.16 ppm (TMS)).

δ / ppm	Assignment
13.86	$C^{0,1'}_{\mathrm{Me,Bu{-}OAE_n}}$ / $C^{0,1}_{\mathrm{Bu,Bu{-}OAE_n}}$ $(n \geq 1)$
19.69	$C^{0,2'}_{\mathrm{Me,Bu{-}OAE_n}}$ / $C^{0,2}_{\mathrm{Bu,Bu{-}OAE_n}}$ $(n \geq 2)$
19.77	$C^{0,2'}_{\mathrm{Me,Bu{-}OAE_1}}$ / $C^{0,2}_{\mathrm{Bu,Bu{-}OAE_1}}$
32.25	$C^{0,3'}_{\mathrm{Me,Bu{-}OAE_n}}$ / $C^{0,3}_{\mathrm{Bu,Bu{-}OAE_n}}$ $(n \geq 2)$
32.33	$C^{0,3'}_{\mathrm{Me,Bu{-}OAE_1}}$ / $C^{0,3}_{\mathrm{Bu,Bu{-}OAE_1}}$
54.33	$C^{0,1}_{\mathrm{Me,Me{-}OAE_1}}$
54.39	$C^{0,1}_{\mathrm{Me,Bu{-}OAE_1}}$
55.05	$C^{0,1}_{\mathrm{Me,Bu{-}OAE_2}}$
55.08	$C^{0,1}_{\mathrm{Me,Me{-}OAE_2}}$
55.10	$C^{0,1}_{\mathrm{Me,Bu{-}OAE_n}}$ $(n \geq 3)$
55.15	$C^{0,1}_{\mathrm{Me,Me{-}OAE_n}}$ $(n \geq 3)$
67.28	$C^{0,4'}_{\mathrm{Me,Bu{-}OAE_1}}$ / $C^{0,4}_{\mathrm{Bu,Bu{-}OAE_1}}$
67.97	$C^{0,4}_{\mathrm{Bu,Bu{-}OAE_2}}$
68.01	$C^{0,4'}_{\mathrm{Me,Bu{-}OAE_2}}$
68.04	$C^{0,4}_{\mathrm{Bu,Bu{-}OAE_n}}$ $(n \geq 3)$
68.10	$C^{0,4'}_{\mathrm{Me,Bu{-}OAE_n}}$ $(n \geq 3)$
87.64	$C^{2}_{\mathrm{Bu,Bu{-}OAE_3}}$
87.71	$C^{2}_{\mathrm{Me,Bu{-}OAE_3}}$
87.78	$C^{2}_{\mathrm{Me,Me{-}OAE_3}}$
91.58	$C^{1}_{\mathrm{Bu,Bu{-}OAE_2}}$
91.63	$C^{1'}_{\mathrm{Me,Bu{-}OAE_2}}$
92.07	$C^{1}_{\mathrm{Bu,Bu{-}OAE_3}}$
92.11	$C^{1'}_{\mathrm{Me,Bu{-}OAE_3}}$
92.13	$C^{1}_{\mathrm{Bu,Bu{-}OAE_n}}$ $(n \geq 4)$
92.17	$C^{1'}_{\mathrm{Me,Bu{-}OAE_n}}$ $(n \geq 4)$
92.78	$C^{1}_{\mathrm{Me,Bu{-}OAE_2}}$
92.83	$C^{1}_{\mathrm{Me,Me{-}OAE_2}}$
93.27	$C^{1}_{\mathrm{Me,Bu{-}OAE_3}}$
93.32	$C^{1}_{\mathrm{Me,Me{-}OAE_3}}$
93.34	$C^{1}_{\mathrm{Me,Bu{-}OAE_n}}$ $(n \geq 4)$
93.38	$C^{1}_{\mathrm{Me,Me{-}OAE_n}}$ $(n \geq 4)$
93.58	C^{1}_{TRI}
95.33	$C^{1}_{\mathrm{Bu,Bu{-}OAE_1}}$
96.43	$C^{1}_{\mathrm{Me,Bu{-}OAE_1}}$
97.51	$C^{1}_{\mathrm{Me,Me{-}OAE_1}}$

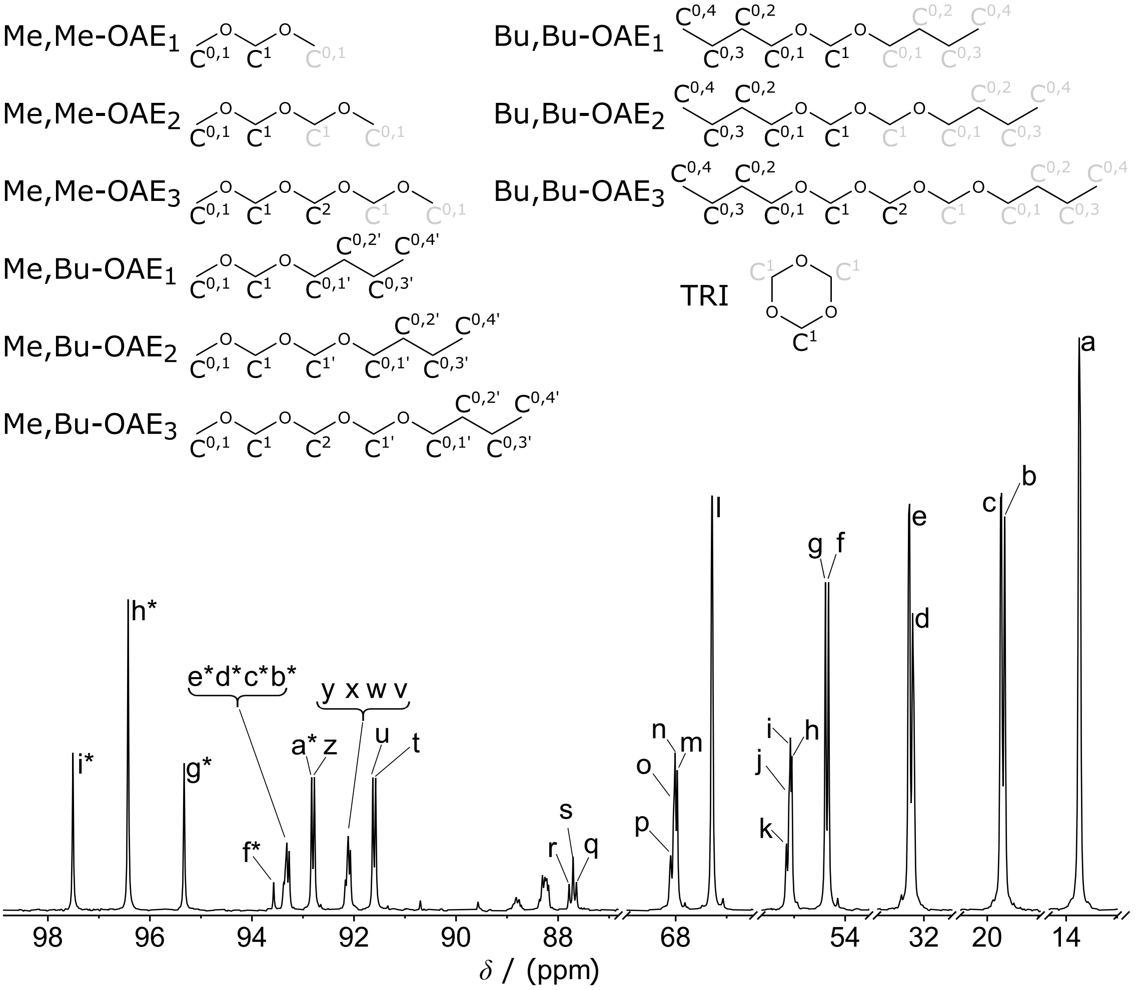

Figure 51: ^{13}C NMR spectrum and peak assignment for the system (Me,Me-OAE + Me,Bu-OAE + Bu,Bu-OAE + trioxane), reference = CDCl$_3$ (77.16 ppm (TMS)). Repeating carbon atoms are written in grey. Assigned peaks: a = $C^{0,1'}_{\text{Me,Bu-OAE}_\text{n}}$ / $C^{0,1}_{\text{Bu,Bu-OAE}_\text{n}}$ ($n \geq 1$), b = $C^{0,2'}_{\text{Me,Bu-OAE}_\text{n}}$ / $C^{0,2}_{\text{Bu,Bu-OAE}_\text{n}}$ ($n \geq 2$), c = $C^{0,2'}_{\text{Me,Bu-OAE}_1}$ / $C^{0,2}_{\text{Bu,Bu-OAE}_1}$, d = $C^{0,3'}_{\text{Me,Bu-OAE}_\text{n}}$ / $C^{0,3}_{\text{Bu,Bu-OAE}_\text{n}}$ ($n \geq 2$), e = $C^{0,3'}_{\text{Me,Bu-OAE}_1}$ / $C^{0,3}_{\text{Bu,Bu-OAE}_1}$, f = $C^{0,1}_{\text{Me,Me-OAE}_1}$, g = $C^{0,1}_{\text{Me,Bu-OAE}_1}$, h = $C^{0,1}_{\text{Me,Bu-OAE}_2}$, i = $C^{0,1}_{\text{Me,Me-OAE}_2}$, j = $C^{0,1}_{\text{Me,Bu-OAE}_\text{n}}$ ($n \geq 3$), k = $C^{0,1}_{\text{Me,Me-OAE}_\text{n}}$ ($n \geq 3$), l = $C^{0,4'}_{\text{Me,Bu-OAE}_1}$ / $C^{0,4}_{\text{Bu,Bu-OAE}_1}$, m = $C^{0,4}_{\text{Bu,Bu-OAE}_2}$, n = $C^{0,4'}_{\text{Me,Bu-OAE}_2}$, o = $C^{0,4}_{\text{Bu,Bu-OAE}_\text{n}}$ ($n \geq 3$), p = $C^{0,4'}_{\text{Me,Bu-OAE}_\text{n}}$ ($n \geq 3$), q = $C^{2}_{\text{Bu,Bu-OAE}_3}$, r = $C^{2}_{\text{Me,Bu-OAE}_3}$, s = $C^{2}_{\text{Me,Me-OAE}_3}$, t = $C^{1}_{\text{Bu,Bu-OAE}_2}$, u = $C^{1'}_{\text{Me,Bu-OAE}_2}$, v = $C^{1}_{\text{Bu,Bu-OAE}_3}$, w = $C^{1'}_{\text{Me,Bu-OAE}_3}$, x = $C^{1}_{\text{Bu,Bu-OAE}_\text{n}}$ ($n \geq 4$), y = $C^{1'}_{\text{Me,Bu-OAE}_\text{n}}$ ($n \geq 4$), z = $C^{1}_{\text{Me,Bu-OAE}_2}$, a* = $C^{1}_{\text{Me,Me-OAE}_2}$, b* = $C^{1}_{\text{Me,Bu-OAE}_3}$, c* = $C^{1}_{\text{Me,Me-OAE}_3}$, d* = $C^{1}_{\text{Me,Bu-OAE}_\text{n}}$ ($n \geq 4$), e* = $C^{1}_{\text{Me,Me-OAE}_\text{n}}$ ($n \geq 4$), f* = C^{1}_{TRI}, g* = $C^{1}_{\text{Bu,Bu-OAE}_1}$, h* = $C^{1}_{\text{Me,Bu-OAE}_1}$, i* = $C^{1}_{\text{Me,Me-OAE}_1}$.

C.3 Experimental Data

The numerical results from the NMR analysis for the reaction experiments E1-E4 and E5-E11 are shown in Table 37 and Table 38, respectively.

Table 37: Mole fractions from the NMR analysis for the reaction experiments E1-E4. OAE with $n \geq 6$ could not be reliably evaluated individually and are therefore combined.

	T / K	mole fraction / mol/mol						
		Et,Et-OAE$_1$	Et,Et-OAE$_2$	Et,Et-OAE$_3$	Et,Et-OAE$_4$	Et,Et-OAE$_5$	Et,Et-OAE$_{6+}$	TRI
E1	303.15	0.5343	0.2508	0.1174	0.0487	0.0209	0.0158	0.0120
	323.15	0.5444	0.2500	0.1115	0.0465	0.0212	0.0127	0.0136
	343.15	0.5655	0.2457	0.1076	0.0386	0.0148	0.0132	0.0146
	363.15	0.6115	0.2333	0.0915	0.0307	0.0123	0.0063	0.0144
E2	303.15	0.5926	0.2431	0.0953	0.0364	0.0145	0.0097	0.0085
	323.15	0.6012	0.2407	0.0932	0.0351	0.0138	0.0064	0.0095
	343.15	0.6343	0.2328	0.0837	0.0260	0.0081	0.0044	0.0107
	363.15	0.6650	0.2225	0.0724	0.0226	0.0069	0.0017	0.0088

	T / K	mole fraction / mol/mol						
		Bu,Bu-OAE$_1$	Bu,Bu-OAE$_2$	Bu,Bu-OAE$_3$	Bu,Bu-OAE$_4$	Bu,Bu-OAE$_5$	Bu,Bu-OAE$_{6+}$	TRI
E3	303.15	0.5739	0.2482	0.1008	0.0434	0.0169	0.0076	0.0092
	323.15	0.5770	0.2443	0.1035	0.0410	0.0160	0.0084	0.0098
	343.15	0.5892	0.2420	0.0968	0.0362	0.0169	0.0066	0.0122
	363.15	0.6499	0.2274	0.0769	0.0249	0.0093	0.0017	0.0097
E4	303.15	0.6070	0.2373	0.0950	0.0329	0.0133	0.0073	0.0072
	323.15	0.6111	0.2358	0.0916	0.0340	0.0125	0.0056	0.0094
	343.15	0.6438	0.2277	0.0808	0.0268	0.0098	0.0037	0.0074
	363.15	0.6893	0.2148	0.0632	0.0188	0.0062	0.0012	0.0064

Table 38: Mole fractions from the NMR analysis for the reaction experiments T1-T4. OAE with $n \geq 4$ could not be reliably evaluated individually and are therefore combined.

	mole fraction / mol/mol										
	Me,Me-OAE$_1$	Me,Me-OAE$_2$	Me,Me-OAE$_3$	Me,Et-OAE$_1$	Me,Et-OAE$_2$	Me,Et-OAE$_3$	Et,Et-OAE$_1$	Et,Et-OAE$_2$	Et,Et-OAE$_3$	OAE$_{4+}$	TRI
E5	0.3608	0.1072	0.0373	0.2686	0.0843	0.0251	0.0582	0.0178	0.0069	0.0295	0.0044
E6	0.0328	0.0104	0.0015	0.2367	0.0837	0.0339	0.3681	0.1323	0.0477	0.0467	0.0060
E7	0.1392	0.0589	0.0179	0.2935	0.1248	0.0572	0.1574	0.0619	0.0355	0.0459	0.0079

	mole fraction / mol/mol										
	Me,Me-OAE$_1$	Me,Me-OAE$_2$	Me,Me-OAE$_3$	Me,Bu-OAE$_1$	Me,Bu-OAE$_2$	Me,Bu-OAE$_3$	Bu,Bu-OAE$_1$	Bu,Bu-OAE$_2$	Bu,Bu-OAE$_3$	OAE$_{4+}$	TRI
E8	0.3184	0.1312	0.0621	0.2149	0.0913	0.0408	0.0389	0.0156	0.0088	0.0698	0.0083
E9	0.0357	0.0138	0.0005	0.2259	0.0823	0.0416	0.3514	0.1302	0.0572	0.0547	0.0066
E10	0.1394	0.0635	0.0325	0.2852	0.1221	0.0530	0.1506	0.0599	0.0341	0.0531	0.0067

	mole fraction / mol/mol					
	Me,Me-OAE$_1$	Me,Et-OAE$_1$	Et,Et-OAE$_1$	Et,Bu-OAE$_1$	Bu,Bu-OAE$_1$	Me,Bu-OAE$_1$
E11	0.1275	0.2297	0.0994	0.2063	0.1046	0.2326

C.4 Comparison between Model and Experimental Results

The experimental results of the reaction experiments E1-E4, E6, E7, E9, and E10 are compared to the model calculations in Figures 52- 57. The diagrams of the remaining reaction experiments ars shown in the main part. In addition, the results from the experiment E1 at T = 303.15 K and T = 363.15 K are compared to the model calculations performed with the correlation of the present work (correlation parameters are given in the main part) in Figure 58.

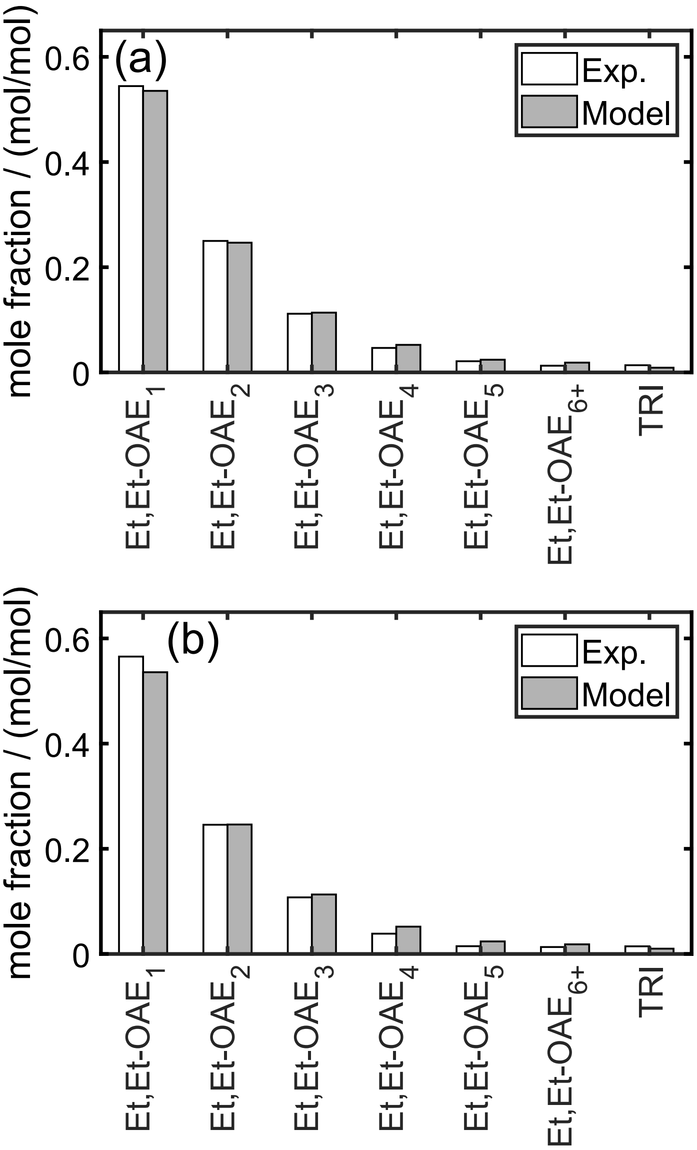

Figure 52: Comparison between the experiment and the model results for reaction experiment E1 ((a) T = 323.15 K, (b) T = 343.15 K).

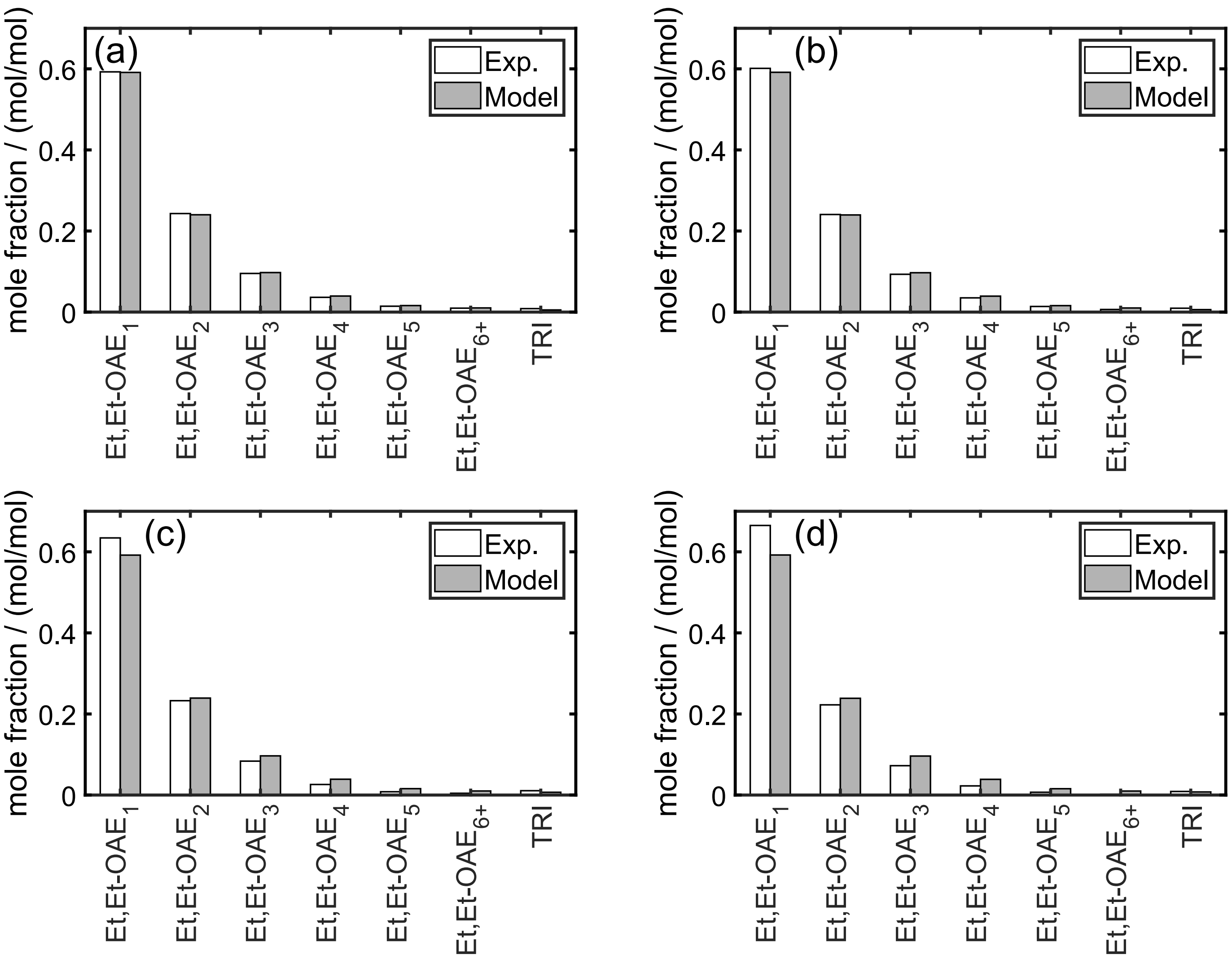

Figure 53: Comparison between the experiment and the model results for reaction experiment E2 ((a) T = 303.15 K, (b) T = 323.15 K, (c) T = 343.15 K, (d) T = 363.15 K).

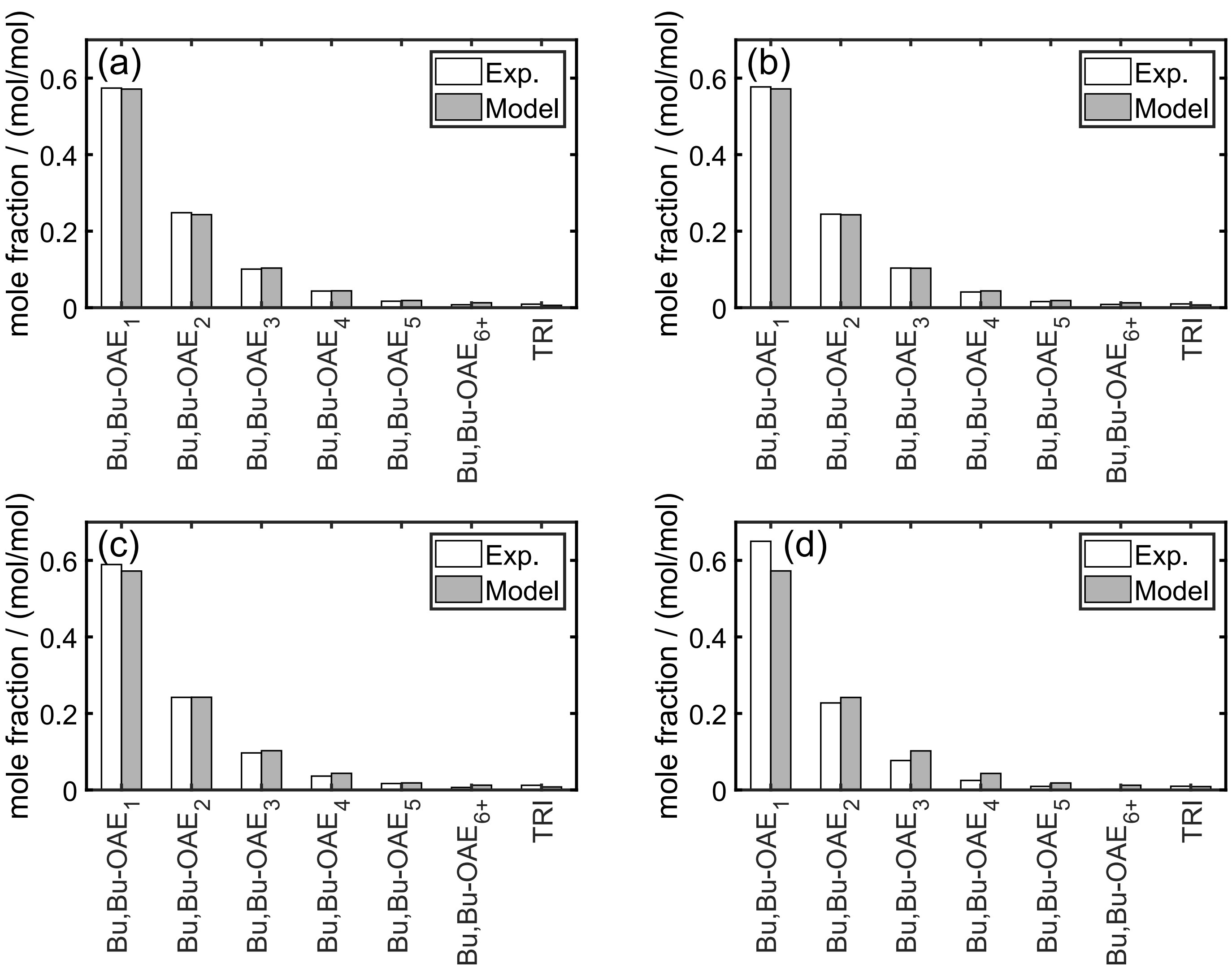

Figure 54: Comparison between the experiment and the model results for reaction experiment E3 ((a) T = 303.15 K, (b) T = 323.15 K, (c) T = 343.15 K, (d) T = 363.15 K).

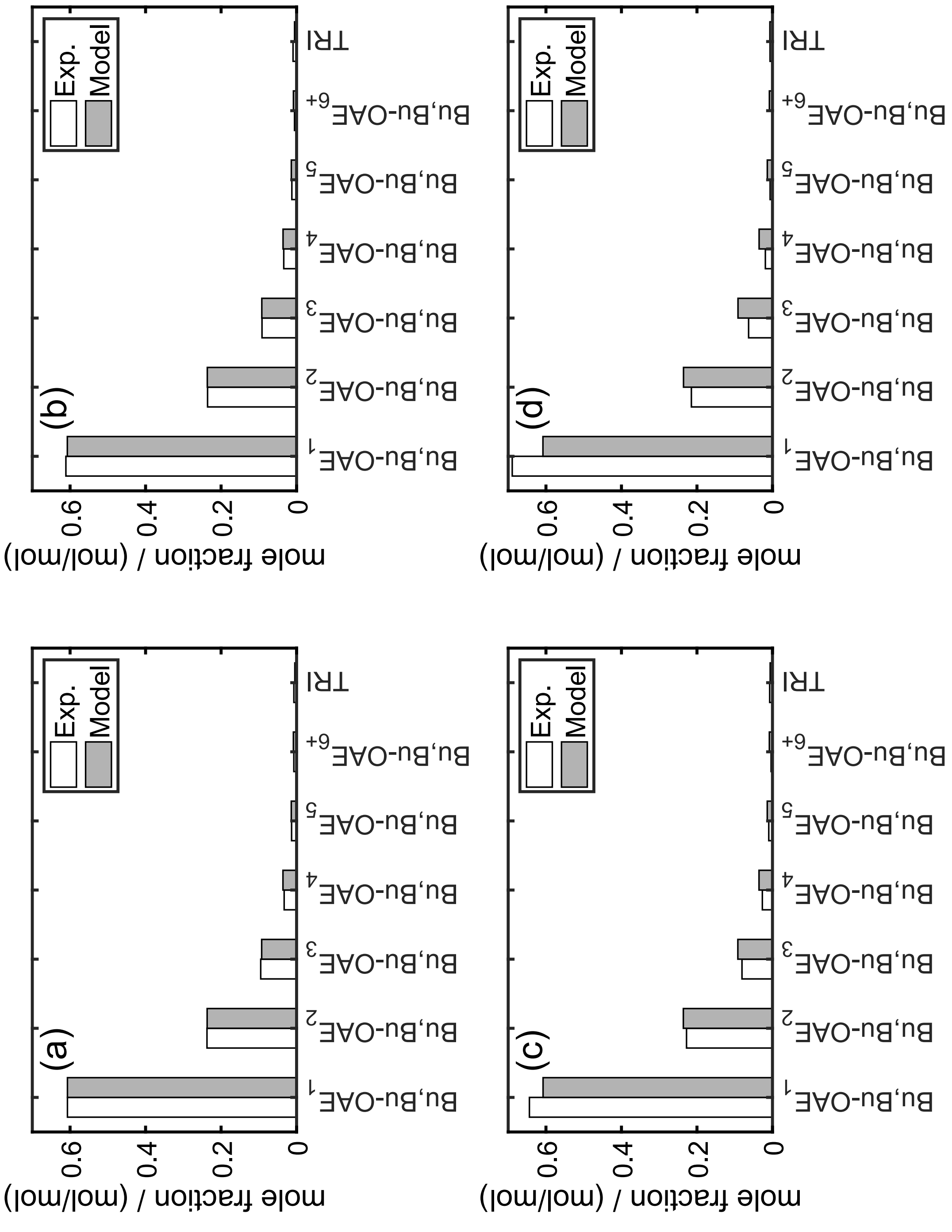

Figure 55: Comparison between the experiment and the model results for reaction experiment E4 ((a) $T = 303.15$ K, (b) $T = 323.15$ K, (c) $T = 343.15$ K, (d) $T = 363.15$ K).

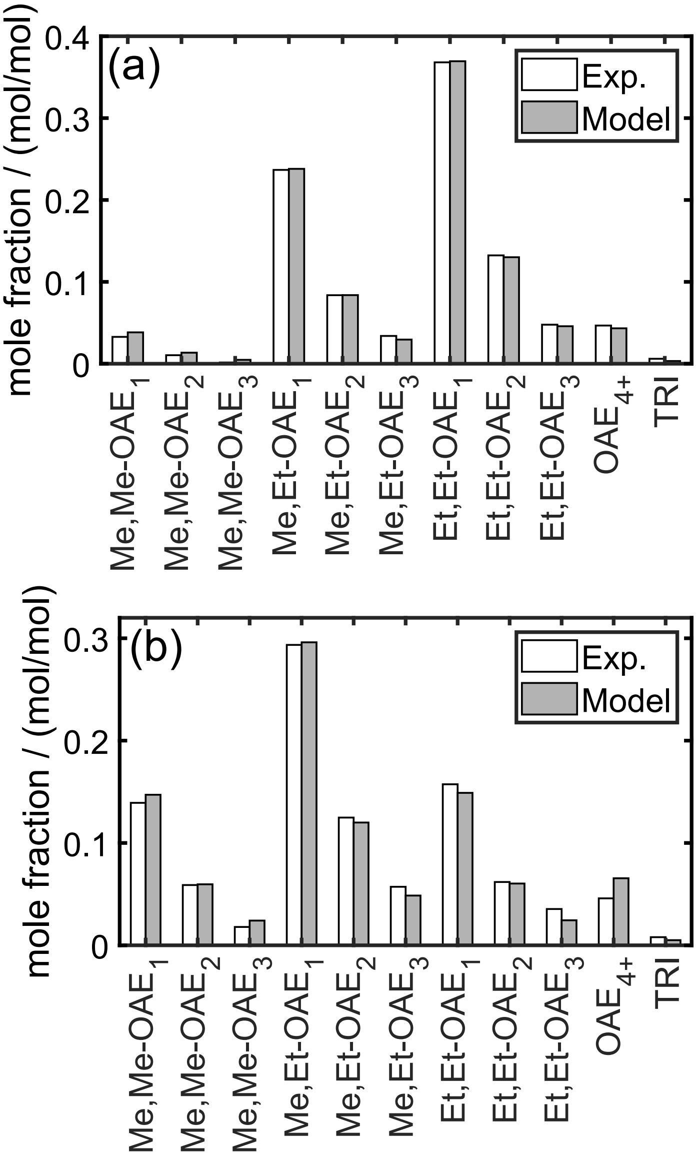

Figure 56: Comparison between the experiment and the model results for reaction experiments E6 (a) and E7 (b).

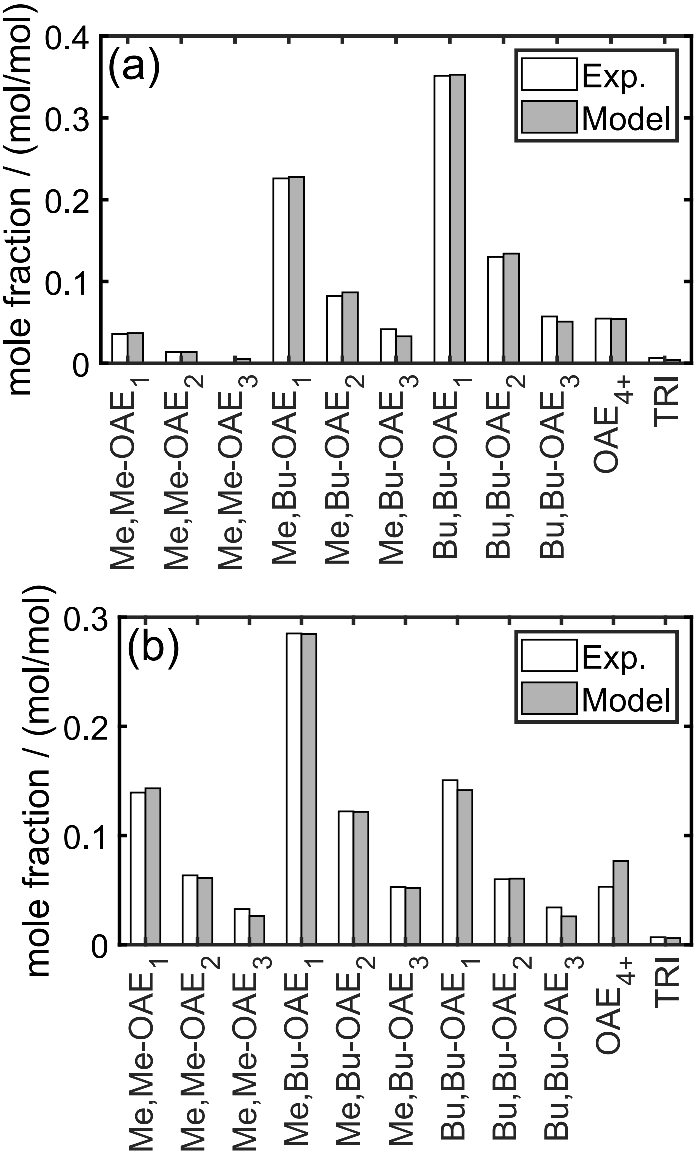

Figure 57: Comparison between the experiment and the model results for reaction experiments E9 (a) and E10 (b).

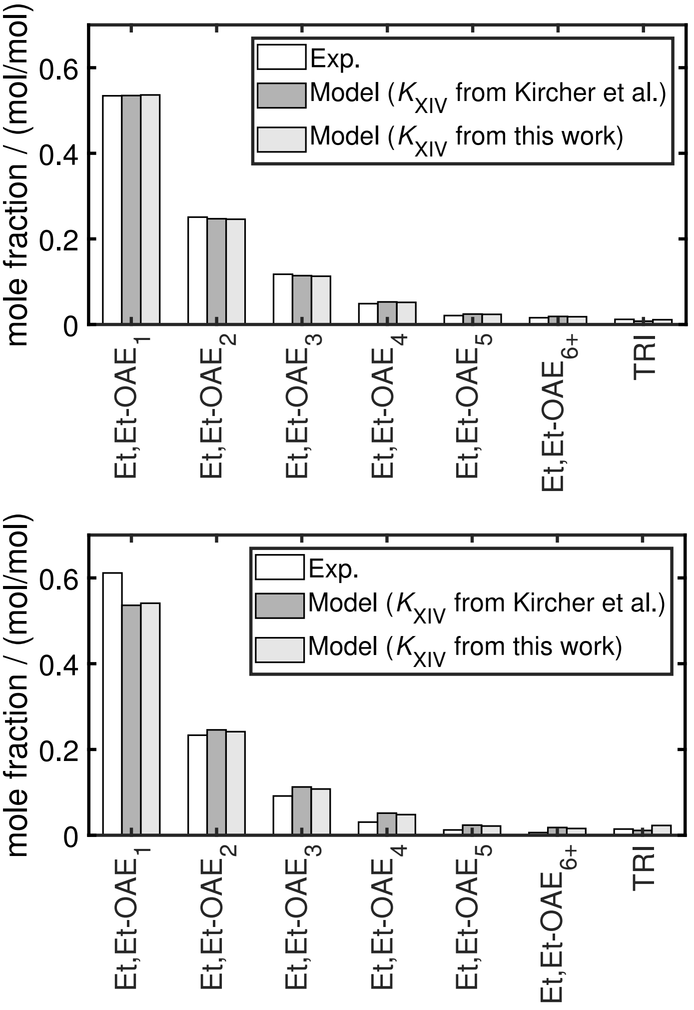

Figure 58: Comparison between the experiment, the model results with the parameters from Kircher et al. [92], and the model results with the parameters from the present work (see main part for parameter values) for reaction experiment E1 ((a) $T = 303.15$ K, (b) $T = 363.15$ K).

Declaration

This dissertation contains material that has been published previously or that is included in submitted publications. In the following, these publications are listed together with a statement on the contributions of the author of the present dissertation.

- J. Voggenreiter, J. Burger: Side Products in the Water-Tolerant Synthesis of Poly(oxymethylene) Dimethyl Ethers: Formation Kinetics and Implications for Process Design, Industrial & Engineering Chemistry Research 60 (2021) 2418-2429.

  The author set up and carried out the experiments, and evaluated the results. The author developed the model and carried out the parameterization. The author performed the process simulation and evaluated the results. The author wrote the manuscript.

- J. Voggenreiter, J. Burger: Irreversible Bildung von Nebenprodukten bei der Synthese von Poly(oxymethylen)dimethylethern, Chemie Ingenieur Technik 93 (2021) 844-849.

  The author set up and carried out the experiments, and evaluated the results. The author developed the model and carried out the parameterization. The author wrote the manuscript.

- J. Voggenreiter, A. Ferre, J. Burger: Scale-up of the Continuous Production of Poly(oxymethylene) Dimethyl Ethers from Methanol and Formaldehyde in Tubular Reactors, Industrial & Engineering Chemistry Research, *accepted* (2022).

  The author set up and carried out the experiments, and evaluated the results. The author developed the model and carried out the parameterization. The author performed the process simulation and evaluated the results. The author wrote the manuscript.

- J. Voggenreiter, P. van de Zande, J. Burger: Generalized Model of the Chemical Equilibrium of Transacetalization and Oligomerization of Poly(oxymethylene) Dialkyl Ethers, Chemical Engineering Science, *submitted* (2022).

The author carried out the experiments and evaluated the results together with Pascal van de Zande. The author developed the model. The author wrote the manuscript.

Student theses

The following student theses were prepared under the supervision of the author of the present doctoral thesis in the frame of his research:

- P. van de Zande: Experimentelle Untersuchung von formaldehydhaltigen Mischungen mit Kernspinresonanzspektroskopie (NMR). Bachelor thesis, Laboratory of Chemical Process Engineering (CTV), Technical University of Munich (2021).
- M. Tobler: Experimental study of chemical equilibria with nuclear magnetic resonance spectroscopy (NMR). Bachelor thesis, Laboratory of Chemical Process Engineering (CTV), Technical University of Munich (2021).
- F. Turkowksi: Experimentelle Untersuchung der kontinuierlichen Synthese von Poly(oxymethylen)dimethylethern in einem Rohrreaktor. Bachelor thesis, Laboratory of Chemical Process Engineering (CTV), Technical University of Munich (2020).